Title

On the Influence of Superhydrophobic Coatings on Turbulent Boundary Layer Separation

Author

Grieb, Daniel Joseph

Publication Date

2022

Peer reviewed|Thesis/dissertation

On the Influence of Superhydrophobic Coatings on Turbulent Boundary Layer Separation

by

Daniel Joseph Grieb

A dissertation submitted in partial satisfaction of the

requirements for the degree of

Doctor of Philosophy

in

Engineering - Mechanical Engineering

in the

Graduate Division

of the

University of California, Berkeley

Committee in charge:

Assistant Professor Simo A. Mäkiharju, Co-chair
Professor Ömer Savaş, Co-chair
Professor Philip S. Marcus
Professor Evan A. Variano

Summer 2022

On the Influence of Superhydrophobic Coatings on Turbulent Boundary Layer Separation

Abstract

On the Influence of Superhydrophobic Coatings on Turbulent Boundary Layer Separation

by

Daniel Joseph Grieb

Doctor of Philosophy in Engineering - Mechanical Engineering

University of California, Berkeley

Assistant Professor Simo A. Mäkiharju, Co-chair

Professor Ömer Savaş, Co-chair

This experimental study of turbulent boundary layer separation from a contoured backward facing ramp demonstrates that a spray-on superhydrophobic coating modifies the location of turbulent boundary layer separation. A custom water tunnel was designed and constructed to study turbulent boundary layer separation from a backward facing ramp located downstream of a flat plate. Particle image velocimetry was used to measure the velocity field and identify the onset of turbulent boundary layer separation. The flow rate within the water tunnel was adjusted to study the separation of turbulent boundary layers at Reynolds numbers based on the plate length of 500,000 to 6,000,000.

Experiments on a smooth baseline surface showed that the turbulent boundary layer remained fully attached along the ramp at low flow rates. The boundary layer detached as the fluid velocity was increased, and the location of the onset of separation advanced upstream with increasing velocity. The application of a superhydrophobic coating caused the onset of separation to occur at a lower flow rate, as well as the location of separation to advance further upstream at a fixed flow rate. Analysis of the velocities in the turbulent boundary layer upstream of the ramp show that the separation location is modified due to a decrease in the Reynolds shear stress within the boundary layer. This decrease in turbulent mixing, brought about by the presence of a superhydrophobic coating, reduces the transport of momentum to the wall which leads to earlier onset of turbulent boundary layer separation. This identifies a concern that should be addressed as superhydrophobic coatings are investigated as a method for reducing ship resistance within the maritime industry.

To my wife, Sarah

You are the reason I was able to complete this endeavor.

And to my children, Phoebe and Gus

I hope that you both have as many learning opportunities as I have had.

Contents

List of Figures

List of Tables

Acknowledgments

I would like to thank everyone who supported me in my research. Specifically, I would like to thank the plethora of lab mates I have worked with, the team in the UC Berkeley Mechanical Engineering machine shop, my committee members, and my advisors. I would like to make a special acknowledgement of Clayton Pelzer, who's partnership was invaluable in getting the flow loop operational. I would like to thank family and friends who have supported me and my wife, as well as cared for our children. Most of all, I would like to thank my wife who has supported me and loved me far more than I could ever have asked.

Chapter 1

Background

1.1 Motivation

The goal of reducing the resistance of ships is driven by both the operating costs that result from fuel consumption, as well as the desire to reduce greenhouse gas emissions. To that end, advances in drag reduction technology, as well as improved understanding of the physics of flow around a ship hull, are needed to enable more efficient ship designs. This work focuses on the intersection of two fields of fluid dynamics research: the study of superhydrophobic coatings intended for drag reduction and the study of turbulent boundary separation in adverse pressure gradients.

Environmental Impact of Ships

The rise of a globally integrated economy has driven an increase in the international transport of trade goods. As of 2008, The maritime shipping industry annually accounted for approximately 750 megatons of CO_2 emissions globally. Based on estimate from a study by the European Union committee on Environment, Public Health, and Food Safety, maritime transport is predicted to account for 17% of the global carbon footprint by 2050.[1] In order to reduce this source of carbon emissions, the efficiency of ships must be improved through improvements in engine efficiency and reduction in drag.

In addition to the maritime industry's impact on greenhouse gases, the particulate matter pollution from maritime transport has a direct impact on human health. A recent study of the impact of low-sulphur marine fuels showed that though cleaner marine fuels are expected to reduce ship-related premature mortality and morbidity by up to 54%, ships using low-sulphur fuels are still expected to contribute to approximately 250k premature deaths annually. The particulate matter pollution from marine fuels additionally contributes to 6.4M annual cases of childhood asthma.[2] Technologies that reduce maritime fuel consumption can help reduce this impact.

Drag on Ships

Ship resistance is primarily composed of the wave resistance and viscous resistance. The wave resistance results from the force required to push a ship through the water at the free surface. As a ship moves along the surface of the water, it pushes the crest of a wave in front of it. It also pulls the crest of a wave behind it. These two wave crests correspond with high pressure stagnation points at the bow and stern of the vessel. Wave resistance scales with the Froude number of the ship:

$$Fr_{ship} = \frac{U_{ship}}{\sqrt{gL_{ship}}}$$

The Froude number is a ratio between the speed of the ship and the natural speed of a wave with a wavelength that matches the length of the ship. The wave resistance take the form:

$$R_W = C_W * \frac{1}{2}\rho U_{ship}^2 S$$

where the wave resistance coefficient C_W is a function of the Froude number, ρ is the water density, and S is the wetted area of the ship hull. The coefficient of wave resistance C_W is typically determined experimentally on a scale model in a towing basin.

The viscous resistance results from the viscosity of the water diffusing the momentum of the ship into the surrounding water. The viscous resistance scales with the Reynolds number:

$$Re_{ship} = \frac{U_{ship}L_{ship}}{\nu}$$

where ν is the kinematic viscosity of the water. The Reynolds number is the ratio between the inertial forces and viscous forces of the flow. The viscous resistance takes the form:

$$R_V = C_V * \frac{1}{2}\rho U_{ship}^2 S$$

where the viscous resistance coefficient C_V is a function of the Reynolds number.

It should be noted that the Froude number scales with the velocity scale in the numerator and the length scale in the denominator. This enables the Froude number of a full scale ship to be matched in a model test by reducing both the length scale and the velocity scale appropriately. In contrast, the Reynolds number scales with both the velocity and length in the numerator. Therefore a model scale test of a ship hull cannot simultaneously match the Froude number and Reynolds number of the full scale ship at the same time. Furthermore, it is impractical to attempt to match full scale Reynolds numbers during a model test of a very large ship, as the velocity would need to be increased and the viscosity decreased to such an extent that additional undesired physical phenomena would occur such as cavitation in liquid test fluid, or the effects of compressibility if a model test were to occur in a gas. As a result, naval architects predicting the total resistance of a ship traditionally rely on experimental determination of the wave resistance based on model testing at the correct Froude number. The viscous resistance is predicted based on an empirical

model of the effects of viscosity. This prediction of viscous resistance is guided by fundamental understanding the physics of the flow around the ship hull. Further understanding of viscous flows at high Reynolds numbers can improve the accuracy of the prediction of the coefficient of viscous resistance. This can enable naval architects to improve the efficiency of ship hullforms, thereby reducing the operating cost and lowering the carbon footprint of a significant portion of global trade.

For large vessels, such as tankers and container ships, their extreme length creates waves with a phase velocity much higher than the ship can travel. This leads to a low Froude number and low wave-making resistance. It is estimated that for a typical container ship, the skin friction drag makes up approximately 70% of the total resistance, while the effects of boundary layer separation make up approximately 10% to 12% of the total resistance.[3]

While skin friction is the dominant mechanism contributing to the resistance of large cargo vessels, viscous pressure drag resulting from boundary layer separation can account for up to 15% of the total resistance [3]. Boundary layer separation in the adverse pressure gradient at the stern of a ship occurs when there is insufficient momentum in the boundary layer near the wall to overcome the rise in pressure. The present study focuses on how SHS frictional drag reduction may influence the location at which a turbulent boundary layer separates in an adverse pressure gradient. For example, while a lesser momentum deficit near the wall might delay separation, reduced Reynolds stresses in the TBL might also hasten flow separation.

Recent studies (e.g. [4][5][6]) have focused on reducing the viscous resistance through the application of superhydrophobic surfaces (SHS). These have shown that application of SHS to a flat plate can in some cases allow, from a macroscopic view point, for a relative 'slip' between the wall and the near-wall fluid in a turbulent boundary layer leading to drag reduction through a reduction in skin friction. However, drag increase may also result, if the roughness of the SHS exceeds the viscous sublayer thickness [4].

1.2 Superhydrophobic Surfaces

A superhydrophobic surface is defined as surface which has a static contact angle with water of greater than 150°. Additions to this definition of a superhydrophobic surface often discuss the surface having a low contact angle hysteresis, which is dependent of the state of a droplet on the surface. In Wenzel's state, the droplet wets the surface between protruding surface roughness features, thereby pinning the droplet to the surface and demonstrating high contact angle hysteresis. In Cassie's state, the droplet does not wet the surface, instead sitting atop the protruding roughness features. This allows the droplet to exhibit low contact angle hysteresis and easily roll off of the surface. The most robust state for repelling droplets is named after the Lotus leaf. As a special case of Cassie's state, the "Lotus" state relies on hierarchical micro- and nanoscale surface topography to repel the droplets from the roughness protrusions it contacts, resulting in extremely low contact angle hysteresis.[7] This hierarchical surface structure is desirable when applying a superhydrophobic coating as a drag reduction method.

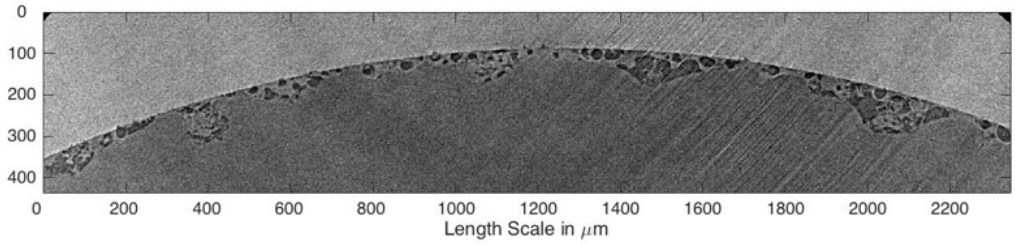

Figure 1.1: One slice from 3D microscopic computed tomography of a superhydrophobic coating on the inner diameter of an aluminum tube filled with water. This data was collected at the Advanced Light Source at Lawrence Berkeley National Laboratory.

While an SHS is defined based on the contact angle between a droplet of water and a dry surface, the application of an SHS to reduce drag requires the surface to be submerged in water. Instead of having droplets beaded up on the surface, a submerged SHS will be covered with small bubbles of air adhering to the surface. These bubbles are referred to as plastrons. The performance of an SHS as a drag-reducing coating is dependent on the state of these plastrons.

We began an investigation of the state of the plastrons and how they relate to a turbulent flow passing over them. The experiment was designed to use microscopic computed tomography (μCT) x-ray imaging of the plastrons on the inner surface of a pipe as water was pumped through the pipe at high Reynolds numbers. The experiment was designed to use the dedicated μCT beamline 8.3.2 of the Advanced Light Source (ALS) at Lawrence Berkeley National Laboratory. However scheduling delays, exacerbated by the COVID-19 pandemic, resulted in the experimental study not being completed to date.

Though the study at the ALS was not completed as planned, preliminary data collected with static water in an SHS-coated aluminum pipe provides a clear example of plastrons in figure 1.1. The image is one slice from a three-dimensional reconstruction of the interrogation volume. The upper half of the image shows the wall of an aluminum pipe. The lower half of the image shows the water contained within the pipe. The dark patches along the circular arced interface between the aluminum and the water are plastrons of air adhering to the surface. The superhydrophobic coating is difficult to identify, as its x-ray attenuation is comparable to that of water. The plastrons cling to the surface texture of the coating. Further research is needed to understand how the plastrons get pulled off of the surface, how they can be replenished, and how many are needed into order to achieve drag reduction.

1.3 Superhydrophobic Surfaces for Skin Friction Reduction

The proposed mechanism by which an SHS reduces skin friction is that the plastrons act as a buffer between the water flowing past and the underlying surface. The air within the plastrons, being lower

dynamic viscosity than the water, allows for a steeper velocity gradient than exists in the water. As a result, from a macroscopic viewpoint, the velocity within the water behaves as if there is some relative slip between the water and the wall, instead of adhering to the no-slip boundary condition. This relative slip allows for a less steep velocity gradient and subsequently lower shear stress.

Work by Seo and Mani [5] used direct numerical simulation to study the relative slip of a turbulent flow over a superhydrophobic surface. The SHS was modeled as an organized grid of solid posts with air between them. They found the relationship between the velocity gradient at the wall and the apparent slip velocity at the wall to follow a linear trendline. The constant slope of that trendline is consistent with the concept of a particle SHS having a specific slip length, λ_{slip}, which is the ratio between the velocity gradient at the wall and the slip velocity. In other words, the amount of slip at the wall is dependent on the conditions of the flow, but can be modeled as follows.

$$u_{slip} = \lambda_{slip} \left. \frac{\partial u}{\partial y} \right|_{wall} \tag{1.1}$$

Research presented by Gose et al. evaluates four different types of superhydrophobic surfaces in a turbulent channel flow.[4] They observed highly variable changes in drag, ranging from 90% increase to 90% reduction. They attribute the variation in drag reduction to surface roughness. As the location of the interface between the plastron and the water can vary with pressure, the distance that a roughness element protrudes into the boundary layer will change as well. A surface is considered hydraulically smooth when the roughness elements remain within the viscous sublayer, defined as five viscous length scales (see equation 2.15) from the wall. They observed that SHS coatings that seem hydraulically smooth in the mean sense, based on a root mean square roughness, can have a few very large roughness features. These large roughness features protruding beyond the viscous sublayer can create a form drag that offsets the drag reduction achieved by slip over the plastrons.

Further work by Gose et al. used laser Doppler velocimetry (LDV) to measure the velocities in a turbulent boundary layer over several superhydrophobic coatings.[8] This data showed an increase in mean velocity throughout the boundary layer, as well as showing the velocity profile to trend towards a non-zero slip velocity at the wall. Additionally, the Reynolds shear stress is observed to be increased throughout the boundary layer. This leads to the total stress (being the combined viscous stress and Reynolds shear stress) to be increased outside of the viscous sublayer and deceased within it, relative to the smooth wall case. It is proposed that the increased Reynolds stress comes from the presence of surface roughness introduced by the SHS. Another noted possible explanation for increased Reynolds stress is that the inner and outer region of the boundary layer may not yet be in equilibrium, as the boundary layer development began on an smooth surface.

A recent review paper of superhydrophobic drag reduction in turbulent flows by Park et al. summarizes recent progress that has been made in understanding the mechanism of drag reduction.[6] They summarize results from 26 separate experimental studies of superhydrophobic surfaces exposed to turbulent flows. A key takeaway from their review of these experiments is that for randomly rough superhydrophobic surfaces (such as we use in our study), the state and thickness of the plastrons can vary greatly, leading to a broad range of drag reduction performance for the same surface. An overgrown plastron can lead to more apparent slip at the wall than would be predicted by the

scale of the roughness. Conversely, as the plastron thins below the tallest peaks of surface roughness, the peaks can extend into the water flow offsetting the skin friction reduction of the regions of slip and sometimes leading to drag increase. The estimated change in drag reported across the broad range of experimental setups and measurement techniques ranged from 90% drag increase to 90% drag reduction, with most data falling between 20% drag increase and 40% drag reduction. The review identified three different experimental setups that were used to study the superhydrophobic coating NeverWet or its precursor, which all reported achieving a drag reduction of up to 20% to 35%, depending on the conditions of the study.

1.4 Roughness Modifying Turbulent Boundary Layer Separation

While we have not found previously published work focused on the influence of superhydrophobic surfaces on turbulent boundary layer separation, the interaction between surface roughness and turbulent boundary layer separation has been an active field of research. One particularly relevant experimental study presented by Song and Eaton [9] looked at a turbulent boundary layer separating from a contoured ramp downstream of a flat plate. The ramp has a constant radius in order to avoid fixing the separation location at a sharp corner and instead allow separation to occur at a location determined by the flow conditions. The work compares the case of a smooth surface to when the flat plate and ramp were fully rough. They observed flow velocities above the ramp that suggest that the boundary layer over the rough wall separates further upstream than the smooth wall case. However their instrumentation setup using a two-component laser Doppler anemometer did not allow them to identify the exact separation location. It was noted that upstream of the ramp the Reynolds shear stress normalized by the friction velocity, $\frac{\overline{u'v'}}{U_\tau}$, was comparable between the rough wall and smooth wall cases.

Further work with this experimental setup was published by Aubertine, Song, and Eaton [10]. This work extends the study to a higher Reynolds number by modifying the viscosity. Additionally, it confirms that roughness shifts the separation location upstream, from approximately 74% of ramp length in the smooth wall case to 62% of the ramp length in the fully rough case. Another conclusion from the study is that the Reynolds stresses scaled by the friction velocity are unchanged between the smooth and rough cases, within their measurement uncertainty.

It should be noted that the skin friction increases significantly for the rough wall case, and subsequently the friction velocity as well. Therefore the Reynolds stresses in dimensional units, or when scaled by the freestream velocity, are increased by the presence of wall roughness. This increased turbulent mixing, which could help delay separation, does not overcome the additional momentum loss due to the increased skin friction of a fully rough wall, resulting in the separation location moving upstream.

Chapter 2

Theory

2.1 Behavior of Turbulent Boundary Layers

The large length scales of ships traveling at moderate speeds lead to high Reynolds number turbulent flows. Turbulent flows are characterized by unsteady, three-dimensional, seemingly random velocity fluctuations across a broad range of length scales. The span between the largest and smallest length scales of the flow increases with the Reynolds number. This range of scales is driven by the nonlinearity in the convective derivative seen in the Navier-Stokes equations, as follows.

$$\frac{\partial u_i}{\partial t} + \frac{\partial}{\partial x_j}(u_i u_j) = -\frac{\partial p}{\partial x_i} + \nu \frac{\partial}{\partial x_j}\left(\frac{\partial u_i}{\partial x_j} + \frac{\partial u_j}{\partial x_i}\right) \tag{2.1}$$

$$p = \frac{P}{\rho} \tag{2.2}$$

$$\frac{\partial u_i}{\partial x_i} = 0 \tag{2.3}$$

Once a flow becomes unstable, the nonlinear interaction between motions of different wavenumbers create a cascade of energy to smaller and smaller length scales. At the smallest scales the energy is dissipated by viscosity. The Reynolds number, being the ratio of inertial forces to viscous forces, quantifies the how well the viscosity can dissipate the energy of the largest scale motions of the flow. As the Reynolds number increases, energy is able to cascade to smaller and smaller scales before it is fully dissipated by viscosity. The smallest length scale of the flow, at which energy is fully dissipated, is referred to as the Kolmogorov length scale.[11][12] Very high Reynolds number turbulent boundary layers develop on the hulls of ships due to the large length scale at moderate velocities. The Reynolds number based on ship length can be on the order of $3 * 10^9$.

While a turbulent flow is constantly fluctuating, the average behavior can be represented by the Reynolds decomposition, where the velocity is decomposed into a mean term plus a fluctuating term as follows.

$$u_i = \bar{u}_i + u_i' \tag{2.4}$$

Applying the boundary layer approximations of $\bar{v} \ll \bar{u}$ and $\frac{\partial}{\partial x} \ll \frac{\partial}{\partial y}$ to the Reynolds averaged Navier-Stokes equations, the resulting equations for a Reynolds averaged two-dimensional turbulent boundary layer are as follows.[13] Note that U_e is the velocity in the streamwise direction outside the boundary layer.

$$\frac{\partial \bar{u}}{\partial x} + \frac{\partial \bar{v}}{\partial y} = 0 \tag{2.5}$$

$$\bar{u}\frac{\partial \bar{u}}{\partial x} + \bar{v}\frac{\partial \bar{u}}{\partial y} \approx U_e \frac{dU_e}{dx} + \frac{1}{\rho}\frac{\partial \tau}{\partial y} \tag{2.6}$$

$$\tau = \mu\frac{\partial \bar{u}}{\partial y} - \rho\overline{u'v'} \tag{2.7}$$

At a single streamwise location, the overall shape of the boundary layer is described by several integral parameters. The boundary layer thickness δ is defined as the distance from the wall that the average velocity is 99% of the local freestream velocity. This is difficult to identify without measuring the velocity field within the boundary layer and well into the freestream. The displacement thickness δ^* is a measure of how the boundary layer blocks the flow of the fluid in the freestream, defined below. The momentum thickness θ is a measure of how much momentum has been removed from the freestream flow to create the boundary layer. The momentum shape factor $H = \delta^*/\theta$ is defined as the ratio between the displacement thickness and momentum thickness.

$$\delta^* = \int_0^\infty \left(1 - \frac{\bar{u}}{U_e}\right) dy \tag{2.8}$$

$$\theta = \int_0^\infty \frac{\bar{u}}{U_e}\left(1 - \frac{\bar{u}}{U_e}\right) dy \tag{2.9}$$

The von Kármán momentum integral (VKMI) equation describes the evolution of the boundary layer in the streamwise direction in terms of these parameters. After algebraic substitution of the Reynolds averaged continuity equation into the streamwise momentum equation (given in equation 2.6), integrating the momentum equation across the boundary layer leads to the following equation.[13]

$$\frac{d\theta}{dx} + (2 + H)\frac{\theta}{U_e}\frac{dU_e}{dx} = \frac{\tau_w}{\rho {U_e}^2} = \frac{C_f}{2} \tag{2.10}$$

2.2 Structure of a Turbulent Boundary Layer

While the VKMI describes the integral properties of the boundary layer, it does not describe the detailed structure of the velocity profile. The velocity profile in a turbulent boundary layer is described by functions empirically fit to data from experimental measurements. A simple one-seventh power-law approximate velocity profile suggested by Prandtl has proved useful for general approximations of the properties of a zero pressure gradient (ZPG) turbulent boundary layer.[14] This

approximation is given as follows, where δ is the measure of the boundary layer thickness, though not necessarily as rigorously defined as the 99% boundary layer thickness δ_{99}.

$$\frac{\bar{u}}{U_e} \approx \left(\frac{y}{\delta}\right)^{1/7} \tag{2.11}$$

Applying this profile to the VKMI with the simplification to a ZPG turbulent boundary layer and solving the resultant ordinary differential equation can give some useful approximations for several boundary layer parameters. Equation 2.12 gives an estimate for the boundary layer thickness. Note that the boundary layer thickness increases as a 6/7 power law function of distance from an origin where the boundary layer begins to develop, and the thickness decreases with higher freestream velocities. Equation 2.13 provides an estimate for the local skin friction coefficient, which notably decays in the streamwise direction as the boundary layer gets thicker. Integration of the assumed velocity profile in equation 2.11 results the simple approximation for the momentum thickness of $\theta \approx 7\delta/72$.[13]

$$\frac{\delta}{x} \approx \frac{0.16}{Re_x^{1/7}} \tag{2.12}$$

$$C_f \approx \frac{0.027}{Re_x^{1/7}} \tag{2.13}$$

A more detailed description of the velocity profile is given by the Law of the Wall and the corollary Law of the Wake introduced by Coles.[15] This description relies on normalizing variables by the wall-friction velocity v^* and the related viscous length scale l as follows. The resulting variables are often referred to as inner variables or wall units.

$$v^* = \left(\frac{\tau_w}{\rho}\right)^{1/2} \tag{2.14}$$

$$l = \frac{\nu}{v^*} \tag{2.15}$$

$$u^+ = \frac{\bar{u}}{v^*} \tag{2.16}$$

$$y^+ = \frac{yv^*}{\nu} = \frac{y}{l} \tag{2.17}$$

The region immediately adjacent to the wall is referred to as the viscous sublayer. In the region of $y^+ < 5$, the velocity profile is linear, following the relationship $u^+ = y^+$. The approximate region of $35 \leq y^+ \leq 350$ is referred to as the logarithmic overlap layer, where the velocity profile can be described by a logarithmic law in either the inner variables or the dimensional outer variables. Beyond this layer, the velocity demonstrates a "wake" profile that rises faster than described by the log law. This region, called the outer layer or wake region, is dependent on the pressure gradient in the freestream flow. Both of the overlap layer and the outer layer can be described by the following

equation in terms of the turbulent boundary layer constants κ and B and the pressure gradient constant A.

$$u^+ \approx \frac{1}{\kappa}\ln\left(y^+\right) + B + \frac{2\Pi}{\kappa} f\left(\frac{y}{\delta}\right) \tag{2.18}$$

where $f(\eta) \approx sin^2\left(\frac{\pi}{2}\eta\right) \approx 3\eta^2 - 2\eta^3$ and $\Pi = \frac{\kappa A}{2}$

The region between the viscous sublayer and the log layer ($5 \leq y^+ \leq 30$) is referred to as the buffer layer, where the velocity profile smoothly transitions from a linear relationship to a logarithmic relationship. Spalding proposed the following equation to match experimental data in all three of these regions up to approximately $y^+ = 100$.[16]

$$y^+ = u^+ + e^{-\kappa B}\left[e^{\kappa u^+} - 1 - \kappa u^+ - \frac{\left(\kappa u^+\right)^2}{2} - \frac{\left(\kappa u^+\right)^3}{6}\right] \tag{2.21}$$

2.3 Turbulent Boundary Layer Separation

When the flow outside the boundary layer slows down due to changes in flow area, the static pressure will rise along the streamline. This is due to the conservation of energy in an inviscid flow, as described by Bernoulli's equation below, where ϕ represents the velocity potential.

$$\rho\frac{\partial\phi}{\partial t} + p + \frac{1}{2}\rho V^2 + \rho g z = const \tag{2.22}$$

When a boundary layer faces this rise in pressure, it is referred to as an adverse pressure gradient. Due to the energy that has been removed from the fluid in the boundary layer, the fluid near the wall does not have as much kinetic energy as the fluid in the freestream. Therefore the fluid in the boundary layer is unable to rise as high in pressure through the recovery of kinetic energy, compared to the freestream. The resulting flow behavior, known as boundary layer separation, is seen when the flow at the wall stagnates. The freestream flow stops faithfully following the contour of the wall and instead the streamlines turn downstream. The near-wall region past the stagnation point often is filled with recirculating flow at a relatively low pressure. This low pressure region can cause increased drag on a body.

Superhydrophobic surfaces reduce skin friction by creating a relative slip between the solid surface and a liquid flowing over it. This relative slip is achieved through microscopic bubbles, or plastrons, that are held within the texture of the surface. The shear stress within the liquid boundary layer is transferred to the air within the plastrons, creating flow within the plastron, instead of being reacted by a larger force on a solid surface. The result is that the turbulent boundary layer has reduced skin friction, as well as higher velocities (possibly non-zero in a spatially-averaged sense) near the wall.

The influence of superhydrophobic surfaces on boundary layer separation has not yet been investigated. However, there are several possible ways to evaluate the possible influence of reduced

skin friction on the behavior in an adverse pressure gradient leading up to separation. First, we can revisit the von Kármán momentum integral given in equation (2.10).

Here, a reduction in the skin friction term τ_w is shown to reduce the rate at which the momentum thickness grows. However, one common criteria to identify the expected point of boundary layer separation is the shape factor H. The point of separation is predicted between $H = 1.8$ and $H = 4.0$, depending on the criteria.[17] However, the VKMI does not describe how the shape factor will evolve in the streamwise direction. Several correlations relating shape factor H, momentum thickness θ, and skin friction coefficient C_f have been proposed as a closure to the problem of integrating the VKMI to predict boundary layer behavior. However, all of these correlations are based on data without partial slip occurring at the wall. They are not expected to remain valid when the skin friction behavior is modified and therefore is not a good prediction of the influence of SHSs on boundary layer separation. In spite of this, we can note that these correlations show a trend of increasing H with decreasing C_f, assuming a fixed θ.[13] A reduction in θ also trends toward an increase in H, as seen in the definition of $H = \delta^*/\theta$. The conclusion of this investigation of the VKMI is that it is suggested that reduction in skin friction may speed up the onset of boundary layer separation, but the picture is still unclear and incomplete.

A second way of looking at the influence of reduced skin friction is to investigate a special class of flows referred to as equilibrium turbulent flows. These flows have been shown to have properties that scale with a single parameter when Clauser's equilibrium parameter β is held constant. These flows are more prone to boundary layer separation with higher values of β, which is defined as follows.[13]

$$\beta = \frac{\delta^*}{\tau_w}\frac{dp_e}{dx} \tag{2.23}$$

It can be seen from the definition that β will be affected by reduced skin friction achieved by SHS coatings. A reduction in skin friction will increase the value of β. This effect will be counteracted by the decreased displacement thickness that results from less skin friction on the surface upstream of a given location being investigated. Once again, it is unclear what insight can be drawn in order to predict how an SHS coating will influence boundary layer separation.

There are several competing arguments based on fundamental physics as to how SHS coatings will influence turbulent boundary layer separation. Firstly, a boundary layer is prone to separation because the fluid does not contain enough momentum to overcome an adverse pressure gradient. By this argument, reducing skin friction will allow the boundary layer to maintain more momentum and thereby rise to a higher static pressure prior to separation. Conversely, there is an argument that the reason turbulent boundary layers do not separate as soon as laminar boundary layers is due to turbulent mixing of high momentum fluid closer to the wall. This would mean that reduced skin friction would lead to a less "potent" level of turbulence (to borrow a description from Prof. Savaş), which would subsequently reduce the mixing and accelerate the onset of boundary layer separation. This is consistent with the previously mentioned correlations between θ and H for fixed levels of the skin friction coefficient C_f.

Stratford lays out a simplified balance of forces in the boundary layer that can be extended to the case of SHS coatings reducing skin friction.[18] He argues that in the outer region of the boundary

layer the shear stress is relatively low and the pressure gradient is balanced by the reduction in velocity. For the inner region of the boundary layer the low inertia of the fluid causes the velocity profile to distort such that the pressure gradient is primarily balanced by the difference in shear stress between the wall and the top of the inner region. With high pressure gradients, the wall shear stress goes to zero in order to allow the pressure gradient to be balanced by the shear stress off of the wall in the boundary layer. Beyond this point the boundary layer separates as the shear stress off of the wall in the boundary layer cannot overcome any more pressure rise. In light of this, a reduction in the wall skin friction would be expected to accelerate the onset of boundary layer separation.

2.4 Theoretical Discussion Based on the Von Kármán Momentum Integral Equation

Modeling an SHS as causing partial slip assumes that the fluid experiences reduced shear stress at the wall as a result of a relaxation of the no-slip condition. We treat this as a perturbation away from a baseline mean velocity profile, such that the normalized mean velocity profile takes the form $\frac{\bar{u}(y)}{U_e} = \frac{\bar{u}_b(y)}{U_e} + \varepsilon\phi(y)$. This could represent any perturbation in the velocity, such as a renormalization of the roughness function ΔU^+ used in surface roughness literature.[19][20] For the case of slip over an SHS, ε is the slip velocity normalized by the freestream velocity and $\phi(y)$ is a profile function taking a value of unity at the wall and zero in the freestream (presumably with a monotonic decay through the thickness of the boundary layer).

The von Kármán momentum integral equation (VKMI) given in equation 2.10 states that the reduction in shear stress from an SHS will reduce the momentum thickness downstream. However the perturbation in the velocity profile will also change the shape factor $H = \frac{\delta^*}{\theta}$. The shape factor typically evolves from approximately 1.3 in zero pressure gradient to approximately 3 at TBL separation. Predicting the evolution of H in a TBL requires a more complicated model, often correlated or calibrated with experimental data. While there is insufficient data to predict the evolution over an SHS, analysis of the sensitivity of H to the velocity perturbation reveals insights about how an SHS may change the separation location.

We substitute the perturbed velocity profiles into the expressions for θ and δ^* and differentiate with respect to the perturbation scale ε. Note that we split the momentum thickness integral into two regions, above and below the point $y = c$, such that $\bar{u}_b(c) = 0.5$, resulting in the two terms having opposite sign for positive ϕ.

$$\left.\frac{\partial\theta}{\partial\varepsilon}\right|_{\varepsilon=0} = \int_0^c \phi\left\{1 - 2\frac{\bar{u}_b}{U_e}\right\}dy + \int_c^\infty \phi\left\{1 - 2\frac{\bar{u}_b}{U_e}\right\}dy \tag{2.24}$$

$$\left.\frac{\partial\delta^*}{\partial\varepsilon}\right|_{\varepsilon=0} = \int_0^\infty -\phi dy \tag{2.25}$$

The derivative of the shape function with respect to ε takes the following form.

$$\left.\frac{\partial H}{\partial \varepsilon}\right|_{\varepsilon=0} = \frac{1}{\theta}\int_0^\infty -\phi dy - \frac{H}{\theta}\int_0^c \phi\left\{1-2\frac{\bar{u}_b}{U_e}\right\}dy - \frac{H}{\theta}\int_c^\infty \phi\left\{1-2\frac{\bar{u}_b}{U_e}\right\}dy \tag{2.26}$$

Assuming that the perturbation velocity is always positive, representing an increase in the velocity profile, we can see that the first two terms of $\frac{\partial H}{\partial \varepsilon}$ are negative, thereby increasing robustness to separation. They come from decrease in displacement thickness and the decrease in momentum thickness due to additional near-wall velocity, respectively. The third term, which comes from additional velocity being added away from the wall at $y > c$, has a positive sign, as the corresponding reduction in θ leads to a less robust boundary layer. This third term must have a greater magnitude than the second term for the case of reduced shear stress.

The investigation of the signs of these terms suggest that applying SHSs upstream of the separation region may advance the onset of separation due to the increase in velocity away from the wall being dominant. This can be seen from the fact that a reduction in shear stress will reduce the momentum thickness downstream. Meanwhile, application of an SHS coating in the region of separation should primarily affect the near-wall velocities, thereby reducing H and delaying separation. Our experimental investigation was designed to compare the influence on the location of separation of applying SHSs in both the zero pressure gradient region and the adverse pressure gradient region.

2.5 Discussion of the Influence of Terms in the Reynolds-Averaged Boundary Layer Equation

The conservation of linear momentum in the streamwise direction is described by equation 2.6. After assuming constant fluid properties, a characteristic length scale of δ and a characteristic velocity scale of U_0 are selected. Every term can be multiplied by the term $\delta/{U_0}^2$ resulting in the non-dimensional expression as follows:

$$\tilde{u}\frac{\partial \tilde{u}}{\partial \tilde{x}} + \tilde{v}\frac{\partial \tilde{u}}{\partial \tilde{y}} \approx \tilde{U}_e\frac{d\tilde{U}_e}{d\tilde{x}} + \frac{\nu}{U_0\delta}\frac{\partial^2 \tilde{u}}{\partial \tilde{y}^2} - \frac{\partial \overline{\tilde{u}'\tilde{v}'}}{\partial \tilde{y}} \tag{2.27}$$

In equation 2.27 the non-dimensional terms are defined as follows: $\tilde{u} = \frac{\bar{u}}{U_0}$; $\tilde{v} = \frac{\bar{v}}{U_0}$; $\tilde{U}_e = \frac{U_e}{U_0}$; $\overline{\tilde{u}'\tilde{v}'} = \frac{\overline{u'v'}}{{U_0}^2}$; $\tilde{x} = \frac{x}{\delta}$; $\tilde{y} = \frac{y}{\delta}$. On the the left-hand side of the equation, the two terms come from the streamwise and wall-normal portions of the convective derivative. On the right-hand side, the three terms come from the freestream velocity gradient, the viscous stress, and the turbulent stress, respectively. Rearranging the terms and dividing by the non-dimensional streamwise velocity $\tilde{u}$, we arrive at an expression for the rate of change of the streamwise velocity in the streamwise direction

as follows.

$$\frac{\partial \tilde{u}}{\partial \tilde{x}} \approx \frac{\tilde{U}_e}{\tilde{u}} \frac{d\tilde{U}_e}{d\tilde{x}} + \frac{\nu}{U_0 \delta} \frac{1}{\tilde{u}} \frac{\partial^2 \tilde{u}}{\partial \tilde{y}^2} - \frac{1}{\tilde{u}} \frac{\partial \overline{\tilde{u}' \tilde{v}'}}{\partial \tilde{y}} - \frac{\tilde{v}}{\tilde{u}} \frac{\partial \tilde{u}}{\partial \tilde{y}} \tag{2.28}$$

The four terms influencing the change of velocity in the streamwise direction can be evaluated to identify their relative influence. For the case of a turbulent boundary layer in an adverse pressure gradient leading up to the point of separation, the streamwise velocity will be positive, but its streamwise derivative will be negative.

The freestream velocity gradient term will be negative, leading to a reduction in the local velocity within the boundary layer. This is the dominant forcing function causing the velocity to reach zero and the boundary layer to separate.

The viscous stress term is negative throughout the boundary layer. Its magnitude is highest near the wall, then it decays with distance from the wall. A turbulent boundary layer that strictly follows the law of the wall would have uniform viscous shear stress throughout the linear velocity profile of the viscous sublayer. Therefore the magnitude of the second term in the right-hand side of equation 2.28, which represents the first derivative of the viscous shear stress, will have a maximum magnitude somewhere outside of the viscous sublayer. This maximum will occur in the buffer layer, as the term transitions from zero in the viscous sublayer to scaling with $-1/y^2$ in the log layer. Both the slowing down of the freestream and the viscous shear stress act to reduce the streamwise velocity, which brings the boundary layer closer to the point of separation.

The third term on the right-hand side of equation 2.28 comes from the turbulent mixing within the boundary layer. The Reynolds shear stress $\overline{u'v'}$ typically has a negative value throughout the boundary layer. This comes from events in which a parcel of fluid with a higher than average streamwise velocity is perturbed up or down within the boundary layer by a fluctuation in the wall-normal velocity. The negative value means that the parcel of higher velocity fluid is statistically more likely to be perturbed downward towards the wall. This is consistent with the concept of the turbulent fluctuation acting like a vortex within the boundary layer. A vortex with the same sign of vorticity as the average velocity profile would have a negatively valued instantaneous $u'v'$. This turbulent mixing of higher velocity fluid towards the wall is the mechanism by which a turbulent boundary layer delays separation when compared to a laminar boundary layer.

The Reynolds shear stress typically is zero-valued at the wall, increasing in magnitude moving away from the wall in the near-wall region, then decays back to zero in the freestream. At positions below the location of minimum Reynolds shear stress, its derivative is negative. At positions further from the wall than the location of minimum Reynolds shear stress, the derivative is positive. This means that the turbulent mixing acts to reduce the velocity of the fluid away from the wall, while increasing the velocity of the fluid near the wall, as seen by the changing sign of the third term on the right-hand side of equation 2.28. As boundary layer separation occurs as a result of near-wall fluid reaching zero velocity, the Reynolds shear stress acts to delay turbulent boundary layer separation.

The fourth term on the right-hand side of equation 2.28 represents a mean wall-normal velocity that convects higher velocity fluid towards the wall or away from it. As the sign of the vertical gradient of steamwise velocity, $\partial u/\partial y$, is positive, the influence of this term depends on the sign of

the mean wall-normal velocity. In a typical flat plate boundary layer, the mean wall-normal velocity can be shown to be slightly positive based on mass conservation within the boundary layer. For cases such as the backward facing ramp in this investigation, a slight mean negative wall-normal velocity in the freestream upstream of the ramp can lead to a low magnitude negative mean wall-normal velocity within the boundary layer. Therefore the fourth term is able to either increase or decrease the streamwise velocity in the boundary layer.

In the case being studied, of the four terms on the right-hand side of equation 2.28, the first two terms (coming from the freestream velocity gradient and the viscous shear stress) always act to slow down the fluid in the the near-wall region. The third term (coming from the Reynolds shear stress) acts to counteract the first two mechanisms, speeding up the fluid near the wall. The final term, resulting from wall-normal mean convection, is typically low magnitude and can either speed up or slow down the fluid near the wall. The balance between these four terms determines when the boundary layer separates. It is expected that the presence of an SHS will modify both the viscous stress term and the Reynolds stress term, reducing the magnitude of both. The extent to which each is modified will determine if the boundary layer separation is hastened or delayed.

Chapter 3

Experimental Setup

3.1 Water Tunnel

A custom recirculating flow loop, or water tunnel, was designed and constructed at UC Berkeley within Etcheverry Hall in order to enable experimental studies of turbulent boundary layers over superhydrophobic surfaces. The design was guided by reports on the design of comparable water tunnels [21][22], as well as the requirements of the study.

Flow Loop Sizing

The cross-section of the test section is $(152\ \text{mm})^2$. The flow area reduces to 152 mm by 102 mm in order to allow for a contoured backward facing ramp on which to study turbulent boundary layer separation. The development length prior to the separation was selected to be approximately 1 m, based on physical space constraints. In order to ensure a fully turbulent boundary layer entering the backward facing ramp, the selected design target was $Re_x = Ux/\nu \approx 5 * 10^6$ to $1 * 10^7$. With the viscosity of water at room temperature nominally $\nu \approx 1 * 10^{-6}\ m^2/s$, the targeted velocity becomes $U \approx 5$ to $10\ m/s$. The resulting estimate for turbulent boundary layer thickness (based on a $\frac{1}{7}$ power law profile[13]) at the $5m/s$ design point takes the form:

$$\delta \approx \frac{0.16x}{{Re_x}^{1/7}} \approx 18mm$$

Integrating the $\frac{1}{7}$ power law velocity profile gives an estimate for the displacement thickness of one eight of boundary layer thickness as follows:

$$\delta^* \approx \int_0^\delta 1 - \frac{u}{U_\infty} dy \approx \int_0^\delta 1 - \left(\frac{y}{\delta}\right)^{\frac{1}{7}} dy = \frac{\delta}{8} \approx 2.2mm$$

This displacement thickness, assumed to be applied to all four walls of the test section, translates to a test section blockage of approximately 7% in a 152 mm by 102 mm cross-section. The corresponding volumetric flow rate at the 5 m/s design point is approximately 0.078 m^3/s, or 1230

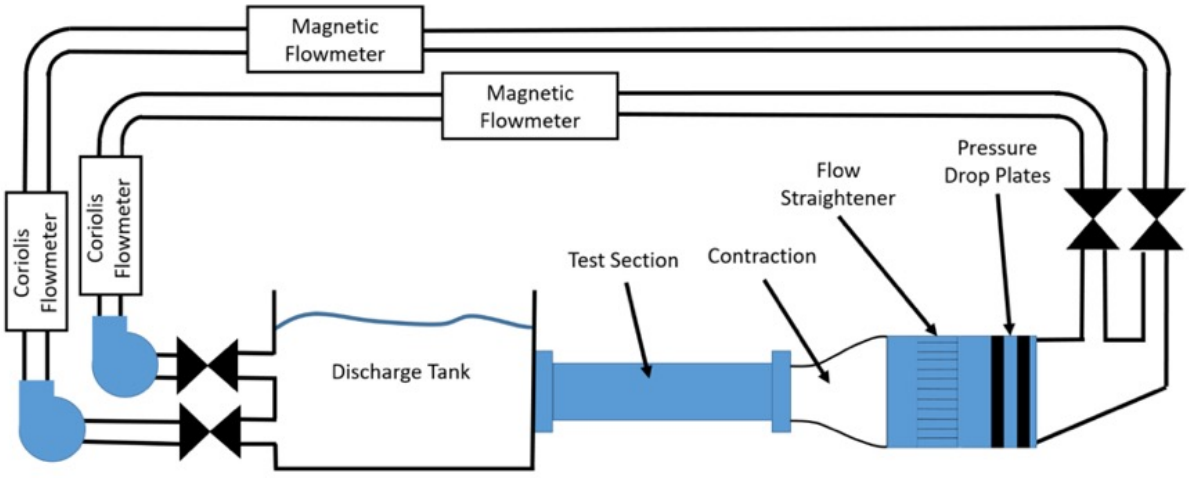

Figure 3.1: This schematic of the flow loop shows the two parallel flow paths that combine upstream of the test section. Valves allow each line to be isolated during the priming process, during which air is released through vent valves located between the Coriolis-type flow meters and the magnetic flow meters. Special thanks is due to Clayton Pelzer who helped build the flow loop and created this figure.

GPM. This level of blockage was determined to be an adequate balance to achieve flows at the desired range of Reynolds number without requiring excessive volumetric flow rate. The system components were subsequently selected assuming an operating point between 1000 and 1500 GPM.

Flow Loop System Layout

In order to achieve the target range of flow rates, a pair of identical centrifugal pumps were selected to operate in parallel. They are capable of pumping 750 GPM each at their peak efficiency operating point, and up to approximately 1000 GPM each if paired with a low restriction system. Therefore the system is designed to have two parallel flow paths that combine at the flow conditioner upstream of the test section. A schematic of the system is shown in figure 3.1.

The two pumps pull water from a large, custom-built, open-topped, stainless steel discharge tank, shown in figure 3.2. The internal dimensions of the tank are nominally 1.54 m (60.5") long, by 1.21 m (47.5") wide, by 1.08 m (42.5") tall, with a step in its floor to accommodate an optical table on which the test section is mounted. Accounting for the step in the floor and that the open-topped tank cannot be filled to the top edge, the volume of the tank is approximately 1600 liters. The tank is constructed from laser cut 3.2 mm (0.125") thick 304L stainless steel sheet. The sheet for each wall is bolted to a frame made from stainless steel angle stock. The wall subassemblies are bolted together to form the tank. It is sealed with 3M 5200 Marine Adhesive Sealant.

Figure 3.2: The stainless steel discharge tank assembled in place, prior to being sealed. Water enters from the test section through the hole on the right side of the figure. The two holes at the bottom left are outlets that lead to the suction side of the pumps.

Figure 3.3: The Coriolis flow meters are mounted vertically in line with the outlet of the pumps.

The water exits the side of the tank through two 102 mm (4" nominal) diameter PVC pipes and is routed to the suction end of the centrifugal pumps. Each pipe has a gate valve used during the system priming process. The water exits vertically from the top of the pumps through a 76 mm (3" nominal) flexible coupling and passes through two Coriolis style flow meters with DIN 80 (3" nominal) pipe flanges. After the Coriolis flow meters, the pipe is expanded from 3" to 4" diameter and turned to be horizontal. This horizontal pipe section is the high point in the system and there is a tee with a valve for releasing trapped air. This location is approximately 3 m off the ground.

The water is then routed through two 102 mm (4" nominal) flexible PVC hoses across the room to the wall above the test section. It passes through two parallel assemblies, each consisting of a magnetic flow meter with 4" pipe flanges bolted to straight development lengths of 102 mm (4" nominal) PVC pipe upstream and downstream. Another pair of 102 mm (4" nominal) PVC hoses route the flow to the flow conditioner assembly.

The flow conditioner assembly combines the water being pumped through two 102 mm (4" nominal) hoses and conditions it to enter the test section as a nominally uniform parallel flow. The external shell of the assembly consists of a 460 mm (18" nominal) diameter stainless steel pipe approximately 914 mm (36") long. Welded to the flange on the inlet end of the assembly are

Figure 3.4: The magnetic flow meters are mounted horizontally, cantilevered from the wall above the optical table.

two 102 mm (4" nominal) stainless steel ball valves mounted on elbows of 102 mm (4" nominal) stainless steel pipe. The water enters vertically through the valves, which are used during the system priming process to isolate the hoses. The water then turns through the elbows to enter the tank as two 102 mm (4") diameter jets. The external shell, shown in figure 3.5 during the installation process, contains a single flow conditioning insert, shown in figure 3.6.

The jets entering the contraction tank immediately impinge directly onto the first of two perforated stainless steel plates, intended to break up the jets. The plates are 3 mm (0.12" nominal) thick and have holes of 4.8 mm (0.1875") diameter, with a staggered spacing of 7.9 mm (0.3125"). The perforated plates are cut to a circular pattern to fit within the inner diameter of the 18" stainless steel pipe. They are spaced approximately 5 cm apart. Another 5 cm downstream of the perforated plates, the flow passes through a stainless steel honeycomb. The honeycomb is made from 0.16 mm thick 304 stainless steel foil, spot welded to form a 60 mm thick honeycomb pattern with 6.4 mm cells. The honeycomb is cut to fill the inner diameter of the 460 mm stainless steel pipe, but masked on both sides to only allow flow through an approximately 305 mm by 305 mm (12" by 12") square. Exiting the honeycomb, the flow enters a 305 mm by 305 mm (12" by 12") settling chamber, approximately 295 mm (11.5825") long in the streamwise direction. After the settling

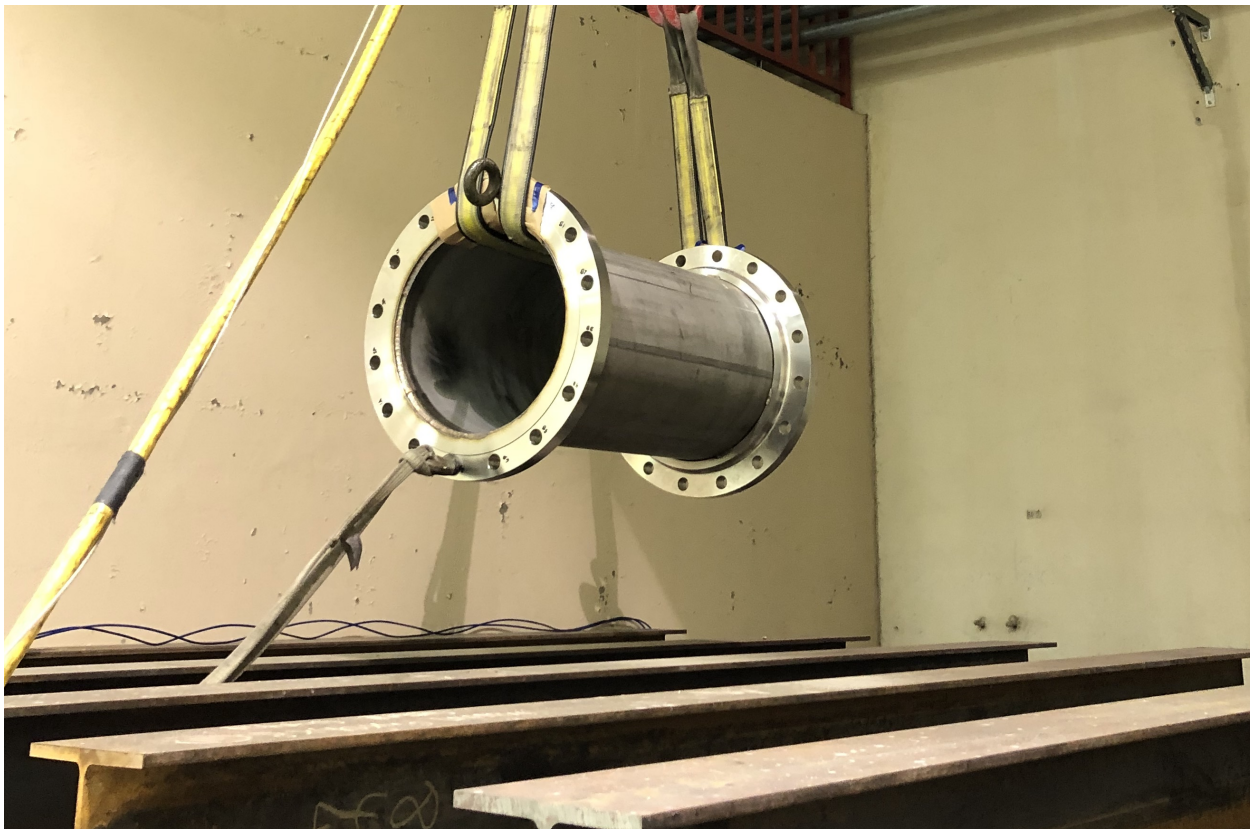

Figure 3.5: The contraction tank was lifted over the concrete x-ray containment wall into the lab space using the overhead gantry crane.

chamber, the flow enters the a contraction that smoothly reduces the flow area from a 305 mm by 305 mm (12" by 12") square with chamfered corners to the 152 mm by 152 mm (6" by 6") square cross-section of the test section. The contraction follows a 5^{th}-order polynomial profile, with the contraction occurring over a 406mm (16") streamwise distance.

The contraction is constructed from 3D printed ABS plastic, shown in figure 3.7. This is bolted to a frame constructed from stainless steel angle that mounts the perforated plates and honeycomb, as well as carries the load on the contraction. The 3D printed contraction is overlaid with fiberglass fiber reinforced epoxy. This provides strength to the shell of the contraction. The excess space between the contraction and the wall of the 460 mm pipe is filled with waterproof closed cell polyurethane expanding foam. The entire flow conditioning assembly inserts into the 460 mm pipe and is held in place by set screws.

The test section is constructed from 25mm (1" nominal) thick cast acrylic sheet. The flow area is 152 mm by 152 mm (6" by 6"), with standard 8" pipe flanges on both ends. Both sides of the test section are clear for optical access. The top and bottom of the test section have removable

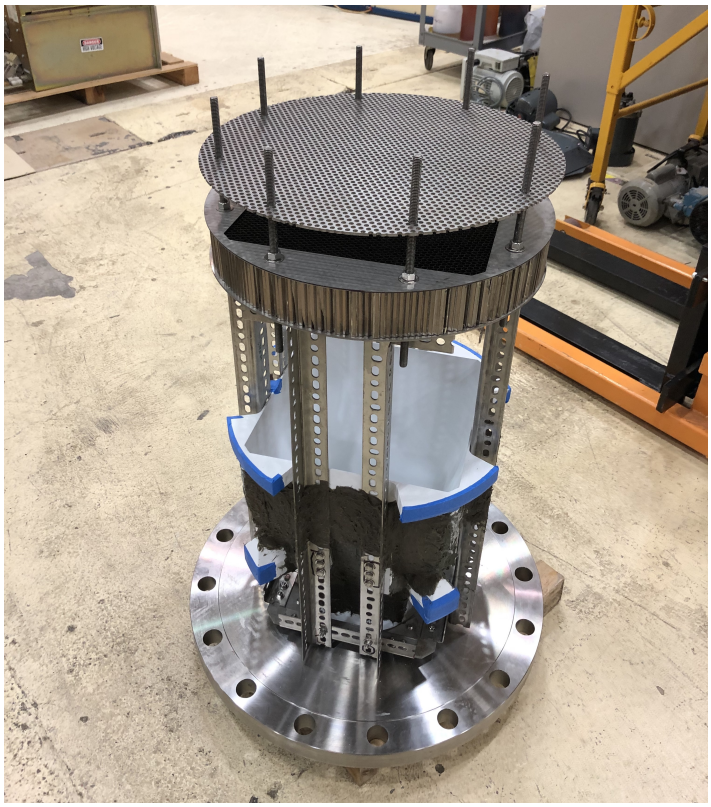

Figure 3.6: The flow conditioning insert consists of (from top to bottom) two perforated stainless steel plates (only one shown), a honeycomb, a settling chamber (walls not shown) and a 4:1 3D printed contraction. The assembly is supported by a stainless steel frame. Shown during a fit check, it is sitting atop the stainless steel flange that is used to cap the outlet end of the contraction tank.

windows. The window on the floor of the test section is made from cast acrylic and sealed with an o-ring. The roof of the test section has two interchangeable configurations constructed from Mic 6 aluminum. The flat plate configuration maintains the 152mm by 152mm flow area and is used for studying boundary layers over injected air layers. The boundary layer separation configuration reduces the flow area to 152 mm by 102 mm (6" by 4") leading up to a backward facing ramp from which the boundary layer separates.

The outlet of the test section discharges directly into the open-topped tank. The jet into the tank is deflected downward and broken up by a sheet of perforated aluminum. This is intended to dissipate the energy of the jet and minimize the magnitude of waves on the free surface of the discharge tank. The jet break-up device is shown in figure 3.9.

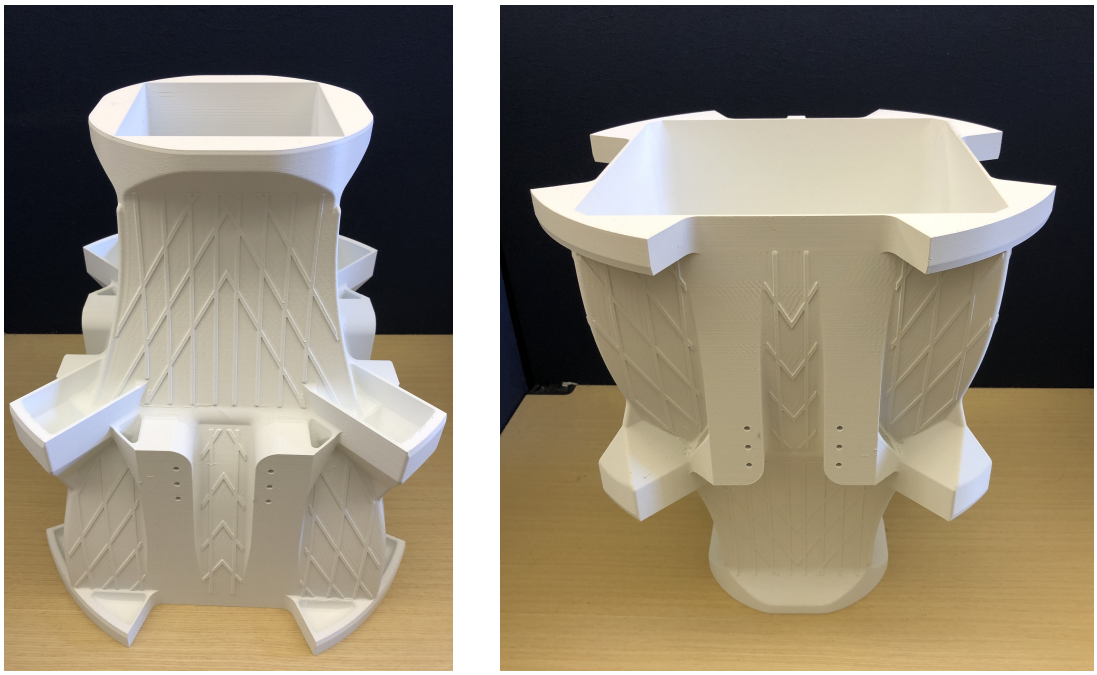

Figure 3.7: The contraction was 3D printed from ABS plastic using fused deposition modeling (FDM). It includes features for aligning within the contraction tank, bolting to the support frame, and adhering to a fiberglass reinforced epoxy overlay used for strengthening the shell.

Flow Rate Measurement and Control

The water is pumped through the system by two Goulds model 23SH2Q45H0 centrifugal pumps. The pumps have 4 inch pipe flange inlets, 3 inch pipe flange outlets, and casings for up to 8 inch diameter impellers. The impellers are trimmed to $6\frac{7}{8}$ inch diameter. The impeller and casings are made of 316 stainless steel. They are paired to 22 kW (30 HP) totally enclosed, fan-cooled electric motors. The pumps are driven by two independently controlled variable frequency drives (VFDs). The VFDs are Rockwell Automation 750-series AC drives operating at 460 VAC. They control the speed of the pump by varying the frequency of the 3-phase alternating current through the pump, via a closed-loop frequency control strategy. The steady state rotational speed of the pumps is directly proportional to the AC frequency applied. The flow rate within the system is a resultant function of the pump speed and the system head loss curve.

The flow rate is measured in two ways in each of the two parallel flow paths coming from the pumps. A Coriolis-type mass flow meter is mounted in line with the outlet of each of the pumps. They are Endress & Hauser Proline Promass 83 model flow meters rated to measure mass flow rates up to 3000 kg/min, or just under 800 GPM at nominal density. A Rosemount model 8705 magnetic flow meter is mounted in each line approximately mid way between the pumps and the flow conditioner assembly. These are each rated to measure volumetric flow rates up to 1000 GPM.

Figure 3.8: The assembled contraction tank includes two 102 mm (4" nominal) ball valves used to isolate the upper section of the flow loop during system priming.

3.2 Flow Loop Commissioning & Characterization

While commissioning the newly constructed flow loop several aspects of the operation were investigated. A preliminary leak check revealed several locations of leaks that needed to be addressed. The most serious leak was coming from the pump casing seal on both pumps. The stamped stainless steel casing was incorrectly stamped at the factory with two small darts in the area of the casing o-ring seal. These features allowed water to leak past the o-ring and accumulate on the floor of the lab. To address this issue, the pump heads were disassembled and the indentations were packed with Dow Corning High Vacuum Grease. This prevented water from leaking from the pump heads. However, due to the unknown pressure limit at which the water would be able to leak past the vacuum grease, the operating frequency of the pumps was limited to less than 40 Hz.

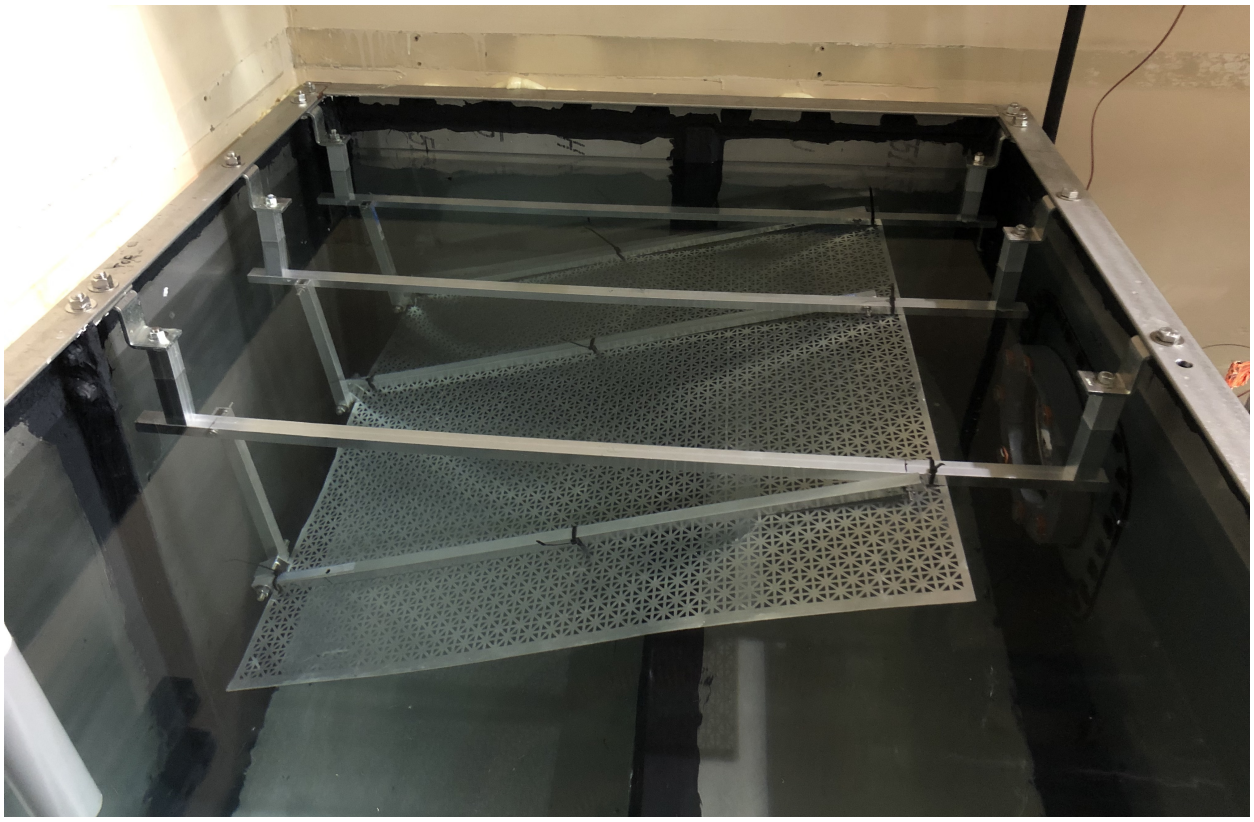

Figure 3.9: The perforated aluminum sheet mounted in the discharge tank is intended to break up the jet exiting the test section and reduce free surface disturbances.

Flow Loop Operating Conditions

Upon completion of all leak checks, the range of possible flow rates was investigated. Prior to operating the pumps it was unknown what flow rates could be achieved, as there was a lot of uncertainty in design estimates of the minor losses within the system. This was especially true for the flow conditioning features. Table 3.1 shows the measured flow rates at a range of pump operating frequencies. The combined flow rate from the two pumps was used to calculate the bulk velocity based on the cross-sectional area of the test section in the boundary layer separation configuration. Due to the pump speed being limited in order to avoid causing leaks from the pump casings, the maximum flow rate observed is slightly less than targeted flow rate range of 1000 to 1500 GPM. However, the range of flow rates achieved was sufficient for the geometry used in this study. An extrapolation of the data suggests that a permanent solution to the potential pump leaks would enable the flow loop to achieve a flow rate on the order of 1700 GPM at the standard operating frequency of 60 Hz.

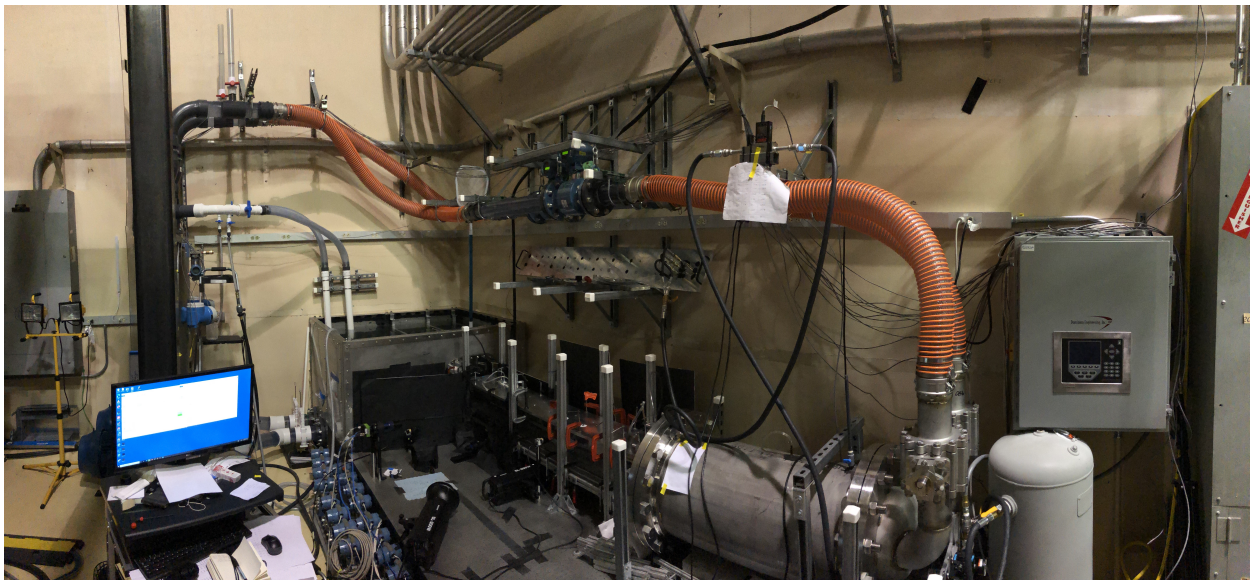

Figure 3.10: The completed flow loop was operated up to a combined flowrate of approximately 1000 GPM during preliminary testing.

VFD Frequency Setting $[Hz]$	Pump 1 Flow Rate $[GPM]$	Pump 2 Flow Rate $[GPM]$	Combined Flow Rate $[GPM]$	Computed Test Section Bulk Velocity $[m/s]$	$Re_H * 10^{-5}$ $[-]$
5	67	65	132	0.54	0.55
7	94	93	187	0.76	0.78
10	136	134	270	1.10	1.12
13	177	177	354	1.44	1.47
15	206	205	411	1.67	1.71
17	234	234	468	1.90	1.94
20	277	277	554	2.25	2.30
23	320	321	641	2.61	2.66
25	349	349	698	2.84	2.90
27	378	379	757	3.08	3.14
30	421	423	844	3.43	3.50
35	493	495	988	4.02	4.10

Table 3.1: Measured volumetric flow rates over a range of pump frequencies with 152 mm by 102 mm test section installed. The Reynolds number is based on the channel height of 102 mm and the nominal viscosity of 10^{-6} m^2/s. Data was collected with both pumps operating at the same frequency.

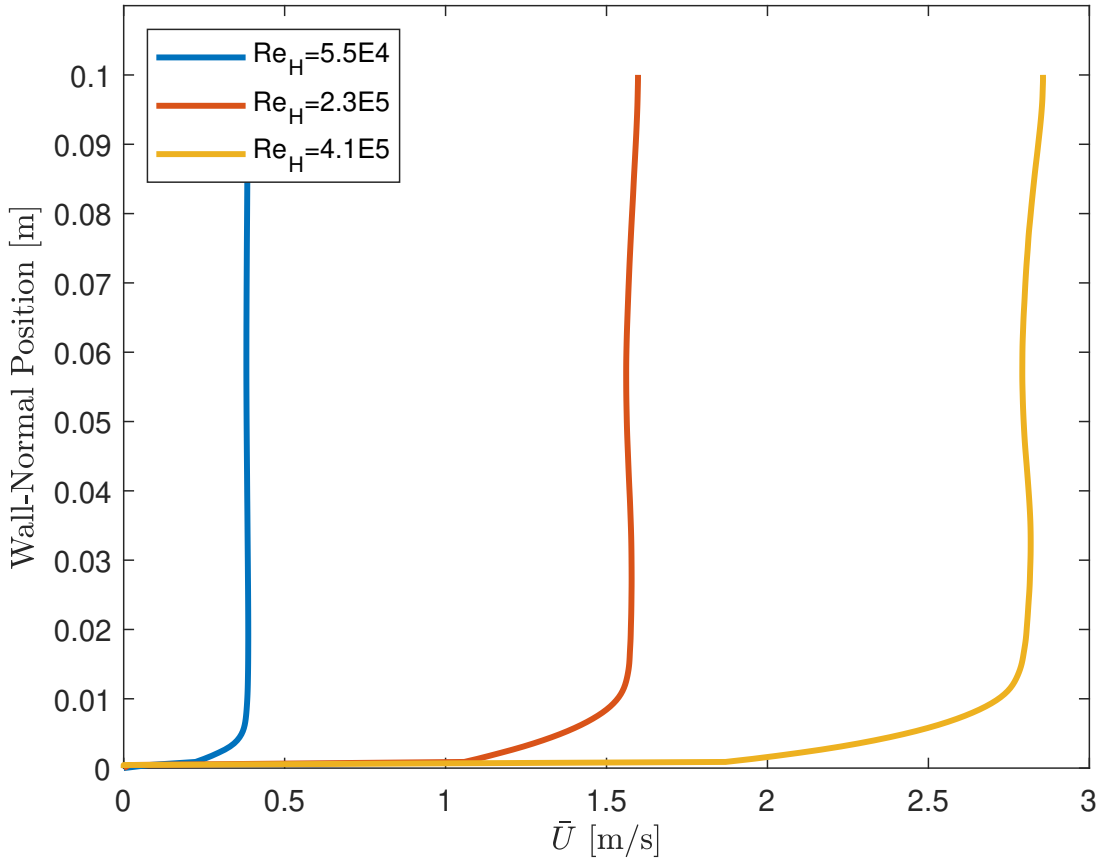

Figure 3.11: The flow conditions were measured at the inlet of the test section in the full 152 mm by 152 mm configuration. The mean velocities are shown as a function of distance from the roof of the test section for three flow rates. The data is based on PIV from 500 image pairs.

Test Section Inlet Characterization

The performance of the flow conditioner was evaluated via particle image velocimetry at the entrance of the test section. Performed with the test section in the flat plate configuration, the velocity field was measured within a vertical plane located nominally on the centerline of the test section approximately three channel heights downstream of the contraction. An ensemble of 500 image pairs was collected at three nominal flowrates. The mean velocity profiles (shown in figure 3.11) and freestream turbulence intensities of less than 0.6% (shown in figure 3.12) indicate that the inlet flow is adequately conditioned.

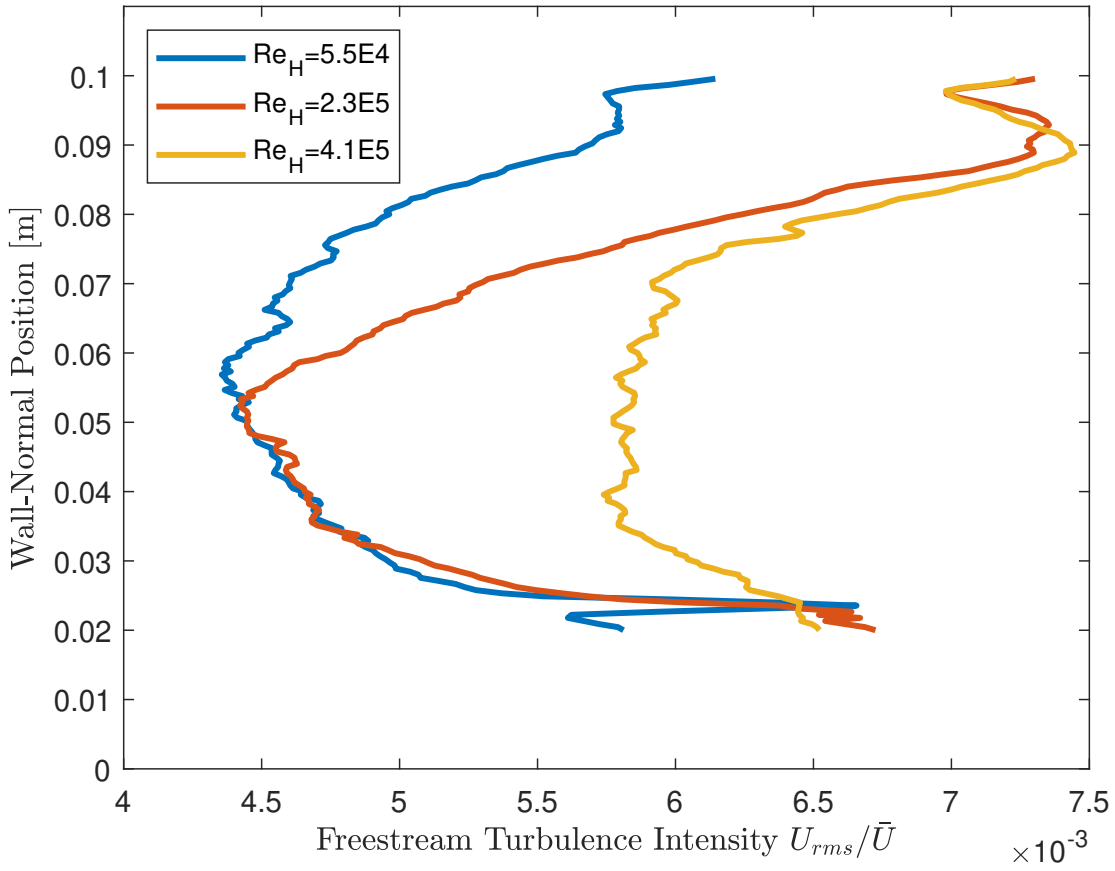

Figure 3.12: The inlet turbulence intensity was calculated from PIV results based on 500 image pairs at three separate flow rates. It is plotted as a function of distance from the roof of the 152 mm by 152 mm test section. Note that the turbulence intensity remains below 0.6% near the centerline of the test section, indicating acceptable flow conditioning.

3.3 Particle Image Velocimetry Setup

The setup for particle image velocimetry (PIV) consists of a laser and light sheet optics for illuminating the flow, tracer particles to indicate the motion of the fluid, and a camera system for capturing images.

Laser and Light Sheet

A Quantel Evergreen 200 Nd:YAG double pulsed laser is used to illuminate the flow. It utilizes two independently triggered laser cavities to create a pair of 200 mJ pulses with a pulse width of approximately 7.5 ns. The repetition rate can be adjusted up to 15 Hz. The beam has a nominal diameter of 6 mm. The path of the laser is shown in figure 3.13

The laser fires down the length of the optical table, parallel with the flow. The beam is reflected off a turning mirror to pass through light sheet optics. The iLA 5150 LSO light sheet optics create an expanding light sheet that is expanding at a divergence angle of 50° while the sheet thins to a focus line a few centimeters beyond the surface of interest. The expanding light sheet exits the sheet optics in the horizontal plane, then reflects off a second turning mirror to shine into the test section as a vertical plane located approximately at the centerline of the test section. The light sheet was measured at the roof of the test section to be approximately 2 mm thick at the center of the fan, and approximately 0.5 mm thick at a location approximately 8 cm downstream. These measurements were based on traces left on burn paper. The light sheet can be seen in figure 3.14.

Tracer Particles

The water in the flow loop was seeded in bulk with tracer particles. Potters Sphericel® 110P8 hollow fused borosilicate glass microspheres were used as tracer particles. The density of the particles is 1.10 g/cm^3 and the nominal diameter is 10 μm. The resulting particle response time constant in room temperature water is estimated as follows:

$$\tau_p = d_p^2 \frac{\rho_p}{18\mu} \approx 6\mu sec$$

The time constant of the boundary layer was estimated to be the ratio between the characteristic length scale and the characteristic velocity of the flow.[23] The conventional choice for a turbulent boundary layer of the boundary layer thickness and the freestream velocity leads to a range of flow time constants from 0.005 to 0.05 seconds for the range of flowrates that were investigated. The Stokes number is the ratio between the particle response time constant and the time constant of the flow as follows:

$$Stk = \frac{\tau_p}{\tau_f}$$

A Stokes number of much less than 0.1 indicates that a particle will faithfully follow the motion of the surrounding flow. The Stokes number is estimated to be on the order of 10^{-4} to 10^{-3} for the flowrates investigated, indicating that the particles are faithful tracers.

Figure 3.13: The laser system and laser path can be seen above. The pulse generator is located in the lower right corner of the image. The laser head seen just above the pulse generator sends the laser beam down the length of the optical table, off a turning mirror, through the light sheet optics, and off a second turning mirror to enter the test section as a vertical sheet. The PIV cameras can be seen mounted at the left edge of the optical table approximately in line with the light sheet optics.

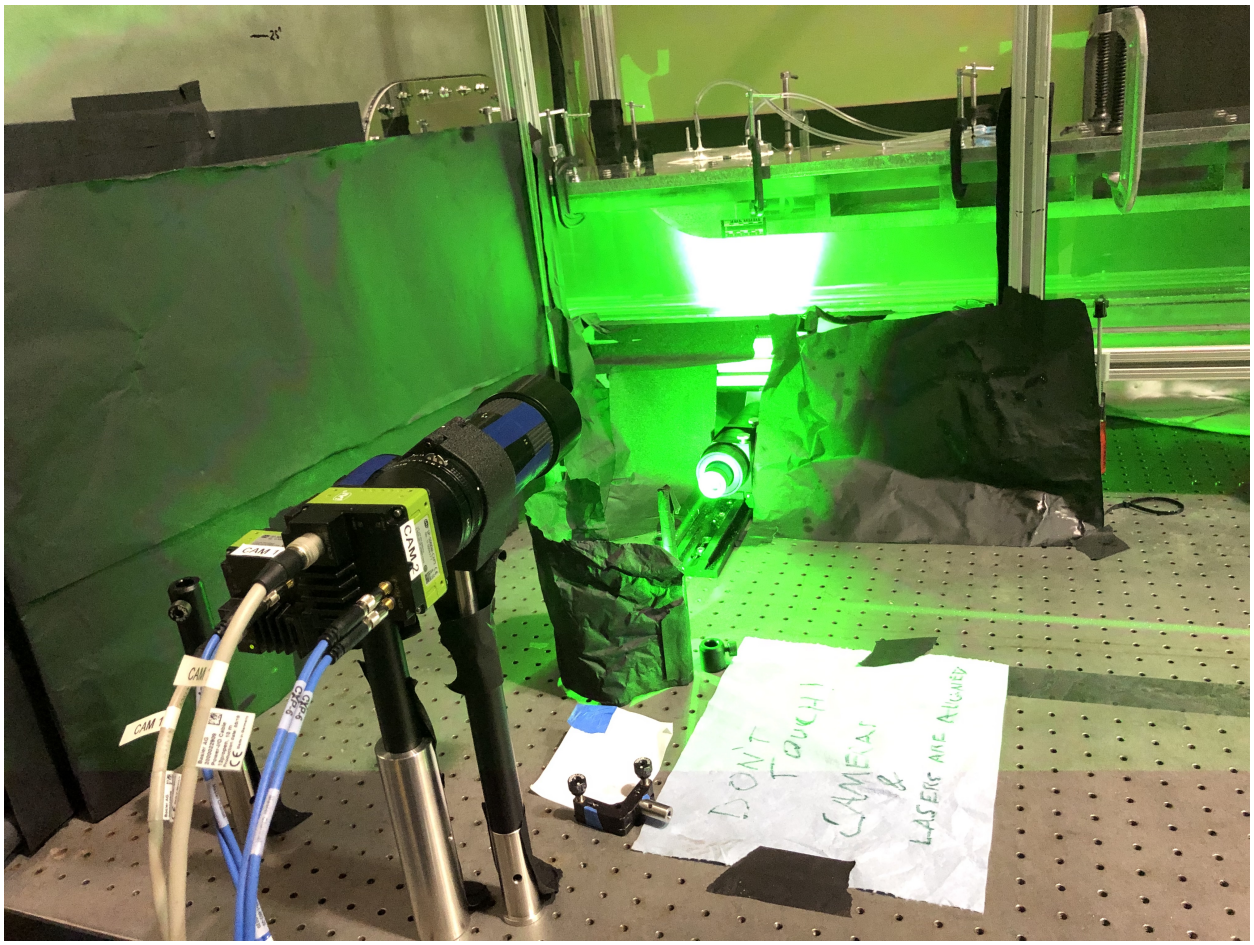

Figure 3.14: The laser sheet is shown from the point of view behind the PIV cameras.

Camera System

The camera system used consists of two JAI SP-5000M-CXP2 cameras linked to a Euresys Coaxlink Quad CXP-12 framegrabber PCI card installed in a HP Z840 workstation. The cameras and laser timing are controlled relative to each other by precise triggering from a Quantum Composers 9520 Series pulse generator. The cameras record 5.2MP 12-bit grayscale images. When operating in PIV mode, they record two images in quick succession in response to a single trigger pulse. The particles in the image are effectively frozen by the short duration of the laser pulse, which is triggered by the pulse generator to occur once during each of the two camera exposures. The images from the cameras are processed to compute velocities using LaVision DaVis 8.4.0 software.

3.4 Geometry

The test geometry used for boundary layer separation studies consists of a single 19 mm thick sheet of Mic 6 aluminum, nominally 990.6 mm long and 151.1 mm wide. This surface is mounted to the removable roof of the test section such that the flat surface is nominally 102 mm above the floor of the test section. Upstream of this plate is a 3D-printed ABS ramp that follows a 5^{th}-order polynomial contour to smoothly transition between the full 152 mm test section height to the 102 mm height. The 5^{th}-order polynomial transitions the 50 mm height change over a 266 mm streamwise distance. Downstream of the aluminum plate is a constant 127 mm radius contoured backward facing ramp. This constant radius geometry, inspired by the work of Song et al.[9], provides a progressively more adverse pressure gradient, allowing the location of separation to move up and down the ramp depending on the robustness of the boundary layer. A 3D-printed ABS ramp was used for preliminary investigations. It was replaced by CNC machined 6061 aluminum geometry for the final round of investigations. The test section geometry is shown in figure 3.15. The equation for the roof height (in millimeters) relative to the floor of the test section is given in equations 3.1 through 3.5. The x coordinate (in millimeters) is measured from the leading edge of the flat aluminum plate. Note that $x = -481$ mm is location where the 4:1 contraction entering the test section ends, and $x = 1420$ mm is the location where the test section discharges into the discharge tank.

$$H = 152; [-481 < x < -298] \tag{3.1}$$

$$H = 152 - 50\left[6\left(\frac{x+298}{266}\right)^5 - 15\left(\frac{x+298}{266}\right)^4 + 10\left(\frac{x+298}{266}\right)^3\right]; [-298 < x < -32] \tag{3.2}$$

$$H = 102; [-32 < x < 1010] \tag{3.3}$$

$$H = 102 + 127 - \sqrt{127^2 - (x-1010)^2}; [1010 < x < 1111] \tag{3.4}$$

$$H = 152; [1111 < x < 1420] \tag{3.5}$$

3.5 Coatings

Several coatings were tested to identify a surface that performed adequately to complete the study. Preliminary PIV studies demonstrated that the bare aluminum surface was too reflective to achieve clear images of the particles near the wall. Therefore a matte black paint was used to reduce the reflectivity of both the flat aluminum plate and the backward face ramp geometry. All of the baseline data sets were collected on matte black painted surfaces.

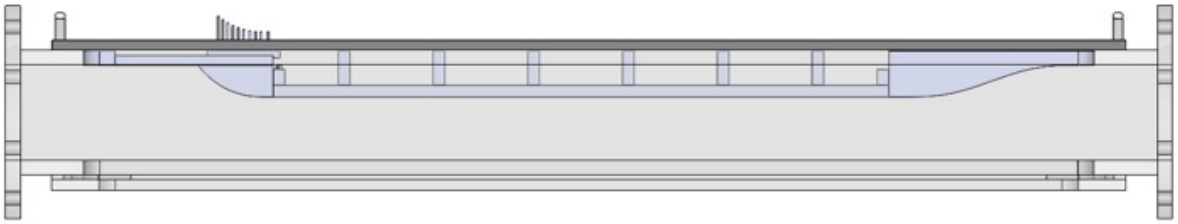

Figure 3.15: The test geometry includes a flat plate mounted to the roof of the test section. As the water (flowing from right to left) reaches the end of the flat plate, the boundary layer separation is studied on the constant radius backward facing ramp.

Two different commercially available superhydrophobic coatings underwent preliminary testing. Rust-Oleum NeverWet® is a two-part superhydrophobic coating system available as a set of aerosol containers. The first part consists of micron scale hydrophobic particles in an acrylic-based polymer solution. After the first coat is applied and partially dry, the second part is applied which consists of nanometer scale hydrophobic particles mixed with ethanol which acts as a solvent. Upon application the ethanol partially melts the polymer substrate before evaporating, allowing the nano scale particles to become embedded in the top layer of the substrate, creating a hierarchical structure of micro and nano scale features that is characteristic of a robust superhydrophobic surface.[24]

The second superhydrophobic coating tested was Nasiol® SHBC, a similar two-part coating. Sold in liquid form, it is recommended to be applied using a high volume, low pressure (HVLP) type spray gun. Upon application, the Nasiol® coating failed to adequately adhere to the aluminum surface. The coating shrank significantly during the drying process, resulting in delamination starting where it pulled back at the edges of the aluminum plate. When exposed to the flow, the coating began peeling off of the aluminum as a continuous sheet within the first 15 minutes of testing, at a bulk velocity of approximately 1.7 m/s (corresponding to a pump speed of 15 Hz). Future work must be done in an attempt to modify the application process in hopes of improving the adhesion between Nasiol® SHBC and the aluminum plate. Currently, no boundary layer results using the Nasiol® coating are being reported.

Chapter 4

Methodology

The goal of this project was to investigate the influence of superhydrophobic surfaces on turbulent boundary layer separation. In order to achieve that end, a direct A-B comparison was performed between a baseline coating and a superhydrophobic coating. The coatings were applied to the same aluminum geometry and tested over the same range of flow conditions. In order to compare the cases, several categories of measurement were required: characterization of the coatings, measurement of the bulk properties of the flow, and detailed measurement of velocity fields within the region of interest.

4.1 Coating Characterization

The coatings were applied to the 990 mm long flat plate and the backward facing ramp. After the coatings were dry, the roughness and contact angles were recorded.

Coating Application

The coatings were applied to the 990 mm long flat plate and the backward facing ramp. The plate and the ramp were removed from the roof as a subassembly. After being masked along to edges, they were spray coated with the appropriate coating. After the coating was dry and surface properties were tested, the flat plate and ramp subassembly were bolted to the roof of the test section and reinstalled in the flow loop.

The NeverWet coating was applied to the flat plate and the backward facing ramp following the manufacturer's instructions supplied with the aerosol cans. The bare aluminum was cleaned with acetone, then soap and water, to prepare for the coatings to be applied. The first coat of the base coating (or part A) was sprayed onto the surface with slightly overlapping spray passes oriented approximately 45° from the long axis of the flat plate. After allowing the first coat to briefly dry for between 30 to 60 seconds, a second coat of the base coating was applied in a similar manner, but with the overlapping spray pattern oriented approximately perpendicular to the original spray pattern. After allowing the base coating to dry for between 30 and 45 minutes, the same application process

of two sequential spray patterns was repeated using the top coat (or part B) spray. The surface was allowed to dry for at least twelve hours before being tested for roughness or contact angle. It was observed that the timing between the application of the base coat and the top coat is an important parameter. The base coat must be dried such that no regions appear to still be liquid before the top coat is applied. Otherwise the liquid base coat will react with the top coat to form a non-uniform coating with an "orange peel" or "cracked earth" type of texture. However the base coat must not be fully cured at the time the top coat is applied, as the top coat is intended to react with the base coat in order to improve adhesion.

The matte black surface was applied in a similar manner using Rust-Oleum Painter's Touch® 2X Ultra Cover® matte black aerosol spray paint. A flat black primer from the same line of coatings was used to improve adhesion. The primer was applied using the two sequential perpendicular spray patterns and allowed to dry approximately one hour. Then two coats of the matte black paint were applied in a similar manner approximately 30 minutes apart. The paint was allowed to dry for at least twelve hours before being tested for roughness and contact angle.

Surface Roughness

The roughness of the surfaces was measured using a Mitutoyo SJ-210 Portable Surface Roughness Tester. This device operates by dragging a needle-style probe over the surface to record a line profile. The roughness parameters are computed from the line profile. The roughness was recorded in both the longitudal and transverse directions on the flat plate in multiple locations after the coatings were applied. The definitions of the three roughness parameters recorded, in terms of the filtered surface heights, Z_i, relative to the mean surface, are given as follows:

$$R_a = \frac{1}{N}\sum_{i=1}^{i=N}|Z_i| \tag{4.1}$$

$$R_q = \sqrt{\frac{1}{N}\sum_{i=1}^{i=N}{Z_i}^2} \tag{4.2}$$

$$R_z = \frac{1}{5}\sum_{k=1}^{k=5}(Z_{peak} - Z_{valley})_k \tag{4.3}$$

where subset k is a shorter line profile within the total recorded line profile. Z_{peak} and Z_{valley} are the tallest and deepest points within subset k. This means that R_z is the average of the maximum range of measurements in five separate regions of the surface.[25]

Contact Angle

The contact angle between a droplet of tap water and the coating was measured based on an image recorded on a Basler acA2040-55um camera. A small droplet on the order of 10 μL was deposited on the surface using a pipette. The camera was aligned such that the field of view looked across

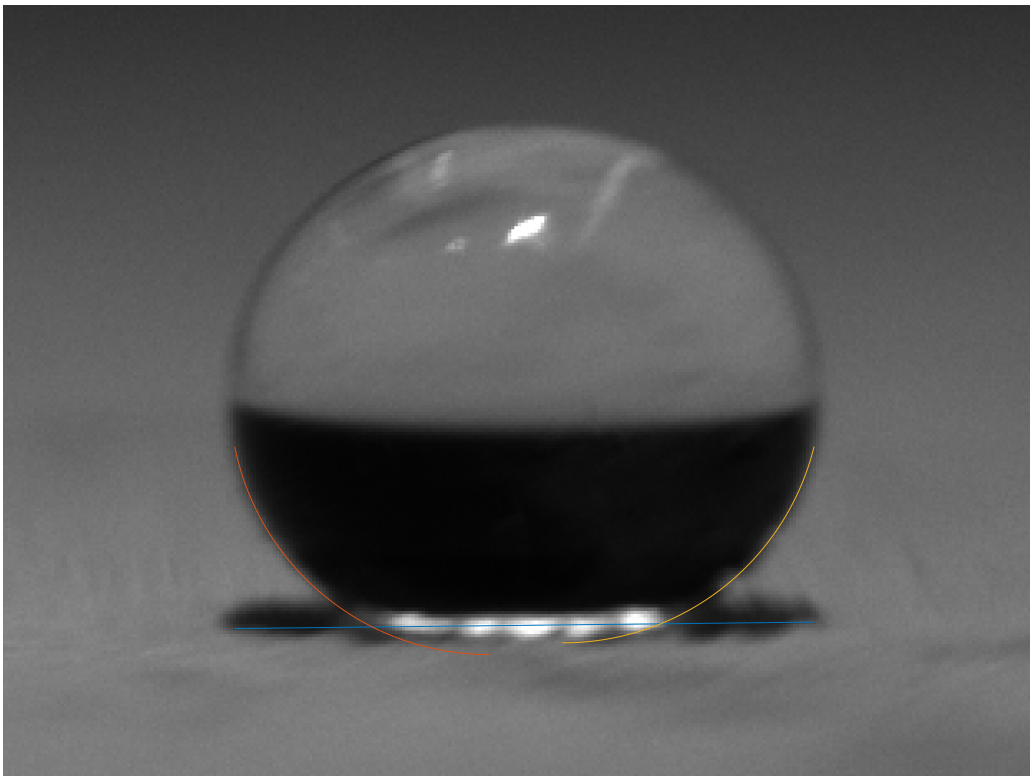

Figure 4.1: The contact angle was computed as the intersection angle between a circle fitted to the edge of the droplet and the contact line with the surface being evaluated. This was applied independently to the left and right side of the droplet. The droplet above was found to have a contact angle of 153° on the left side and 158° on the right side when contacting surface NW2.

the surface of the aluminum plate. The camera was manually focused on the droplet and an image was recorded.

To compute the contact angle, the edge of the droplet was approximated as a circle based on three manually selected points. The interface between the surface and the droplet was represented by a line manually overlaid on the image. The contact angle was computed as the angle at which the circular segment that was fit to the droplet edge crossed the contact line. This was performed on both the left and right side of the droplet. An example of this is shown in figure 4.1.

4.2 Bulk Fluid Quantities

The bulk behavior of the flow loop was recorded in Labview using a CompactRIO system for data acquisition. This included the pump VFD frequencies, flow rates, temperatures at two locations (contraction tank and discharge tank), dissolved oxygen level in the discharge tank, and several pressure transducers used for system diagnostics. All of the signals were averaged over the collection time for the PIV ensemble data for each point.

The flow rate was recorded from both the Coriolis-type flow meter and the magnetic flow meters. As the Coriolis flow meters fundamentally measure mass flow rate and the magnetic flow meters fundamentally measure a volumetric flow rate, the signal from the magnetic flow meter was used to compute the bulk velocity in the test section, eliminating the need for an accurate estimate of density in that calculation.

The viscosity and density were computed from the measured temperature in the contraction tank. A cubic fit was used to interpolate kinematic viscosity, ν, and fluid density, ρ, from reference data published by Kestin et al.[26]. While the Coriolis flow meters are designed to directly measure the viscosity of the water, the measurement was observed to be inconsistent between the two devices, as well as highly dependent on the operating condition of the flow loop. As the lab space did not allow for the manufacturer recommended amount of straight pipe length between the pumps and the Coriolis flow meters, we believe that the error in viscosity comes from the influence of secondary flows within the flow meter caused by the pumps. Therefore the interpolation scheme based on temperature was used to determine viscosity and density of the water.

An Endress & Hauser OxyMax WCOS 41 Dissolved Oxygen sensor was used to measured the dissolved oxygen near the free surface of the water in the discharge tank. The dissolved oxygen was observed to be on the order of 9 to 9.5 mg/L when the tank was freshly filled. The level dropped as low as 2.7 mg/L when the system was left sitting stagnant for an extended period of time allowing the SHS to reach a "fully wetted" state. After air injection was used to re-establish the plastrons on the SHS, the dissolved oxygen was observed to has risen to a level between 6.5 and 7 mg/L. Further work will be needed to quantify the interaction between the dissolved oxygen level and the state of the plastrons.

4.3 Velocity Fields

Two-dimensional velocity fields were computed from particle images based on two separate camera fields of view. A wider field of view, obtained with a 60 mm focal length lens, was used to capture the velocities along the entire length of the backward facing cylindrical ramp. The velocity field from this view was used to determine the location of flow separation. A second camera mounted with a 200 mm focal length lens provided a view of the near-wall region just upstream of the backward facing ramp. Images from this camera were used to determine the velocities in the boundary layer and subsequently compute the parameters of the incoming boundary layer prior to separation. A particle image velocimetry algorithm was applied to ensembles of 1000 image pairs from each

camera in order to determine the mean velocities in the streamwise and wall-normal directions, as well as statistics of the turbulent fluctuations in those velocities.

4.4 Testing Process

The testing process was designed around getting high quality PIV data. The image quality is dependent on the amount of light collected by the camera that is reflected or scattered by the particles, as well as the amount of light scattered from the test surface. A high quality image maximizes the amount of light coming from the particles, while minimizing the amount of light coming from the surface. These are two competing requirements, as increasing the number of particles in the interrogation volume increases the amount of light that is scattered from the particles to the surface. Additionally, the different surfaces, as well as the different states of plastrons on the surface, changed the way in which light was reflected and scattered from the surface. As a result, there was a significant amount of trial and error to get the imaging settings correct prior to collecting each data set.

Preparation for Image Collection

After the lasers were aligned and the cameras were focused on the light sheet, there were three parameters that could be adjusted to try to improve the quality of the PIV images. The first parameter was the laser energy. However we observed that for our optical setup, adjusting the pulse energy did not have a spatially uniform effect on image brightness. The edges of the light sheet were darkened significantly without a significant reduction in the light scattered off of the wall near the center of the light sheet. Therefore the laser was kept at the full energy of 200 mJ per pulse. The other two parameters used to adjust the image quality are the particle seeding density and the aperture of the cameras.

Prior to collecting data for every case, the seeding and camera apertures were adjusted and test data was collected to ensure that the image quality was adequate. First the flow loop would be started up to stir up any particles in the system. A few image pairs were collected and processed with the PIV algorithm to evaluate image quality. An image pair with minimal velocity outliers was considered to be of adequate image quality. Additional seeding would be added to the system as necessary, replacing particles that had settled on the bottom of the discharge tank and were not stirred up by running the flow loop. On the order of 10 to 20 grams of particles were a typical total amount of seeding. An early study found that approximately 30 grams of particles is an upper limit for being able to achieve high quality results.

The apertures of the camera lenses were adjusted to control the amount of light entering the camera. The 200 mm lens was focused at the wall near the center of the laser sheet, where the lighting was more than sufficient. The aperture was closed to reduce the brightness of the light reflecting off of the wall. The lens was set to the smallest aperture at which the light sheet impinging on the wall was recorded as a thin line of saturated pixels. The aperture of the 200 mm lens was

typically F22, though might be adjusted one stop up or down depending on the seeding and the state of the plastrons on the surface.

The field of view of the camera with the 60 mm lens extended all the way to edge of the light sheet downstream of the ramp. As the light sheet thins near its edges, the critical goal was to ensure sufficient lighting at the downstream edge of the ramp. The aperture of the 60 mm lens was opened up until the preliminary PIV results did not show any velocity outliers along the ramp. A larger portion of the upstream region of the wall was typically saturated as a result. The aperture of the 60 mm lens was typically F16, or one stop up or down.

Order of Testing

After adjusting and confirming the seeding and camera settings, the data set for the given case was collected. Ideally, the first data point was a repeat of a previous point at a moderate flow rate. In early cases this would have been around a pump frequency of 20 Hz. However as later cases focused on results at lower flow rates, this initial point typically shifted to a lower pump frequency. Often the last – or second to last – data point of a given case would be a repeat of a data point recorded earlier in the day in an attempt to capture any changes in behavior throughout the day. The order of runs for each surface case is given in table 4.1.

As can be seen from the order of runs, the collection of the early data was based on an attempt to find a consistent trend in behavior. Cases MB2A and MB2B were used to establish baseline data across a range of flow rates. The order of cases on surface NW1 were mainly guided by visual observation of the plastrons on the surface. One theory at the time was that the large plastrons needed to be sheared off by operating at high velocities in order to achieve the desired skin friction reducing effect. This is seen in the order of runs for case NW1D, where the behavior at 20 Hz and 25 Hz was recorded before and after operating at 40 Hz for an extended period of time. It was not until the separation location data was analyzed in more depth that it was identified that the interesting change in separation behavior occurred at lower flow rates. This led to a more methodical approach focused on lower flow rates for the surface NW2. The run order for MB3 focused on repeating baseline data to compare to the data from surface NW2, then filling in additional data at interesting points as time permitted.

4.5 Data Collection Process

The data collection process required operating multiple pieces of equipment simultaneously in order to control the flow loop as well as record multiple formats of data.

Once it was determined that all of the PIV settings were correct during a test run, the first step was to start the Labview file to record the bulk parameters of the system. The start time was manually noted and later used as a reference to align data between different formats. Next the desired pump speeds were set on the VFD control panels. The flow rates were checked on the magnetic flow meter displays, manually recorded in a notebook, and checked against any previous data at the same operating point.

Case	Order of Runs (Pump Frequency Listed)
MB2A	10Hz, 13Hz, 15Hz, 17Hz, 20Hz, 23Hz, 25Hz, 27Hz, (30Hz), (35Hz)
MB2B	30Hz, 35Hz
NW1A	20Hz, 15Hz, 25Hz, 10Hz, 30Hz, 23Hz, 17Hz, 27Hz, 13Hz, 35Hz, (20Hz)
NW1B	30Hz, 35Hz, 20Hz, 10Hz, 15Hz
NW1C	30Hz, (40Hz), 35Hz, 20Hz, 10Hz
NW1D	20Hz, 25Hz, 20Hz, 25Hz, 40Hz, 40Hz, 25Hz, 20Hz
NW2A	20Hz, 15Hz, 10Hz, 13Hz, 17Hz, 20Hz, 23Hz, 25Hz
NW2B	20Hz, 15Hz, 10Hz
NW2C	10Hz, 7Hz, 13Hz, 15Hz, 20Hz
NW2D	7Hz, 10Hz, 11Hz, 12Hz, 13Hz, 15Hz, 17Hz, 20Hz, 23Hz, 25Hz, 10Hz
NW2E	10Hz, 7Hz, 5Hz, 2Hz, 13Hz, 15Hz
NW2F	10Hz, 7Hz, 2Hz, 5Hz, 10Hz, 13Hz, 15Hz
NW2G	10Hz, 7Hz, 8Hz, 9Hz, 11Hz, 12Hz, 13Hz, 14Hz, 15Hz, 16Hz,
(cont.)	10Hz, 15Hz, 20Hz, 25Hz, 10Hz
MB3A	10Hz, 15Hz
MB3B	10Hz, 15Hz, 20Hz, 25Hz, 30Hz, 35Hz, 15Hz, 10Hz, 2Hz
MB3C	25Hz, 24Hz, 23Hz, 22Hz, 21Hz, 20Hz, 19Hz, 18Hz, 17Hz, 16Hz, 15Hz
MB3D	10Hz, 7Hz, 13Hz, 5Hz, 1Hz

Table 4.1: The order of runs for each case. Note that runs listed in parentheses had problems during data acquisition and were not included in results.

Next the laser timing was adjusted on the pulse generator. The timing between the laser flash lamp, Q-switch, and camera trigger for a single laser cavity was kept constant based on the specifications of the laser and cameras. However, the timing between the two laser cavities needed to be adjusted based on the flow rate. The delay between the two laser pulses was set to correspond with the time it would take particles at the bulk velocity to move approximately 12 pixels within the upstream boundary layer camera FOV.

The appropriate laser timing and case number was recorded in the name and folder structure of the image files to be recorded, and the frame grabber software was manually triggered from a command line window. This trigger enabled the framegrabber to recruit RAM for all of the images to be recorded. The typical case of 2000 images required 20 GB of RAM to be preallocated.

Once the framegrabber software indicated that the firmware was ready and the upstream FOV camera was waiting for a trigger, the pulse generator was started, sending a trigger signal to the laser and the camera. The time of the start of recording was manually noted. The pulse generator was programmed to fire the laser 100 times before starting to trigger the camera shutter. This allowed the laser to reach a steady state brightness. The delay between image pairs was set to be 75 msec. Therefore after 7.5 seconds of laser warmup and 75 seconds of recording images the pulse generator was manually stopped. The camera would continue copying the images from RAM to

the hard drive.

Meanwhile the process would be repeated for the wider angle camera with an FOV containing the backward facing ramp. The laser timing was adjusted to correspond to approximately 6 pixels of motion of a particle at the bulk velocity. Due to the wider field of view, this translated to an interframe delay of approximately twice that of the upstream camera. The smaller pixel displacement was selected in part due to the highly three-dimensional nature of the separated flow. In the region of separation, the particles can be quickly carried out of the light sheet by the out of plane velocity. Setting the timing to observe very small particle displacements in the separated region allowed the location of backflow to be identified without losing particles from the light sheet between the two exposures. With the goal of identifying the location of separation, computing the correct direction of the velocity vector is more important than having low relative error for the computed magnitude of very low velocities. The difference in timing between the two FOVs is the reason that the two cameras could not record PIV data simultaneously. The framegrabber was manually triggered via the command line to allocate an additional 20 GB of RAM for the second camera. After the framegrabber software indicated that the camera was ready, the laser was triggered for an additional 82.5 seconds. The time of the start of recording was once again manually noted. In addition to collecting images for PIV, for many of the runs images of the state of the plastrons were record with a Basler acA2040-55um camera before the first PIV recording and again after the second PIV recording. Figure 5.1 provides an example of these images.

This constitutes the process for recording the PIV images for one data point, or one run in table 4.1. The framegrabber software would typically take approximately 12 minutes to copy the images from RAM to the hard drive. This was the limiting factoring in the rate at which data points could be recorded. The pump speed was then adjusted to the next desired operating condition and the process was repeated. This could be repeated 5 or 6 times before all of the 256 GB of RAM on the workstation had been used. As the previously used RAM was left in standby, and the framegrabber software took an order of magnitude longer to recruit standby RAM compared to free RAM, the workstation needed to be rebooted at this point to free up more RAM. After all of the data points were recorded for the case, the Labview recording was stopped and the time was noted.

4.6 Data Processing

PIV Calculations

The PIV preprocessing and calculations were performed in LaVision DaVis 8.4.0 software. The images are saved on the hard drive as 2000 separate 2048 pixel by 2560 pixel images in 16 bit tiff format. The camera sensor records the image at 12 bit depth then the camera maps it to 16 bit during the save process. The aperture adjustment process of saturating the image on the wall that was previous described ensures that the full bit depth of the camera is used.

The first processing step is to sort the images into 1000 pairs of images, with the first image of each pair corresponding to the illumination by the first laser pulse, and the second image of the pair corresponding to the second laser pulse. It is important to process the images separately in this

way, as the two laser pulses come from two separate laser cavities and demonstrate slightly different spatial variation in brightness. The two images within the pair will be referred to as frame 1 and frame 2.

After the images are sorted into 1000 image pairs, a time filter is applied. The time filter subtracts the minimum value recorded within the 1000 images at each pixel location. This is applied separately to the two frames. This removes some of the spatial variations in brightness, such as the setting the saturated surface to zero and reducing the signal of reflections from the opposite wall and scattered light near the wall. As a result, the particles stand out as the brightest pixels.

However the spatial variation in brightness throughout the spreading light sheet was still apparent in the brightness of the particles. To account for this spatial variation, an intensity normalization filter was applied. Within each image, each pixel value was normalized based on the values of the surrounding pixels according to the following:

$$P_{new} = \frac{P_{image} - P_{average}}{P_{st.dev.}}$$

The average and standard deviation were calculated from a surrounding patch with a length scale of 5 pixels. This intensity normalization removed the spatial variation in particle brightness.

The built-in PIV algorithm was applied to the resulting preprocessed image pairs. The algorithm had two additional preprocessing steps built in that were found to be insufficient spatial filters, leading to the aforementioned intensity normalization. The algorithm subtracted a sliding background with a length scale of 8 pixels, then normalized the min to max intensity range on a length scale of 5 pixels. The resulting image was then masked to eliminate the PIV algorithm from being applied to regions of the image outside of the flow domain, e.g. the image of the wall.

A multi-pass cross-correlation algorithm was applied with decreasing interrogation window sizes. The initial interrogation windows were 128 pixel by 128 pixel squares, spaced with 50% overlap. The algorithm updated the interrogation window and removed outliers between each pass. The final three passes were performed with a constant circular interrogation window. The repeated passes with the same interrogation window were used to generate an estimated uncertainty in the results.

The final interrogation window size for the camera viewing separation from the ramp were selected to be 24 pixels by 24 pixels with 50% overlap. The final interrogation window size for the camera viewing the upstream boundary layer was selected to be 16 pixels by 16 pixels with 25% overlap. The slightly larger interrogation window in the ramp view allowed for more particles within the interrogation window, as imaged particle density was reduced in the region near the thinning edge of the light sheet. The slightly smaller interrogation window used on the upstream view was intended to capture steeper velocity gradients.

The result from the PIV algorithm for both camera views was an ensemble of 1000 two component velocity vector fields on a 171 window by 214 window grid. The windows were spaced 12 pixels apart. A vector postprocessing algorithm was then applied to the results. The algorithm applied two passes of a universal outlier detection based on a 5 vector by 5 vector patch. The algorithm removed groups of up to three vectors that were identified as outliers and replaced their

values based on interpolation. This algorithm was relied on to correct for errors resulting from bubbles that floated through the camera view.

Mean velocity fields and turbulence statistics were then calculated from the ensemble of 1000 postprocessed vector fields. The output was nine 171 x 214 matrices representing the mean velocities ($\bar{U}$ and $\bar{V}$), the standard deviations in velocities (σ_U and σ_V), the turbulence kinetic energy (TKE), the Reynolds stresses (R_{xx}, R_{yy}, and R_{xy}), and the maximum two-dimensional turbulent shear stress (TSS). These are all floating point values, oriented in the camera coordinate frame, with units of length of pixels and units of time equal to the laser interframe time Δt. The Reynolds stresses are defined in terms of the fluctuating portion of the Reynolds decomposed velocities (see equation 2.4) as follows:

$$R_{xx} = \overline{u'u'} \tag{4.4}$$

$$R_{yy} = \overline{v'v'} \tag{4.5}$$

$$R_{xy} = \overline{u'v'} \tag{4.6}$$

Postprocessing of PIV Results

The PIV results from DaVis were imported into Matlab for postprocessing. The first step was to map the results to the physical coordinate system. The physical coordinate system was defined as having the x-axis in the streamwise direction along the surface of the flat aluminum plate. The y-axis was oriented normal to the surface. A local origin was selected as the location where the light sheet intersected the seam between the flat aluminum plate and the backwards facing ramp. This was selected as it was visible in both camera views.

Rotating the Upstream Camera Data

The primary need for coordinate rotation was due the fact that the upstream camera was oriented with the 2560 pixel dimension in the wall-normal direction, which resulted in a swapped x and y coordinate compared to the physical frame. In addition, the sign of the camera y coordinate was positive down, counting from the top row of pixels. The camera mounting was not perfectly parallel with the wall. The required angle of rotation between the camera coordinate system and the physical coordinate system was determined by fitting a line through the saturated pixels at the wall. This was done for one image pair from each run and the median angle was found for each case. The origin was manually identified in the images. The typical rotation angle was approximately 4° more than the expected 90° rotation. The formulas for the rotated vector values are given in equations 4.7 through 4.13. The subscript 0 denotes the data in the camera reference frame and orientation. The subscript R denotes that the vector directions have been rotated to align with the physical coordinate system, but the points are still located on a grid based on the camera pixel layout. The final step was to create a new grid of points in the physical coordinate system, X_1 and Y_1, and map the data from the points (X_R,Y_R) to the points (X_1,Y_1). This mapping used the Matlab function `griddata` to interpolate the velocities and Reynolds stresses to the grid aligned with the wall. A linear interpolation was applied to the Reynolds stresses, while a cubic interpolation was

applied to the velocities in order to preserve gradients. The velocities were then multiplied by the scale of the image (in meters per pixel) and divided by the interframe time for that particular run, to reach dimensional units of m/s. The Reynolds stresses were multiplied by the square of that same factor to reach dimensional units of m^2/s^2.

$$X_R = cos(\alpha)X_0 - sin(\alpha)Y_0 \tag{4.7}$$

$$Y_R = -sin(\alpha)X_0 - cos(\alpha)Y_0 \tag{4.8}$$

$$\bar{U}_R = cos(\alpha)\bar{U}_0 - sin(\alpha)\bar{V}_0 \tag{4.9}$$

$$\bar{V}_R = -sin(\alpha)\bar{U}_0 - cos(\alpha)\bar{V}_0 \tag{4.10}$$

$$R_{xx_R} = cos^2(\alpha)R_{xx_0} + sin^2(\alpha)R_{yy_0} - 2sin(\alpha)cos(\alpha)R_{xy_0} \tag{4.11}$$

$$R_{yy_R} = sin^2(\alpha)R_{xx_0} + cos^2(\alpha)R_{yy_0} + 2sin(\alpha)cos(\alpha)R_{xy_0} \tag{4.12}$$

$$R_{xy_R} = -sin(\alpha)cos(\alpha)R_{xx_0} + sin(\alpha)cos(\alpha)R_{yy_0} + (sin^2(\alpha) - cos^2(\alpha))R_{xy_0} \tag{4.13}$$

Mapping the Separation Camera Data

The camera used to view separation had a simpler mapping to the physical space. As the location of separation would be analyzed in cylindrical coordinates, the data was mapped directly to a cylindrical coordinate based on the cylindrical shape of the backward facing ramp. A circle was fit to the bright line in the image where the light sheet intersected the cylindrical shape of the backward facing ramp. A cylindrical coordinate system was selected with the origin at the center of that fitted circle. A grid of points in the cylindrical coordinate frame was created, and a cubic interpolation was used to map the velocities in the camera reference frame to the cylindrical coordinate frame grid. The velocities in the cylindrical coordinate frame were then computed according to equations 4.14 and 4.15.

$$V_r = U_0 sin(\theta) + V_0 cos(\theta) \tag{4.14}$$

$$V_\theta = U_0 cos(\theta) - V_0 sin(\theta) \tag{4.15}$$

Determining Boundary Layer Parameters

The first variable to be determined from the upstream camera PIV data is the local freestream velocity. At every x location, the x-direction time-average velocity is analyzed to find the y-locations where the velocity is greater than 99.5% of the maximum velocity observed. This region of high velocity is identified as representing the freestream flow. The edges of this region are trimmed off to remove any spurious data due to interpolation at the edge of the data set. The median of the remaining region is identified as the local freestream velocity. It was observed that the freestream velocity, though noisy, appeared to be constant upstream of the point 971 mm from the leading edge of the flat plate. Therefore the mean of the local freestream velocities upstream of x=971 mm was selected as the representative freestream velocity for the given data point. This is the velocity parameter, $\bar{U}_e$, that will be used for normalizing velocity terms.

The velocity data from the upstream camera was found to be too noisy to evaluate velocity gradients. As a result, it was averaged over a narrow band in an attempt to remove noise. A 2 mm wide region was selected, centered about the point 965 mm downstream of the leading edge of the flat plate. This location was selected as it was far enough upstream of the backward facing ramp that the freestream velocity appeared to not be greatly influenced by the presence of the ramp. After further analysis, the freestream vertical velocity was found to be slightly negative, showing influence from the presence of the ramp, but it was low magnitude relative to the horizontal velocity.

At every distance from the wall (in the physical y direction), the mean value of each variable was found within the 2mm wide patch. This created a mean profile of velocities and Reynolds stresses. This data was normalized by the freestream velocity $\bar{U}_e$ and reported in the results.

The boundary layer thicknesses were computed from the mean velocity profile in the 2 mm wide patch. The 99% boundary layer thickness $\delta_{99\%}$ was determined as the location at which the mean velocity reached 99% of $\bar{U}_e$. The displacement thickness, δ^*, and momentum thickness, θ, were computed according to equations 2.8 and 2.9, respectively, using a trapezoidal integration scheme. The shape factor, H, was computed as the ratio of the two values. Both of these integrated parameters have potential for large errors resulting from the noisy velocity data in the first few interrogation windows adjacent to the wall. This region has the lowest magnitude velocities, the steepest velocity gradients, and the most excess scattered light, all of which can contribute to errors in the velocity calculation. Additionally, there is uncertainty in the exact location of the wall that contributes to the error in δ^* and θ through an uncertainty in the integration limit. The momentum thickness is less sensitive to errors at the wall, as the integrand approaches zero along with the velocity, unlike the integrand of the displacement thickness which approaches its maximum value at the wall.

Due to the noise in the velocity data at the wall, the slope of the near-wall velocity profile could not be used to estimate the shear stress. An alternative method, often referred to as Clauser's method or using Clauser plots, utilizes the slope of the velocity profile in the log layer (in log-linear coordinates) to estimate wall shear stress. It is unclear if this method is valid for the velocity profile over an SHS. An attempt was made to use an iterative algorithm to fit the data to the Law of the Wall according to equation 2.18, with the normalizing wall shear stress τ_w being updated based on the slope in the region $100 < y^+ < 200$. The accuracy of this method is unclear, as a waviness was observed in the velocity profile. Further investigation showed that a laser fringe pattern hidden in the raw images shows up as a coherent error in the mean velocity, which can locally change the slope being used for the skin friction estimation. It is believed that the laser fringe pattern, shown in figure 4.2, is a result of the interference between the incoming laser sheet and the reflected light bouncing off of the surface.

Identifying Boundary Layer Separation

The criteria for identifying the location of boundary layer separation was selected to be regions in which the tangential velocity along the ramp were negative, i.e. $\bar{V}_\theta < 0$. More complicated definitions for different categories of separation could be used, but would require a more compu-

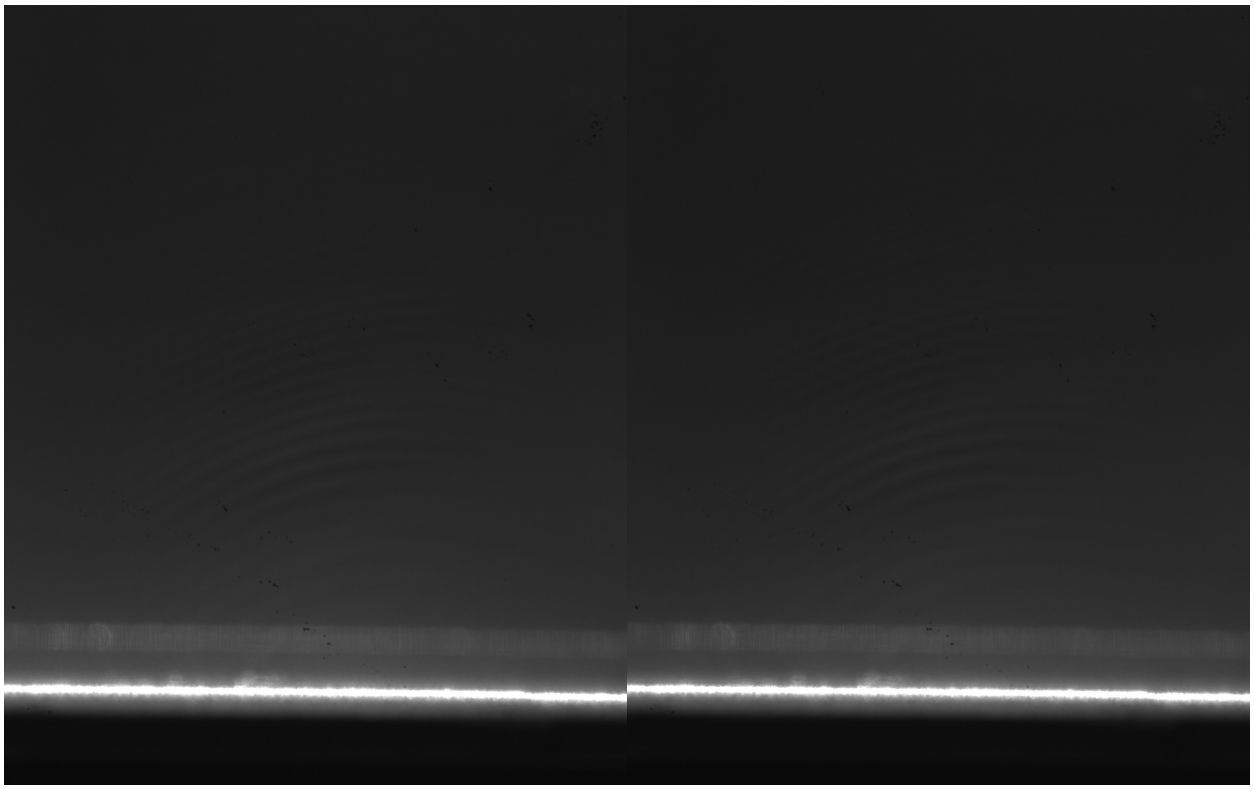

Figure 4.2: The average of a full ensemble of PIV images show a variation in brightness that appears to be a circular fringe pattern. This same pattern shows up as a coherent error in the velocity, causing the instantaneous slope of the velocity profile to be incorrect. The image on the left and on the right represent the average from each of the two laser pulses.

tationally intensive analysis of instantaneous velocity fields. This criteria proved to be acceptable for identifying the changes in separation we were interested in.

The tangential velocity data was analyzed in the region between the surface of the curved ramp and 13 mm off of the surface. At every radial distance from the surface, the angle of the first location of negative tangential velocity was identified. From this set of angles, two angles of separation were identified. First, the minimum angle at which $\bar{V}_\theta < 0$ was referred to as the "raw separation angle". As this criteria was not robust to noise or spatial outliers, a second criteria was also used. A second order polynomial was fit to the data set of radial position vs angle of negative tangential velocity. This fitted curve typically showed the trend that backflow occurred at earlier angles closer to the wall. The polynomial fit was evaluated at a radially position 1 mm above the wall, or nominally R=128 mm. This angle was identified as the fitted separation angle. The fitted separation angle is reported in the results when comparing surfaces. This process is visualized in figure 5.4.

Chapter 5

Results

The results are given for two preliminary surfaces and two final surfaces. The results include a comparison of roughness measurements, separation behavior, and turbulent boundary layer parameters.

5.1 Surfaces Tested

Four surfaces – labeled MB2, NW1, NW2, and MB3 – were successfully tested in the water tunnel with the final instrumentation. A preliminary matte black surface, labeled MB1, was used during the initial testing of instrumentation and in the selection of a field of view (FOV) for the PIV cameras. Results from surface MB1 are not reported here.

Table 5.1 summarizes the cases for the four surfaces tested. Surface MB2 consisted of matte black paint applied to a Mic 6 aluminum flat plate with a 3D printed ABS contoured backward facing ramp. This surface was used to establish preliminary baseline data for a hydrophilic surface. The second surface tested, labeled NW1, consisted of the same aluminum plate and ABS backward facing ramp coated with NeverWet® SHS spray. The data from these two surfaces were used to confirm that the geometry was sufficient in demonstrating a difference in separation phenomena, as well as identify the desired operating conditions. The measured roughness of the two preliminary surfaces is given in table 5.2. For reference, the nominal viscous length scale at the end of the flat plate (based on the bulk velocity and a 1/7 power law velocity profile over a smooth wall given in equation 2.11) varies between 41 μm at the 5 Hz pump frequency and 6 μm at the 35 Hz pump frequency. Based on the worst case roughness measurements, the matte black surface is clearly hydraulically smooth over the entire flow regime studied, while the NeverWet surface is estimated to be hydraulically smooth for all operating conditions at or below the 27 Hz pump frequency. This corresponds to a Reynolds number of approximately $Re_x \approx 3 * 10^6$. This estimate does not take into account any reduction is viscosity due to temperature changes, nor does it account for the unknown apparent roughness of large plastrons pinned to the surface.

After the geometry demonstrated the desired behavior, an aluminum backward facing ramp was CNC machined from 6061 aluminum with the same nominal dimensions as the 3D printed

Case	Geometry	Coating	Plastron Preparation	Pump Speed Range	Marker
MB2A	Printed ABS	Matte Black	Wetted	10 - 27 Hz	Black ·
MB2B	Printed ABS	Matte Black	Wetted	30 - 35 Hz	Black ·
NW1A	Printed ABS	NeverWet	New Install	10 - 35 Hz	Blue ·
NW1B	Printed ABS	NeverWet	Fully Wetted	10 - 35 Hz	Green ·
NW1C	Printed ABS	NeverWet	Dry Overnight	10 - 35 Hz	Cyan ·
NW1D	Printed ABS	NeverWet	Injected Air	20 - 40 Hz	Cyan x
NW2A	CNC 6061	NeverWet	New Install	10 - 25 Hz	Blue ∘
NW2B	CNC 6061	NeverWet	Wet Overnight	10 - 20 Hz	Blue □
NW2C	CNC 6061	NeverWet	Fully Wetted*	7 - 20 Hz	Green ∘
NW2D	CNC 6061	NeverWet	Injected Air	7 - 25 Hz	Cyan ∘
NW2E	CNC 6061	NeverWet	Fully Wetted*	2 - 15 Hz	Green □
NW2F	CNC 6061	NeverWet	Injected Air	2 - 15 Hz	Cyan □
NW2G	CNC 6061	NeverWet	Injected Air	7 - 25 Hz	Cyan Δ
MB3A	CNC 6061	Matte Black	Wetted	10 - 15 Hz	Black Δ
MB3B	CNC 6061	Matte Black	Wetted	2 - 35 Hz	Black ∘
MB3C	CNC 6061	Matte Black	Wetted	15 - 25 Hz	Black □
MB3D	CNC 6061	Matte Black	Wetted	1 - 13 Hz	Black ◇

Table 5.1: The successful test cases for four surfaces - two coatings applied to both preliminary and final geometry. The matte black surfaces (MB2 & MB3) were immediately wetted upon installation in the water. The NeverWet® surfaces were covered in a very thick air layer upon initial installation. The "fully wetted" cases refer to the surface being left submerged greater than 100 hours, resulting in no visually observable plastrons on the surface. *Note that surfaces NW2C and NW2E appeared to not remain fully wetted.

ABS geometry. Surface NW2 consisted of NeverWet® applied to the CNC machined backward facing ramp and a Mic6 aluminum plate. After completion of testing surface NW2, the coating was removed from this final set of geometry and matte black paint was applied. This final surface, labeled MB3, was used to repeat the baseline data at the same operating conditions as was studied on NW2 with identical underlying geometry. The measured roughness of the two final surfaces is given in table 5.3. The measured static contact angle for these surfaces is given in table 5.4. Note that the roughness measurements are very comparable to the preliminary surfaces and the same conclusions about a hydraulically smooth surface apply.

The condition of the surface of the matte black coatings (MB2 & MB3) did not noticeably change during testing. They were considered to be fully wetted at all times during all of the cases. The condition on the surface of the superhydrophobic coatings (NW1 & NW2) did vary between runs. A newly installed SHS coating was observed to have a very thick layer of air attached to the surface. This layer of air - either plastrons or large flat bubbles (as can be seen in Case NW2A of figure 5.1 or in figure 5.2)- would interact with the boundary layer, creating a dynamic surface. This

			MB2			NW1		
Station [in]	Direction	Position	R_a [μm]	R_q [μm]	R_z [μm]	R_a [μm]	R_q [μm]	R_z [μm]
1	Stream	Tap	1.777	2.092	8.269	5.324	6.999	29.336
1	Stream	Mid	1.602	1.966	8.496	6.603	8.031	33.367
1	Stream	Cam	1.078	1.317	5.580	4.306	5.507	21.999
1	Cross	Tap	1.734	2.151	9.325	4.937	6.210	24.075
1	Cross	Mid	1.199	1.498	6.870	4.174	5.076	18.854
1	Cross	Cam	1.816	2.164	8.761	4.970	6.587	28.592
20	Stream	Tap	1.508	1.784	7.332	7.762	9.540	39.040
20	Stream	Mid	1.171	1.480	7.590	5.618	6.999	28.499
20	Stream	Cam	1.119	1.403	6.532	4.533	5.831	24.590
20	Cross	Tap	1.664	2.094	9.284	4.604	5.970	25.463
20	Cross	Mid	1.579	1.946	8.526	6.735	8.662	35.227
20	Cross	Cam	1.195	1.486	6.537	4.141	5.751	29.096
38	Stream	Tap	1.097	1.385	6.597	5.112	6.649	26.309
38	Stream	Mid	1.313	1.574	6.606	4.058	5.099	21.747
38	Stream	Cam	1.683	2.046	8.426	4.646	5.736	22.083
38	Cross	Tap	1.282	1.597	7.075	5.161	7.239	31.326
38	Cross	Mid	1.571	1.969	8.692	6.583	9.086	40.017
38	Cross	Cam	1.063	1.315	5.866	4.269	5.828	26.232

Table 5.2: Measured roughness of preliminary surfaces MB2 and NW1. Note that roughness was measured at three streamwise stations: 1", 20", and 38" from the leading edge of the aluminum plate. The spanwise positions at each of those stations were defined as closer to the cameras ("Cam") or further from the cameras, but closer to a set of pressure taps ("Tap"). The roughness was recorded in the streamwise and crossstream directions.

was the state of cases NW1A and NW2A. During testing, the air would slowly get pulled off of the surface, leaving a thinner layer of plastrons. When surfaces NW1 or NW2 had been left submerged for several days, the plastrons on the surface appeared to dissolve into the water in the flow loop. In this case, no plastrons were visibly observed on the surface, and there was no variation or shimmer in the appearance of the surface when water flowed past it. These cases (NW1B, NW2C, and NW2E) were considered to be fully wetted surfaces. In order to reestablish the plastrons after a surface had become fully wetted two methods were attempted. First, water was pumped out of the water tunnel, such that the coated surface would be dry above the waterline. The surface as left to dry overnight before water was reintroduced into the tunnel. An example of this is case NW1C. However, the layer of plastrons on the surface after reintroducing water were not comparable in thickness or uniformity of distribution to a newly installed surface or after a new installed surface has been exposed to flow. It was found that injecting air into the flow upstream of the surface established the most repeatable uniform distribution of a thin layer of plastrons on the surface of the superhydrophobic coating. The

			MB3			NW2		
Station $[in]$	Direction	Position	R_a $[\mu m]$	R_q $[\mu m]$	R_z $[\mu m]$	R_a $[\mu m]$	R_q $[\mu m]$	R_z $[\mu m]$
1	Stream	Tap	1.072	1.348	6.533	4.528	5.480	22.341
1	Stream	Mid	1.012	1.222	5.676	3.923	5.042	20.351
1	Stream	Cam	0.912	1.159	5.413	6.667	8.966	39.879
1	Cross	Tap	0.972	1.177	5.892	4.794	6.323	27.937
1	Cross	Mid	0.993	1.229	6.254	3.576	4.626	20.258
1	Cross	Cam	1.094	1.374	6.876	5.408	7.307	30.968
20	Stream	Tap	0.815	1.027	4.701	5.099	6.435	29.600
20	Stream	Mid	1.123	1.334	5.854	4.556	5.703	23.577
20	Stream	Cam	0.733	0.950	4.746	3.438	4.337	17.824
20	Cross	Tap	0.991	1.268	6.335	5.315	7.511	33.519
20	Cross	Mid	0.996	1.252	6.630	4.512	5.665	23.748
20	Cross	Cam	1.011	1.275	6.644	5.316	6.506	26.807
38	Stream	Tap	0.961	1.208	5.931	3.684	4.852	21.649
38	Stream	Mid	0.927	1.194	6.360	3.537	4.825	23.186
38	Stream	Cam	0.983	1.181	5.172	5.658	7.057	30.288
38	Cross	Tap	1.027	1.265	6.010	4.188	5.680	25.226
38	Cross	Mid	0.941	1.184	6.171	4.592	5.945	25.112
38	Cross	Cam	1.083	1.358	6.945	5.697	7.281	29.035
40	Stream	Tap	1.166	1.450	6.570	4.533	5.802	24.967
40	Stream	Mid	1.019	1.230	6.003	4.670	5.994	26.388
40	Stream	Cam	0.935	1.140	5.146	3.892	5.145	22.723
40	Cross	Tap	0.886	1.120	5.602	4.541	5.826	24.576
40	Cross	Mid	1.090	1.328	5.921	5.878	7.279	29.441
40	Cross	Cam	1.187	1.468	7.095	6.230	7.945	35.658

Table 5.3: Measured roughness of final surfaces MB3 and NW2. Note that roughness was measured at three streamwise stations: 1", 20", and 38" from the leading edge of the aluminum plate. The spanwise positions at each of those stations were defined as closer to the cameras ("Cam") or further from the cameras, but closer to a set of pressure taps ("Tap"). The roughness was recorded in the streamwise and crossstream directions.

	MB3			NW2				
	Drop 1	Drop 2	Drop 3	Drop 1	Drop 2	Drop 3	Drop 4	Drop 5
Contact Angle (L)	70.8°	72.7°	77.0°	165.3°	156.4°	173.5°	172.3°	153.3°
Contact Angle (R)	72.8°	76.1°	73.2°	151.9°	160.9°	152.0°	162.8°	157.9°

Table 5.4: The static contact angle measured for both the hydrophilic surface (MB3) and the hydrophobic surface (NW2). Note that all of the contact angles observed on surface NW2 are greater than 150°, one criteria for being defined as superhydrophobic. The angle notation of "L" and "R" refers to angles observed on either side of the droplets.

air was injected through an approximately 1/8" port near the entry to the test section. The air was hand-pumped, injecting a slug of approximately 0.5 liters of air to be convected past the surface. The air injection was repeated at a rate up to approximately 150 times per minute, with a typical rate of approximately 1 Hz. This process was repeated intermittently based on visual feedback of the state of the surface for up to one hour, in order to establish a uniform distribution of plastrons. The flow condition with the pumps operating at 15 Hz to 20 Hz (bulk velocity of approximately 1.7 to 2.3 m/s) was found to be optimal for spreading the slugs of air across the entire surface. The cases following air injection (NW1D, NW2D, NW2F, and NW2G) were observed to have the most consistent and repeatable layer of plastrons.

Figure 5.1 shows the plastrons on the surface of coating NW2 at a location approximately 30 cm from the leading edge of the flat aluminum plate. The images were recorded with the pumps operating at 15 Hz, corresponding to a nominal fluid velocity of 1.7 m/s.

The cases after newly submerging the surface (NW2A and NW2B) show a thick layer of plastrons. However these plastrons were observed to dynamically move due to the turbulence in the flow, as well as get stripped off of the surface. On a larger length scale, the thick plastron large would form what appear to be standing wavefronts, with thicker air piling up immediately upstream of a region with most of the plastrons stripped away. Figure 5.2 shows the plastrons on surface NW2 immediately following submergence. Figure 5.3, captured during testing case NW2B, shows the patches where plastrons have been stripped away with thicker air layers collecting upstream. These inconsistent patches that form and grown make it difficult to quantify the behavior of the changing surface state. It is expected that the thicker air layer upstream of the patch would disturb the boundary layer. This is one reason that these cases (NW2A and NW2B) were not focused on when drawing conclusions.

The cases that were intended to represent fully wetted surfaces (NW2C and NW2E) are observed to have streaks or tracks where bubbles have traveled along the surface in the images recorded at the 15 Hz operating condition. It was noted during the testing of case NW2E that the bubbles and streaks were not present on the surface at low flow rates and the streaks only appeared when the pump speed was increased to 13 Hz (bulk velocity of 1.44 m/s). It is believed that these bubbles are being scavenged from elsewhere in the flow loop and are becoming attached to the SHS near the leading edge of the aluminum plate. With increasing flow rate, the bubbles progress further along the surface. At the flow rate shown, the bubble paths have only progressed a short distance past the

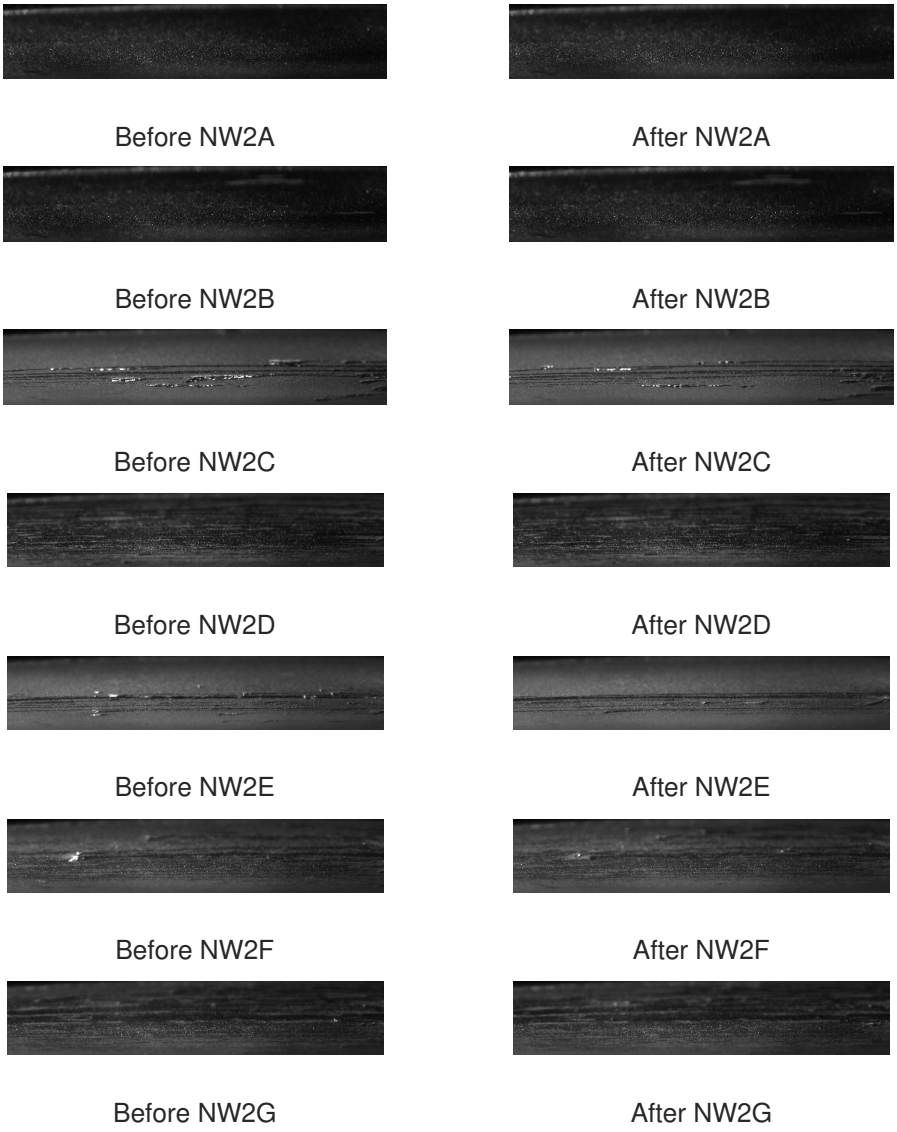

Figure 5.1: The state of the plastrons on surface NW2 can be observed for each case. The images were collected before and after a PIV run with the pumps operating at 15Hz for each case. Cases NW2A and NW2B show the thick plastron layer of a newly installed surface. Cases NW2C and NW2E are intended to be fully wetted. However they appear to be recruiting bubbles from the freestream that create streaks on the surface. Cases NW2D, NW2F, and NW2G show the surface after the surface has been replenished by injecting air. The FOV of these images is approximately 8 cm wide.

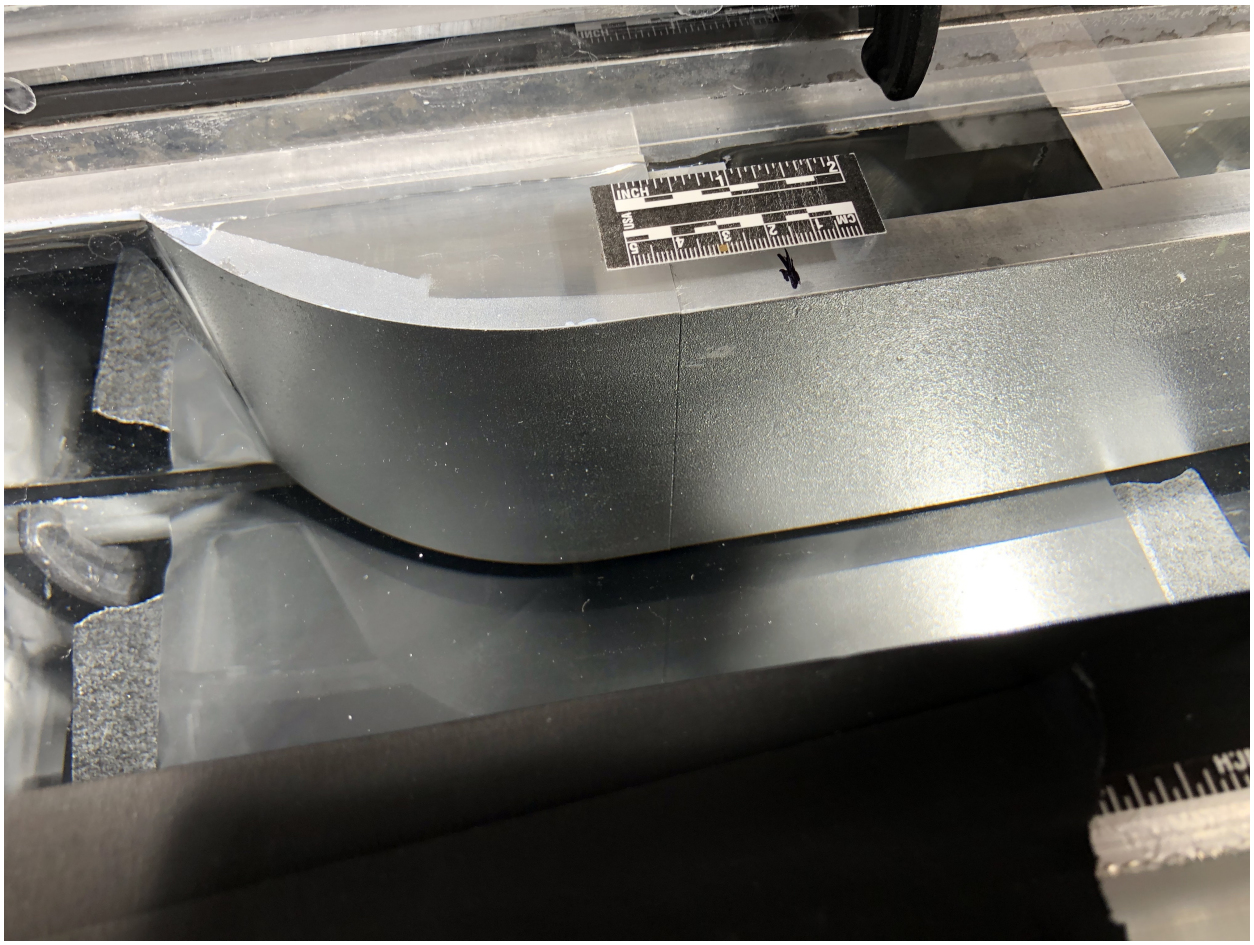

Figure 5.2: Surface NW2 is shown immediately after being submerged. Note the thick, dense distribution of plastrons on the surface.

camera FOV. Noting that images in figure 5.1 are recorded approximately 1/3 of the distance along the plate, it is surmised that the bubbles stop progressing down the plate when they reach a region of lower skin friction due to the thickening of the boundary layer in the streamwise direction. The random location of a few bubble streaks, along with the presence of large bubbles adhering to the surface at the end of the streaks, creates a highly variable influence on the boundary layer. This could explain the difference in observations between NW2C & NW2E compared to NW1B.

The final state of plastrons that was observed corresponds to the cases after injecting air (NW2D, NW2F, and NW2G). These cases show many streaks where bubbles have passed along the surface. On the short length scale shown, the surface appears to be more random than the cases following initial submergence of the surface. However, with the cases following air injection, the presence of bubble path streaks is distributed across the entire plate, as care was taken to inject air until bubbles were flowing across the entire surface. In addition, the pumps were operated at a high flow

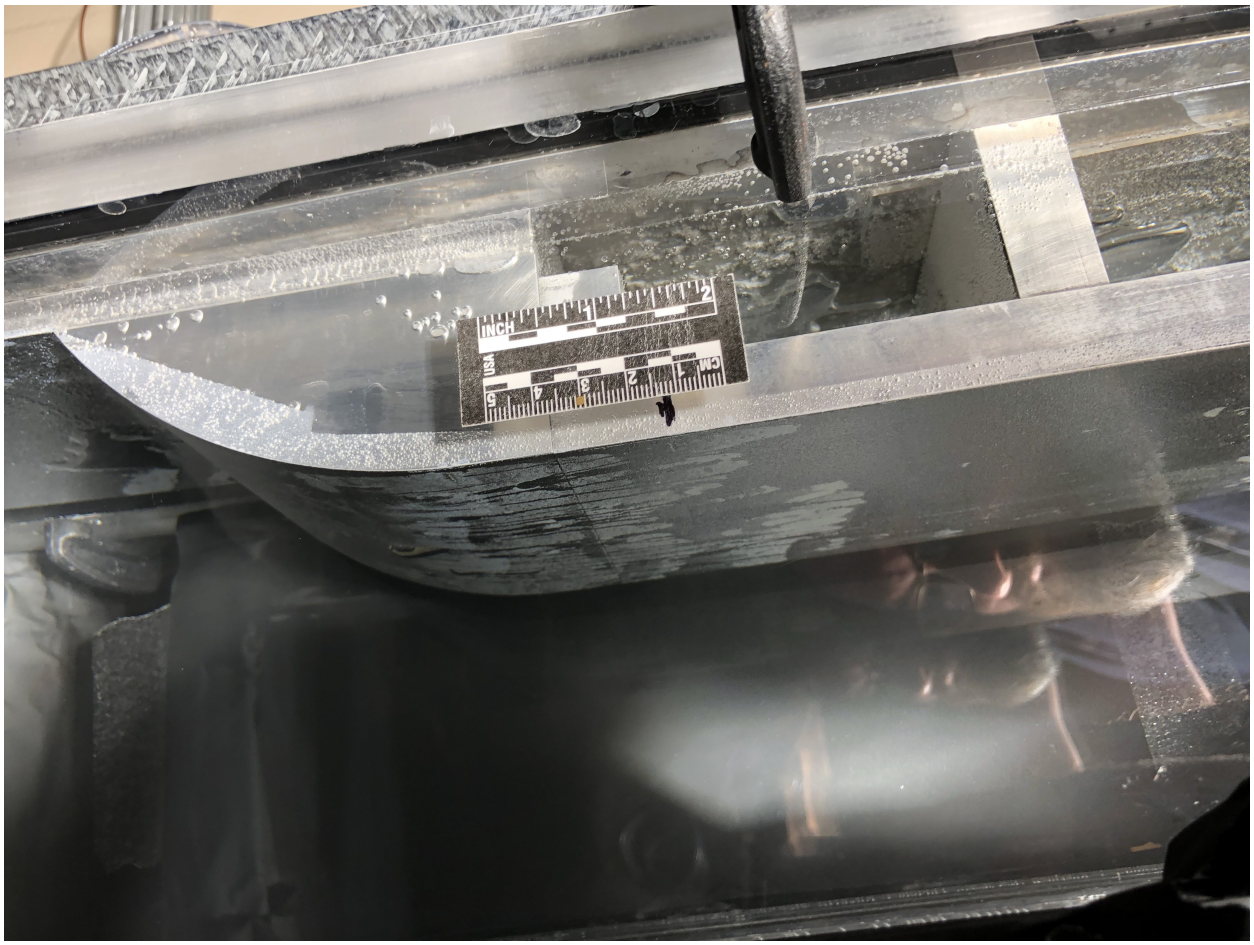

Figure 5.3: A freshly installed surface (NW2 shown) would shed plastrons, forming patches with significantly fewer plastrons. Often the region immediately upstream of the patch would appear to have a standing wave of excess air piled up.

rate following the air injection to generate high enough shear stress to remove any large bubbles left behind on the surface. As a result, the cases following air injection appear to have the most spatially uniform influence from the SHS, when observed on the length scale of the entire plate. These cases are the focus of the conclusions drawn from this study.

5.2 Separation Location

Under certain conditions, the superhydrophobic coating demonstrated a stark difference in the separation behavior, compared with the baseline. This can be seen in figure 5.4, which shows the regions of backflow on the ramp for the same operating condition for cases MB3A and NW2G. Recall that case NW2G is immediately following air injection to re-establish the plastrons. For the

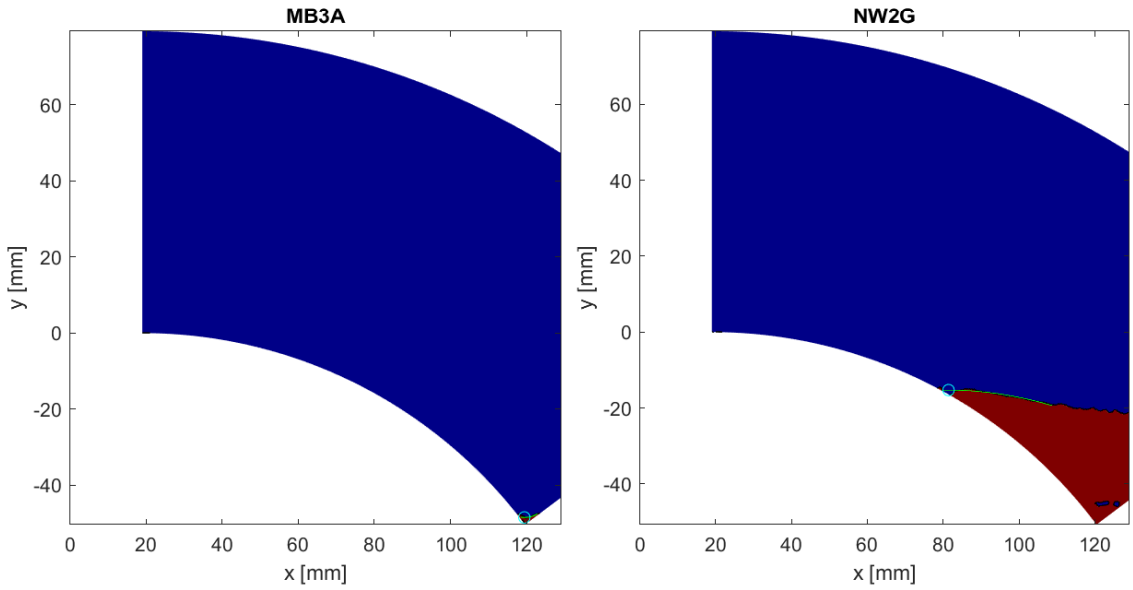

Figure 5.4: The location of boundary layer separation is vastly different between the baseline surface (left) and the SHS coated surface (right). The separation location is identified based on negative mean tangential velocity. Blue regions correspond with positive tangential velocity and red regions correspond with negative tangential velocity. The white circular arc in the lower portion of the plots corresponds with the contoured backward facing ramp. The green line shows a parabolic fit to the interface between positive and negative tangential velocity in a cylindrical coordinate frame. The cyan circle is located at the intersection between that fitted parabola and an arc located 1 mm above the surface of the ramp. The azimuthal coordinate of the cyan circle is referred to as the fitted separation angle.

operating condition shown, with both pumps driven at 15 Hz, the flow remains attached along the full length of the matte black ramp, with backflow only occurring at the vertex at the end of the ramp. In contrast, the flow separates from the SHS-coated ramp at a location approximately 55% of the distance along the arc of the ramp. This comparison is consistent with the trend seen throughout this study.

Separation from the Preliminary Surfaces

The critical result from this study was the determination of the point of separation from the backwards facing ramp. The identification of negative mean tangential flow along the curved surface was used as a surrogate for the separation location. The preliminary surfaces MB2 and NW1 were tested across a wide range of flow rates, pushing towards the upper end of the capabilities of the water tunnel. Analysis of the results shows that the location of separation from the baseline hydrophilic surface MB2 is highly dependent on the flow velocity. Figure 5.5 shows the angle of

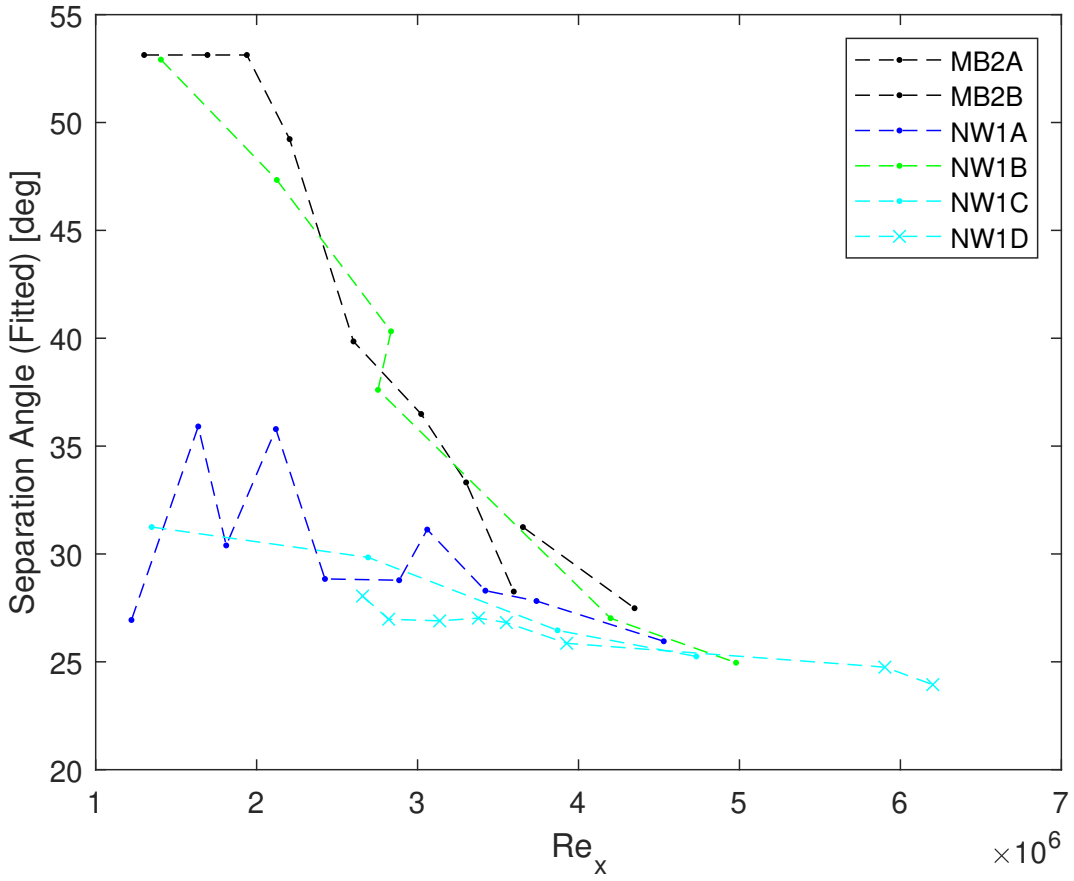

Figure 5.5: The results for separation angle from the preliminary surfaces MB2 and NW1 as a function of Reynolds number. Note that a separation angle of approximately 53° corresponds to no separation from the backwards facing ramp.

separation along the backward facing contoured ramp as a function of the Reynolds number. The Reynolds number is evaluated at a constant lengthscale of 0.965 m, equal to the location 45 mm upstream of the backward facing ramp at which the boundary layer parameters are evaluated. The viscosity varies with the measured temperature of the water. The primary variation in Reynolds number comes from the freestream velocity, which is determined from the upstream PIV results.

Figure 5.5 shows that at Reynolds numbers below approximately $2 * 10^6$ the turbulent boundary layer does not separate from the hydrophilic surface. As the velocity is increased, the boundary layer begins to separate, with the angle of separation advancing upstream until reaching a separation angle of approximately 30° around a Reynolds number of $3.5 * 10^6$. Above this flow rate, the separation angle appears as if it may plateau at an approximately constant value, or the slope of the trend be reduced. It is unclear if the baseline data in the range $3.5 * 10^6 < Re_x < 4.5 * 10^6$ is demonstrating

variability about a relatively constant value (similar to the data from the SHS) or continuing in a downward trend. Further data would be required to determine this.

The behavior of the hydrophobic surface NW1 varies significantly from case to case. Firstly, the fully wetted case NW1B appears to mimic the hydrophilic case closely, with the separation angle being only slightly advanced through the range of $1.5 * 10^6 < Re_x < 3.5 * 10^6$. This behavior suggests that case NW1B is confirmed to be a fully wetted surface and the separation behavior is not influenced by plastrons on the surface, and any additional roughness introduced by the NeverWet coating may be within the hydraulically smooth regime.

The behavior of the newly installed surface, NW1A is highly variable. The separation angle varies between approximately 27° and 37° in the range of $1.5 * 10^6 < Re_x < 3.5 * 10^6$ and trends toward a constant value of 25° at higher flow rates. This variation is consistent with the thick layer of plastrons and bubbles interacting with the boundary layer in a highly variable way. The clear reduction in angle of separation at the lower Reynolds numbers compared to the hydrophilic surface demonstrated that, at least in some cases, the presence of a superhydrophobic surface advances the onset of separation.

Cases NW1C and NW1D have thin, uniform distributions of plastrons based on visual inspection. These cases have less variation in separation location, though most of the data points collected were above $Re_x = 2.5 * 10^6$. The angle of separation for these two cases was consistently between 25° and 30° with only a slightly downward trend as a function of Reynolds number.

One conclusion from the data collected on the preliminary surfaces was that the separation location was dependent on both the Reynolds number and the type and condition of the surface, and the influence of Reynolds number was not necessarily consistent across different surfaces. Also, most of the variation in separation location occurred below $Re_x = 3.5 * 10^6$. Therefore the study of the final geometry should focus on the flow rates below this point and extend the range to lower Reynolds numbers. Also, the pump speed of 15 Hz corresponding to a Reynolds number slightly below $Re_x = 2 * 10^6$ was selected as a operating condition to be repeated as it showed a large difference between the hydrophilic and hydrophobic cases.

Separation from the Final Surfaces

The final surfaces, applied to the CNC machined aluminum geometry, were used to focus on the flow regime in which the hydrophilic and hydrophobic surfaces demonstrated different separation behavior, while expanding the range of some of the baseline data. Figure 5.6 data points collected for separation from the aluminum ramp geometry. The first thing to note is that the data points below $Re_x = 5 * 10^5$ correspond to a flow regime at Reynolds numbers below that of a fully turbulent boundary layer. As a result, the flow separates much earlier than any of the other cases, around 15°. Additionally, the type or condition of the surface does not appear to significantly influence the separation behavior in this laminar or transitional regime. The second thing to note is that the hydrophilic case appears to converge to a constant separation angle around 25° at high Reynolds numbers. This confirms one of the speculations from the preliminary data.

The additional data collected in the range of $5 * 10^5 < Re_x < 3 * 10^6$ shows that the turbulent boundary layer separation from the hydrophilic and hydrophobic surfaces demonstrates a similar

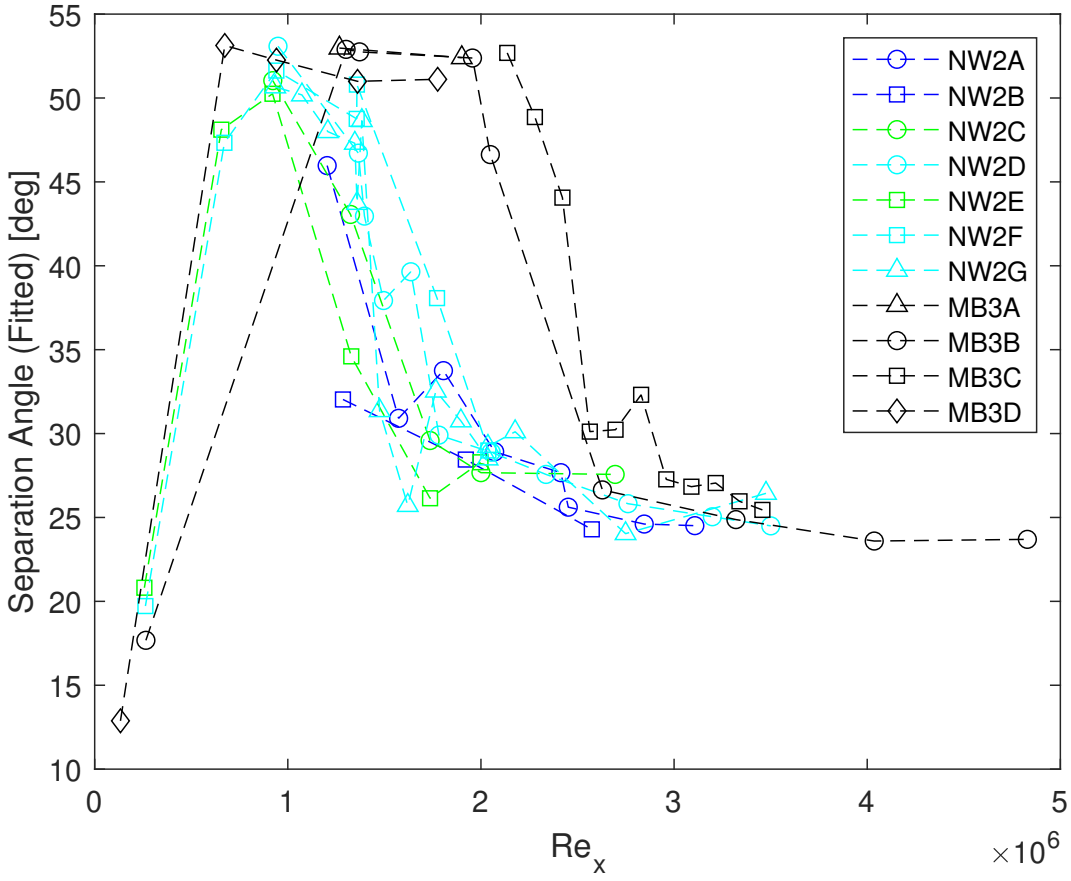

Figure 5.6: The results for separation angle from the final surfaces MB3 and NW2 as a function of Reynolds number. Note that a separation angle of approximately 53° corresponds to no separation from the backwards facing ramp. The separation angle appears to converge to approximately 25° at $Re_x > 3 * 10^6$ for all of the surfaces.

dependence on Reynolds number, with a relatively constant separation angle below some critical Reynolds number, then a steep transition to another relatively constant but significantly earlier separation angle. The transition between these two behaviors happens at approximately $Re_x = 1.3 * 10^6$ for the hydrophobic cases, and around $Re_x = 2 * 10^6$ for the hydrophilic cases. For all cases, the separation angle at lower Reynolds numbers seems to indicate that the boundary layer remains attached for most of the distance down the ramp. The separation angle converges to around 25° to 30° at high Reynolds numbers. In other words, the application of this hydrophobic surface reduces the Reynolds number at which the turbulent boundary layer detaches from the backward facing ramp. It should be noted that this dependency may be on the freestream velocity and not the Reynolds number. Further work specifically varying the fetch length of the flat plate or the viscosity of the water is required to determine the nature of this dependency.

Another thing to note is that the fully wetted surfaces of cases NW2C and NW2E demonstrate a different behavior than that of the fully wetted preliminary surface of case NW1B. While case NW1B demonstrated behavior very similar to the hydrophilic surface, cases NW2C and NW2E demonstrate the opposite variation from a newly installed SHS: they both have separation angles either comparable to or earlier than the SHSs that are covered in plastrons. It is not immediately apparent why this behavior is different than case NW1B. This may be a result of the bubbles observed on these surfaces, as discussed in figure 5.1.

There is a specific range of flow rates at which the turbulent boundary layer separation behavior is consistently different between the hydrophilic and hydrophobic surfaces. In the range $1.5 * 10^6 < Re_x < 2.5 * 10^6$, the turbulent boundary layer remains attached to the hydrophilic surface most of the way down the ramp, yet separates much earlier from the hydrophobic surface. This range, shown in figure 5.7, was studied in greater detail in an attempt to identify the cause of the difference in behavior.

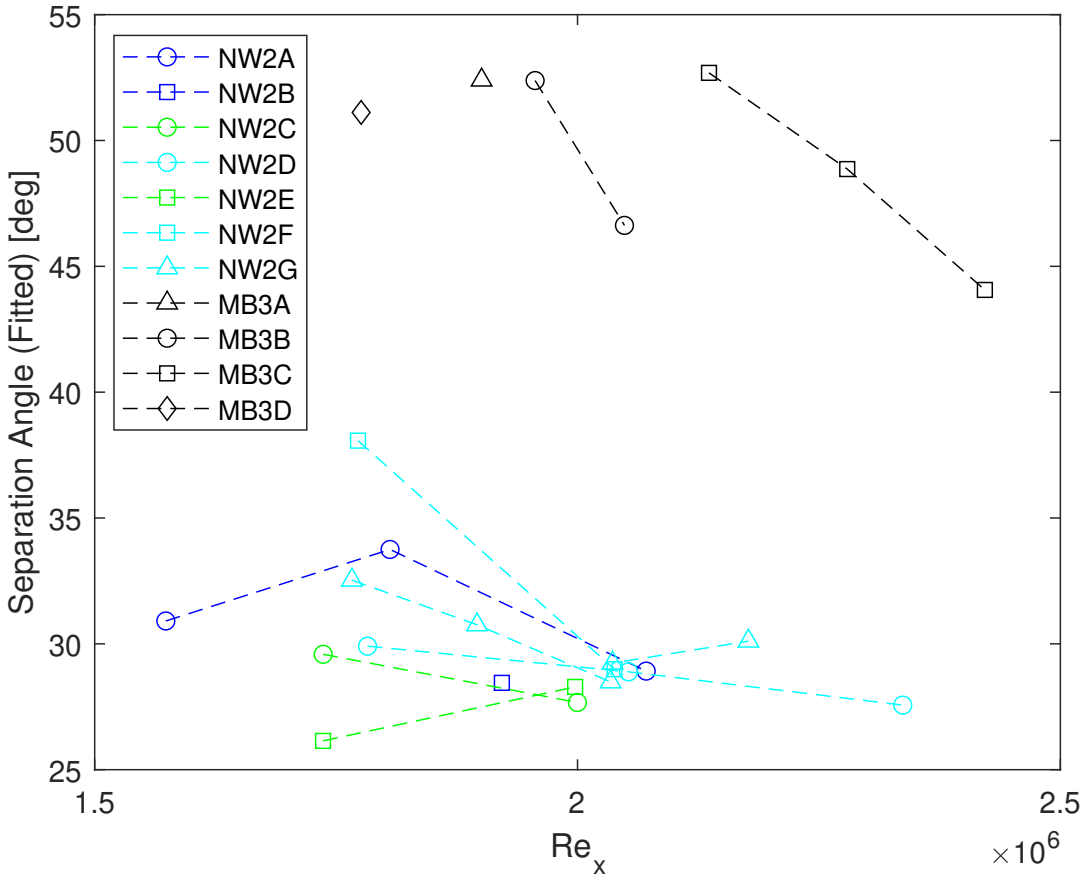

Figure 5.7: The results for separation angle from the final surfaces MB3 and NW2 in the range of Reynolds number over which the separation angle is consistently different. In this flow regime of $1.5 * 10^6 < Re_x < 2.5 * 10^6$, the separation angle from the hydrophilic surface is between approximately 45 ° and 53°, while the separation angle from the hydrophobic surface (across all states of plastrons) is between approximately 26° and 38°.

5.3 Boundary Layer Parameters

As the separation data and surface observations show, there are multiple separate phenomena driving the behavior observed. The plastron state changes between different cases, as well as can change within a single case as a function of time and flow velocity. The separation behavior is highly dependent on the Reynolds number. Based on this observation, a specific range of $1.5 * 10^6 < Re_x < 2.5 * 10^6$ was identified to investigate the differences between the hydrophilic and hydrophobic cases. The momentum thickness was selected as a preliminary measure to identify which cases should be included in that investigation.

Integral Parameters

The boundary layer parameters relevant to the description of behavior in the von Kármán momentum integral (VKMI) equation are obtained through integrating the velocity profile throughout the boundary layer. The momentum thickness, θ, and displacement thickness, δ^*, should increase with increased upstream skin friction, while decreasing as a function of Reynolds number as indicated by equation 2.12. The momentum thickness was selected as a screening parameter, as it is a measure of the effectiveness of the SHS at reducing skin friction. It has an advantage over the displacement thickness in that the integrand of momentum thickness trends to zero at the wall and therefore should be less sensitive to uncertainty in the location of the wall.

Figure 5.8 shows the momentum thickness in the boundary layer 45 mm upstream of the backward facing ramp, at x=965 mm from the leading edge of the flat plate. Once again the data below $Re_x = 5 * 10^5$ is in a laminar or transitional regime and should not be included as part of any trends in the turbulent data. Noted first, the data exhibits a lot of noise within each case, especially for the baseline case. However, the baseline data from surface MB3 does tend to exhibit a general trend of slightly decreasing momentum thickness as a function of Re_x, as would be expected. In comparison to the trend of the baseline case, the cases of a freshly installed SHS with thick plastrons (shown in blue as NW2A and NW2B) appear to have a slightly increased momentum thickness, which would correspond to additional drag upstream on the coated plate. These cases appear to slightly increase in momentum thickness as a function of Reynolds number. It is speculated that this may be indicative of the thick plastrons acting like roughness elements and increasing drag. The interaction between the plastrons and the flow that was visually observed may be changing the topography of the interface in a way that increases the drag. However it is difficult to draw clear conclusions with so much variation in the baseline behavior.

The cases of the SHS immediately following air injection (shown in cyan as NW2D, NW2F, and NW2G) show a clear trend. Appearing to have slightly lower momentum thickness than the baseline surface, these cases show a steep decrease in momentum thickness over the approximate range from $Re_x \approx 1 * 10^6$ to $Re_x \approx 2 * 10^6$. Above $Re_x \approx 2 * 10^6$, the momentum thickness begins to rise again. Recalling the visual observations of the fully wetted surface, this was the approximate flow rate required for a bubble to be dragged along the surface. It is speculated that the higher momentum thickness at higher flow rates results from entering a flow regime in which the thinner plastrons of these cases begin to interact with the boundary layer, possibly forming larger bubbles that act to increase drag. Recall that the roughness of the underlying surface would be expected to be hydraulically smooth up to a Reynolds number of approximately $Re_x \approx 3 * 10^6$.

The data from the cases intended to be fully wetted (shown in green as NW2C and NW2E) follow a trend in momentum thickness somewhat similar to the cases immediately following air injection. At flow rates below $Re_x \approx 2 * 10^6$ the momentum thickness is more variable than the air injection cases, and has a flat or slightly downward trend. Above $Re_x \approx 2 * 10^6$ the momentum thickness rises quickly, which reinforces the theory that the rise is due to larger plastrons or bubbles moving along the surface, as this was observed for these surfaces as previously discussed.

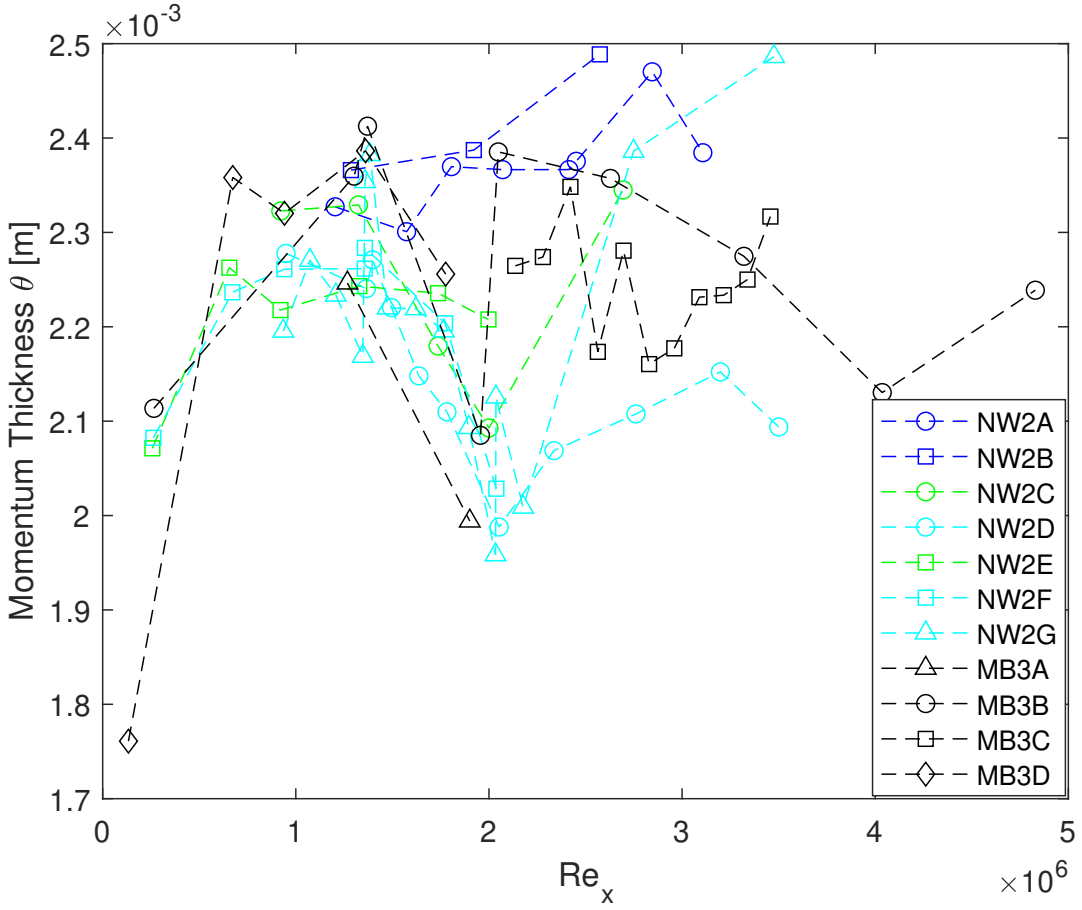

Figure 5.8: The momentum thickness on surfaces NW2 and MB3 as a function of Reynolds number, computed in the boundary layer 45 mm upstream of the backward facing ramp. Note that the thick plastron layer on newly installed surfaces (NW2A & NW2B) leads to a greater momentum thickness. The thinner layer of plastrons achieved after air injections on cases NW2D, NW2F, and NW2G leads to a lesser momentum thickness. Both of these are shifts in the mean away from the behavior of the hydrophilic surface. This data suggests that the thinner layer of plastrons may reduce skin friction, while the thicker layer of plastrons may increase the skin friction.

Based on this review of the momentum thickness data, the cases following air injection to replenish the plastrons were selected to be the focus of more in-depth analysis. These are cases NW2D, ND2F, and NW2G. They demonstrate a consistent trend of earlier separation in the flow regime of interest. Additionally they show a consistent trend of reduced momentum thickness, which suggests that they may be effectively reducing skin friction. These consistent behaviors are a result of the visually observed consistent state of thin plastrons across the entire coated plate.

The cases with a freshly installed SHS and a corresponding thick plastron layer demonstrated high variability within a short timescale as the plastrons came off of the surface in various patches.

Additionally they demonstrated increased momentum thickness, which could be indicative of drag increase. It is difficult to define the state of the surface during one of the data points due to the high spatial and temporal variability. Similarly it is difficult to define the state of the plastrons for cases where surface NW2 was intended to be fully wetted. The behavior was sometimes similar to the cases following air injection, but had a different visual appearance and was more prone to have a few larger bubbles visible on the surface. This behavior was very different from the fully wetted case on the preliminary surface, which behaved very similar to the baseline case. As a result of the high variability in the state of the surface for these cases, they are not the focus of further analysis in this work.

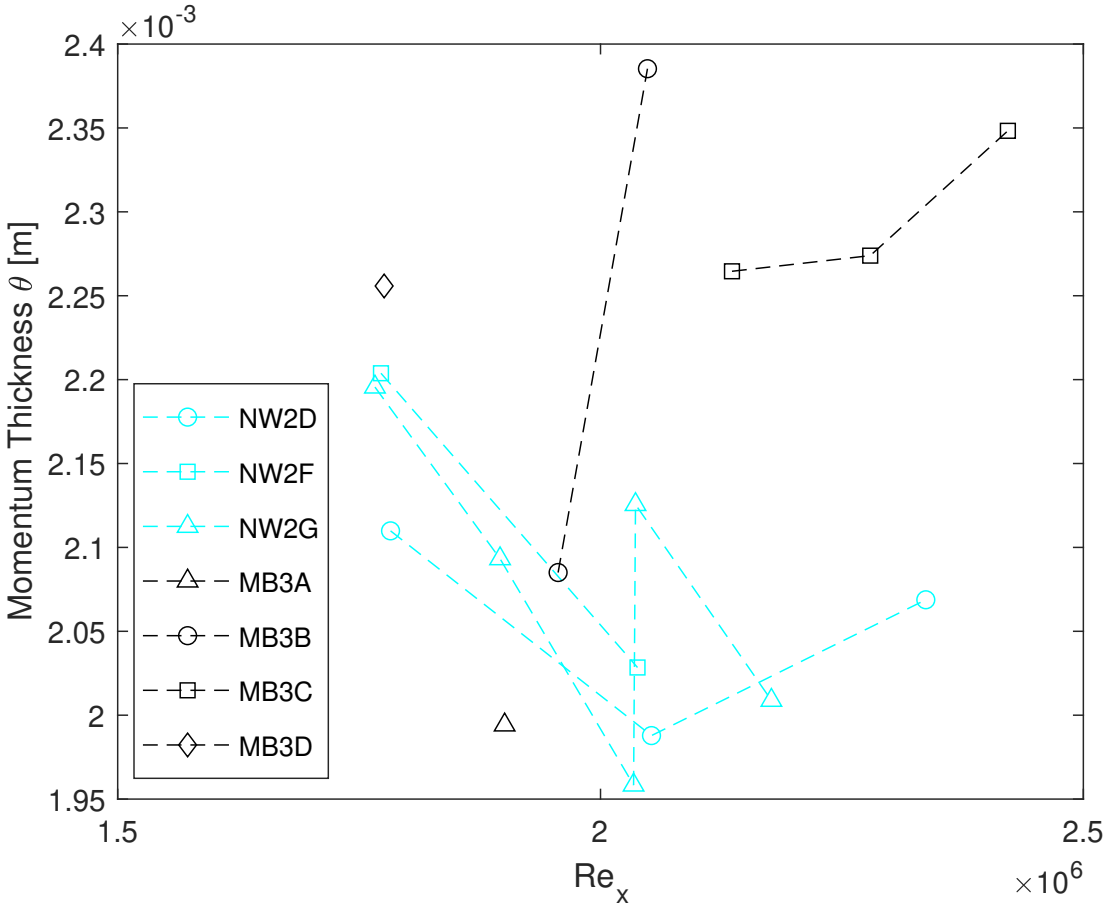

Figure 5.9: The momentum thickness as a function of Reynolds number for the velocity range of interest. The black markers correspond with the baseline surface, while the cyan markers show cases where a thin layer of plastrons have been freshly replenished on the SHS.

Figure 5.9 shows the momentum thickness in the Reynolds number range of interest for the two states of surface being compared: cases on the baseline surface MB2 and the cases on surface NW2

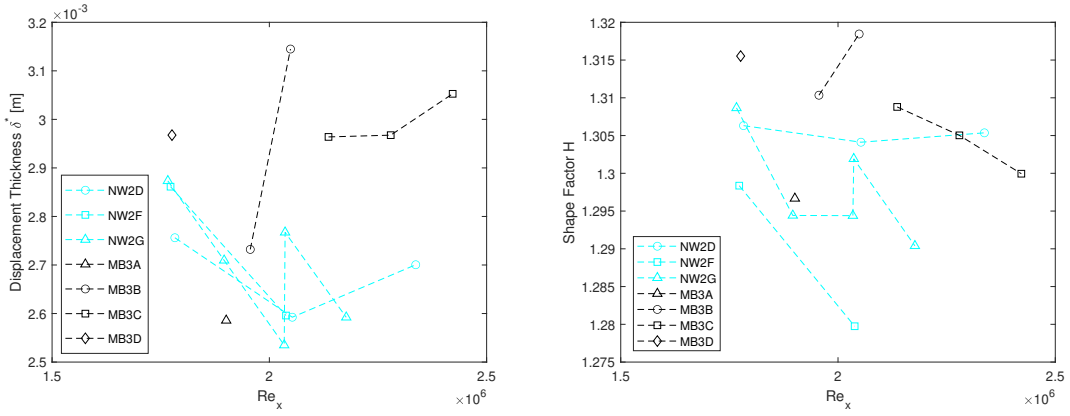

Figure 5.10: The displacement thickness and the shape factor, or ratio between displacement thickness and momentum thickness, as functions of Reynolds number for the velocity range of interest. Recall that separation typically occurs at a shape factor greater than 1.8.

with a recently replenished thin layer of plastrons. Note that the baseline data from surface MB3 displays large variation in momentum thickness. This is greater than would be expected based on the PIV measurement uncertainty alone. There may be some source of bias error that varies between runs.

Figure 5.10 shows the corresponding results for displacement thickness and shape factor. The displacement thickness results are similar to those of the momentum thickness, with the boundary layer over the SHS displaying slightly less thickness than that of the baseline case. The shape factor of the boundary layers over the two surfaces does not give any insight into the cause for the difference in separation location. Recalling that separation typically occurs at a shape factor greater than 1.8, the slightly higher average shape factor of the baseline case indicates that it would actually be closer to the point of separation (if the phenomenon could be explained by a simple evolution of the shape factor) even though the turbulent boundary layer over the baseline surface remains attached longer.

The analysis of the integral parameters of the boundary layer upstream of the ramp has two key takeaways. First, the thin layer of recently replenished plastrons are most likely effective at reducing the skin friction, as indicated by the slightly reduced momentum thickness. Second, the shape factor upstream of the ramp is not a useful indicator of robustness to separation in this case.

Velocity Profile

The velocity profiles were normalized according to the Law of the Wall, assuming a constant skin friction coefficient of 0.0034 to compute the wall units. This value was selected based on an estimate using equation 2.13, assuming a Reynolds number of $Re_x = 2 * 10^6$ is representative of this flow regime. The velocity profile in figure 5.11 is representative of the type of behavior observed. It shows that the superhydrophobic coating allows for increased velocity in the boundary layer. There

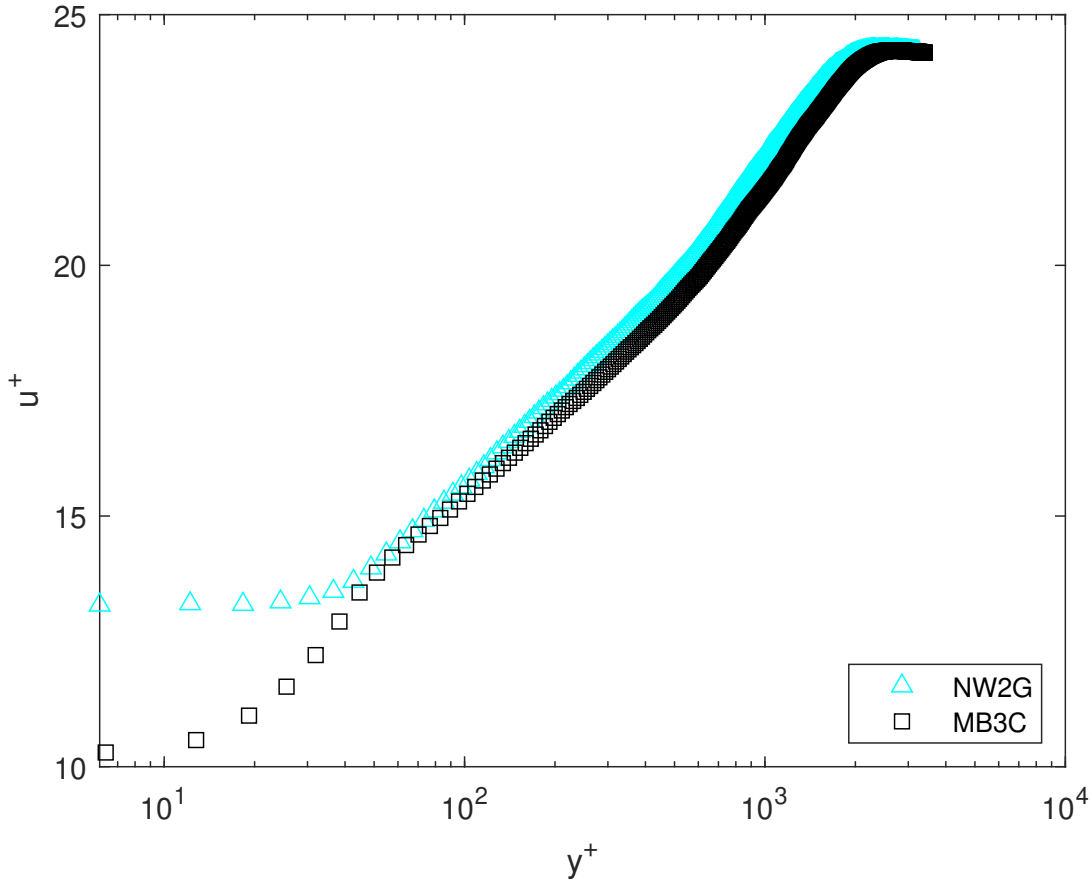

Figure 5.11: An example velocity profile 45 mm upstream of the ramp, plotted in wall units. This data was collected with the pumps operating at 16 Hz. This data is normalized based on an assume skin friction coefficient of 0.0034.

is significantly increased velocity in the near-wall region which corresponds to the expected slip at the wall. A slight increase in velocity is seen in the logarithmic region, which slowly increases moving into the wake region far from the wall. The slope of the profile in the logarithmic region is similar between the baseline and SHS cases, though slightly steeper for the SHS case. Additional velocity profile plots are shared in appendix B. One additional observation is that the baseline data does not appear to converge to zero velocity at the wall. This is most likely due to insufficient spacial resolution of PIV interrogation windows in the viscous sublayer.

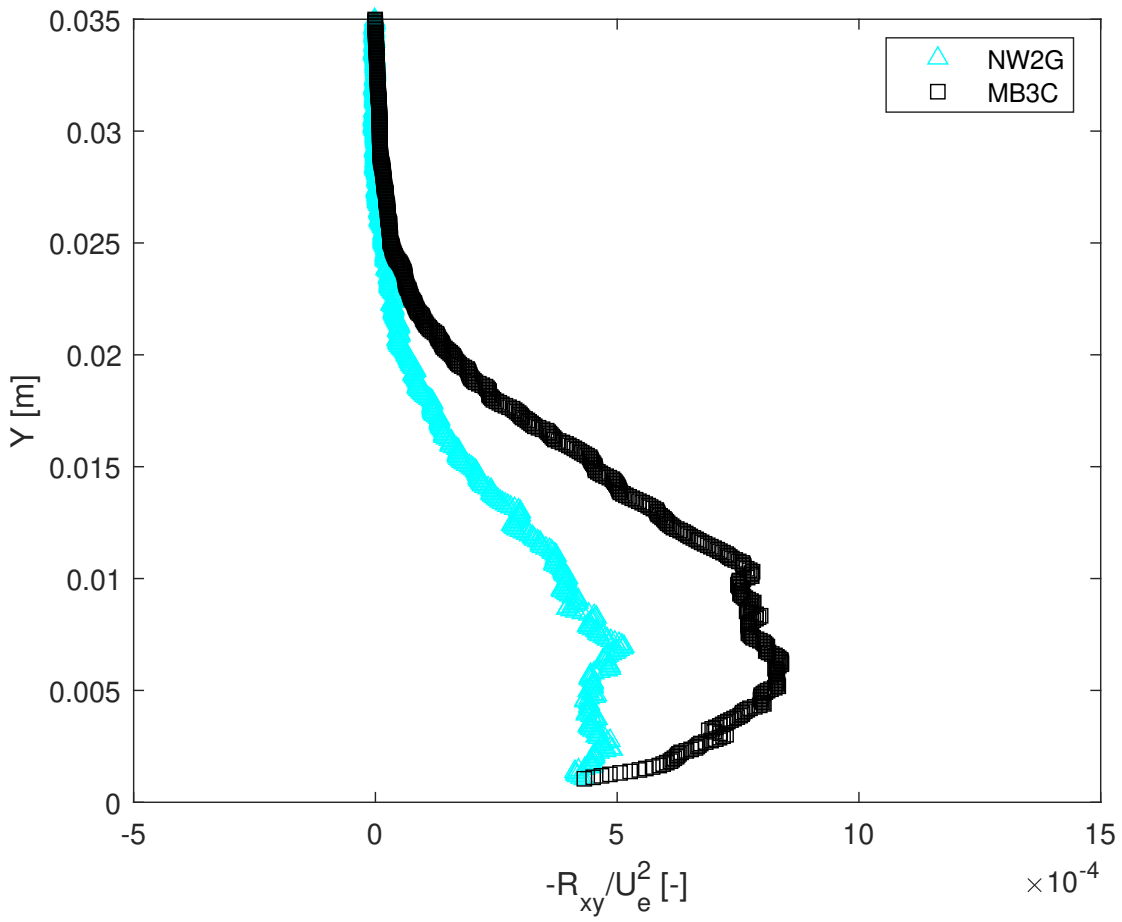

Figure 5.12: An example of the Reynolds shear stress, R_{xy}, in the boundary layer 45 mm upstream of the ramp. Note that the SHS reduces the peak magnitude by approximately 40%, while shifting the location of the peak slightly closer to the wall.

Reynolds Stresses

The key difference observed in the boundary layer between the hydrophilic and hydrophobic cases was a change in the Reynolds stresses. Summaries of the mean velocities and Reynolds stresses in the flow regime of interest are plotted in appendix B. Notably, the primary differences arise in R_{xy} and R_{yy}. These are shown in figures 5.12 and 5.13 respectively. The only notable observation in the mean behavior is that the mean velocity in the wall-normal direction is slightly negative in all of the cases. This is due to the proximity to the ramp and indicates that the boundary layer is thinning slightly at this location 45 mm upstream of the ramp.

The hydrophobic surface significantly reduces the turbulent mixing within the boundary layer. The Reynolds shear stress typically has zero magnitude outside the boundary layer, then slowly

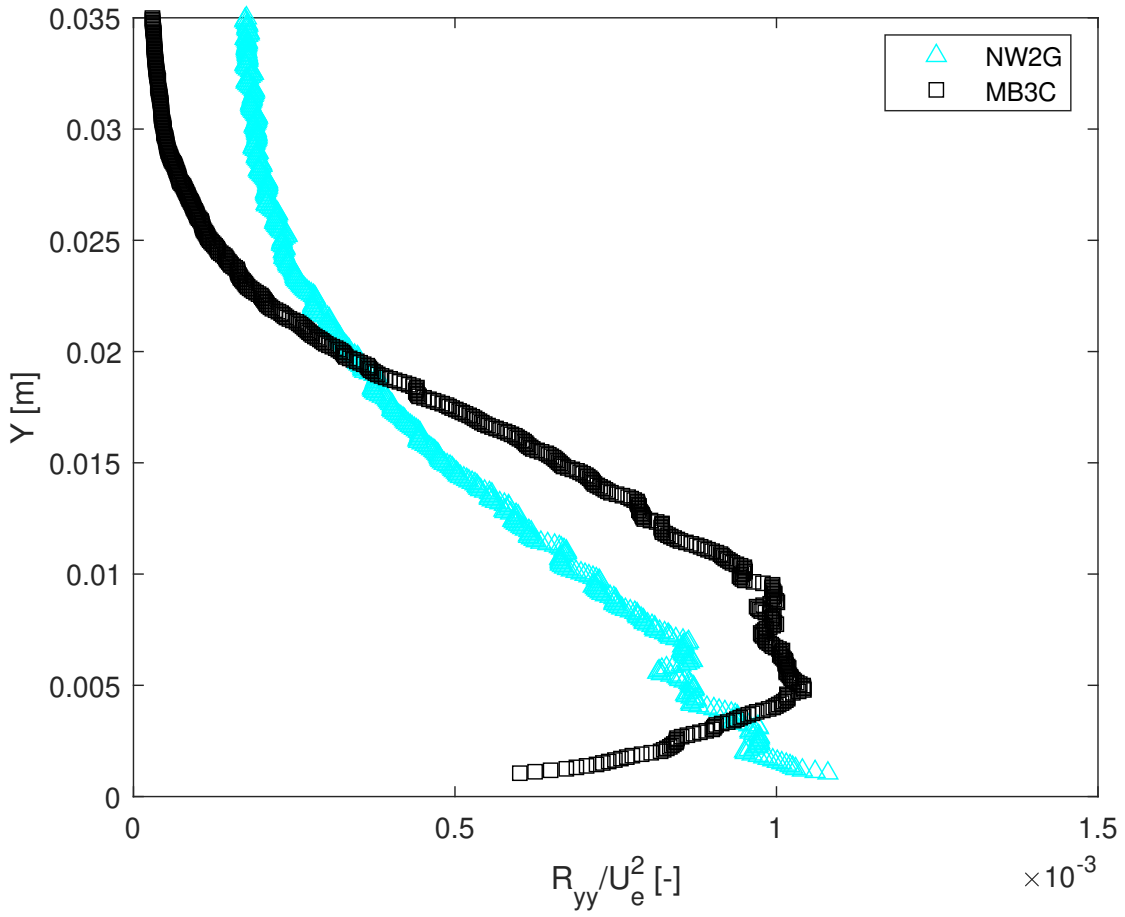

Figure 5.13: An example of the wall-normal Reynolds stress, R_{yy}, in the boundary layer 45 mm upstream of the ramp.

increases closer to the wall. It reaches a peak magnitude in the lower third of the boundary layer before decaying back to zero at the wall. In a turbulent boundary layer, the sign of R_{xy} is negative, as mentioned in the discussion of equation 2.28. Both baseline cases and the SHS cases were observed to follow this behavior. However the magnitude of the Reynolds shear stress is reduced in the boundary layer over the SHS. The peak magnitude of the Reynolds shear stress over the SHS was observed to be as low as approximately 50% of the comparable Reynolds stress over the baseline surface. Additionally, the location of the peak Reynolds stress appears to be shifted slightly closer to the wall for the SHS cases. The magnitude and location of the peak Reynolds shear stress were identified based on a curve fit to the data in the region of the peak. Those values are reported in the summary of results in table 5.5. The Reynolds shear stress, R_{xy}, represents an important mechanism of turbulence mixing higher velocity parcels of fluid closer to the wall. A reduced Reynolds shear stress results in less momentum near the wall. This is likely the primary mechanism by which the

hydrophobic surface advances the onset of separation.

The wall-normal Reynolds stress, R_{yy} did not change significantly in overall magnitude between the baseline and SHS cases. However the shape of the profile changed significantly. The shape of the baseline profile of R_{yy} is comparable to the described shape of the R_{xy} profile: zero magnitude in the freestream and at the wall with a maximum magnitude occurring in the lower portion of the boundary layer. The wall-normal Reynolds stress over the SHS does not follow this trend. Interestingly, the wall-normal Reynolds stress, R_{yy}, does not trend to zero at the wall for most of the observed SHS cases. It is possible that this is due to some compliance of the plastrons allowing wall-normal velocity oscillations at the wall. Another possible explanation of this observation could be that the PIV results near the wall have increased noise for the SHS cases that disguises a decay in R_{yy}. This is unlikely, as the data shown has been trimmed at y=0.001 m, removing data where the image of the wall itself might be within the interrogation window. Additionally, R_{yy} is observed to be a low magnitude non-zero value in the freestream for the SHS cases. One possible cause of this is that the earlier separation is slightly influencing the local freestream fluctuations in velocity at this upstream location.

The observation of reduced Reynolds shear stress is the most clear explanation for the cause of earlier separation. While the slightly higher fluctuations in the freestream velocity may indicate that there could be some feedback from the closer proximity of the separation location influencing the measurements at this location, it is unlikely that the increase in freestream turbulence would cause the observed decrease in the Reynolds shear stress. Therefore, the decreased Reynolds shear stress is attributed to the presence of the superhydrophobic coating. It is believed that this is the mechanism by which the SHS modifies the separation location and not a byproduct of the modified separation. Additional boundary layer data collected further upstream of the ramp could confirm this, however it would require a different instrumentation method, such a scanning laser Doppler velocimetry probe or a second light sheet separate from the one illuminating the ramp.

5.4 Results Summary

The results from the cases and flow regime of interest are summarized in table 5.5. The results are averaged across the SHS and baseline surfaces for data collected specifically at the 15 Hz operating point. This provides a very clear comparison between the two surfaces at the exact same freestream velocity. This freestream velocity is determined from the PIV results, so the fact that all data points are within 0.01 m/s suggests that the PIV and postprocessing algorithms are robust at capturing the mean flow. It also instills confidence that the comparative results between the two surfaces are comparing boundary layers that are exposed to the same freestream condition.

The variation in Reynolds number for data at the same flow velocity highlights that the water temperature was not controlled during these experiments. However there is no obvious trend with Reynolds number independent of the flow velocity.

As previously discussed, the momentum thickness is slightly reduced by the SHS, with a mean 7% lower than that of the baseline case. This suggests that the SHS acts to reduce skin friction. In contrast, the estimated skin friction coefficient is increased by 12% in the mean. This comes

from estimates based on the slope of the velocity profile in the logarithmic region. As previously discussed, there is some error in this estimate caused by the observed fringe pattern. Additionally, the mean for the SHS aligns well with the theoretical estimate for skin friction coefficient, while the baseline case is significantly less than the theoretical estimate at that Reynolds number. Though the magnitude of the skin friction is likely biased by the fringe pattern, an increase in local skin friction could actually be consistent with the presence of a drag reducing SHS. In addition to indicating the presence of more momentum near the wall, the reduced momentum thickness of the SHS indicates a thinner boundary layer. As the freestream velocity is very consistent at a fixed pump frequency, the thinner boundary layer will result in a steeper velocity gradient which directly translates to a higher skin friction estimate. With different instrumentation with higher resolution near the wall, the skin friction could be estimated from the velocity profile in the viscous sublayer.

The Reynolds shear stress demonstrates the largest change in the behavior as a result of the SHS. The average peak Reynolds shear stress is reduced by 41%, with the location of the peak shifting 15% closer to the wall. As the influence of the Reynolds shear stress on the evolution of x-momentum scales with its gradient, this observed shift will result in less momentum being turbulently mixed to the wall.

The SHS demonstrates a clear influence on the angle of separation. At the 15 Hz operating condition, the separation occurs within a tight window of angles between 28.5° and 29.2°. This is in stark contrast the mean baseline separation at 51°, as well as its minimum observed separation angle at the 15 Hz operating condition of 46.6°.

Case	Pump Frequency [Hz]	Re_x $* 10^{-6}$ [-]	U_e [m/s]	θ [mm]	C_f $* 10^3$ (Est.) [-]	$\left\|\frac{R_{xy}}{U_e^2}\right\|_{peak}$ $* 10^4$ [-]	$y_{R_{xy}}$ [mm]	Separation Angle (Fitted) [°]
NW2D	13	1.78	1.64	2.11	3.40	4.77	4.33	29.9
NW2D	15	2.05	1.89	1.99	3.44	4.87	4.20	28.9
NW2D	17	2.34	2.14	2.07	3.24	5.03	4.86	27.6
NW2F	13	1.77	1.64	2.20	3.32	4.46	5.32	38.1
NW2F	15	2.04	1.89	2.03	3.35	5.18	5.12	29.0
NW2G	13	1.77	1.64	2.20	3.32	4.46	4.92	32.5
NW2G	14	1.90	1.76	2.09	3.55	4.85	5.32	30.8
NW2G	15	2.03	1.89	1.96	3.43	5.01	4.66	28.5
NW2G	15	2.04	1.88	2.13	3.51	4.87	6.17	29.2
NW2G	16	2.18	2.02	2.01	3.60	4.80	4.73	30.1
SHS 15 Hz Average	15	2.04	1.89	2.03	3.43	4.98	5.04	28.9
MB3A	15	1.91	1.89	1.99	2.96	8.25	5.12	52.4
MB3B	15	1.96	1.89	2.09	3.49	8.15	6.17	52.4
MB3B	15	2.05	1.89	2.39	2.82	8.83	6.43	46.6
MB3C	15	2.14	1.89	2.26	2.94	8.77	5.97	52.7
MB3C	16	2.28	2.02	2.27	3.00	8.29	6.50	48.9
MB3C	17	2.42	2.15	2.35	2.89	9.06	5.91	44.1
MB3D	13	1.76	1.65	2.26	3.26	9.53	5.84	51.1
Baseline 15 Hz Average	15	2.02	1.89	2.18	3.05	8.5	5.92	51.0

Table 5.5: The summary of results are presented for each case and pump speed. Results include the Reynolds number upstream of the ramp, the observed freestream velocity, the momentum thickness, an estimate for the skin friction coefficient based on the slope of the log layer, the peak normalized Reynolds shear stress and its corresponding wall-normal location, and the angle at which the flow separates. The average value for each surface, based on data collected at the 15 Hz operating point, is also presented.

Chapter 6

Conclusions

This work shows that a superhydrophobic surface can hasten the onset of turbulent boundary layer separation. This is due to a reduction in the magnitude of the Reynolds shear stress within the boundary layer, and the accompanied reduction in the gradient of the Reynolds shear stress. Additionally, this work demonstrated the capabilities of a newly designed and constructed experimental facility that can be used for studying turbulent boundary layers over a variety of surfaces.

6.1 Flow Loop

A flow loop was successfully designed and constructed for the study of turbulent boundary layers over superhydrophobic surfaces. It is currently capable of achieving approximately 1.5 times the flow rate required to study the separation phenomena of interest, which appears to approach to a relatively constant separation angle for all surfaces around a flow rate of approximately 760 GPM (at 27 Hz pump frequency and a bulk velocity of approximately 3.1 m/s). If future studies using the facility require higher flow rates, confirmation of a permanent solution to the leaky pump casing seal would enable flow rates up to approximately 1700 GPM.

The test section of the flow loop demonstrates acceptably low freestream turbulence for studying turbulent boundary layers. The test section can be configured to study turbulent boundary layers in a flat plate configuration with or without injecting air for air layer drag reduction, as well as perform further studies in turbulent boundary layer separation. This work demonstrates that the facility can be used in the boundary layer separation configuration to study turbulent boundary layers at Reynolds numbers based on development length up to $Re_L = 6 * 10^6$.

6.2 Turbulent Boundary Layer Separation

This study shows clearly that an SHS can advance the onset of turbulent boundary separation. Data collected across a wide range of operating conditions demonstrate that coating the surface with an SHS causes a turbulent boundary layer to separate further upstream on a contoured backward facing ramp. The separation location on the baseline case, as well as the SHS coated case, is a function

of the freestream flow velocity. The application of an SHS to the surface caused the separation location to advance upstream at a lower freestream velocity than the baseline case. Additionally, at the fixed freestream velocity of 1.89 m/s, and corresponding Reynolds number of $Re_x \approx 2.0 * 10^6$, the turbulent boundary layer separated at the mean location 28.9° along the ramp. In contrast the turbulent boundary layer remained attached until the mean location 51° along the ramp. Velocities collected in the boundary layer upstream of the ramp show that the change in separation behavior is a result of a reduction in the Reynolds shear stress within the boundary layer.

Reynolds Shear Stress

On average, the SHS causes a 41% reduction in the peak magnitude of the Reynolds shear stress measured upstream of the ramp. This is accompanied by a 15% reduction in the location of the peak relative to the wall, though the overall profile maintains the same shape. This is in contrast to the observations from other studies of a zero pressure gradient turbulent boundary layer over an SHS, which saw increases in the Reynolds shear stress with the application of SHS coatings.[8] Those studies noted that the increased shear stress would be expected to come from increased roughness of the surface, which would have to be in a range which did not negatively affect the drag while still increasing the Reynolds shear stress. The surface NW2 in our study was of comparable roughness to the surfaces studied by Gose et al. However the difference in observed Reynolds stresses may come from either a difference in the plastron topography or from a difference in the highest peaks of roughness elements. A surface such of the one studied by Gose et al. that decreases skin friction while increasing Reynolds shear stresses would be expected to delay the onset of separation.

The study of turbulent boundary layer separation from rough surfaces by Song et al. also showed an increase in Reynolds shear stress caused by the surface roughness.[9] However, the increased Reynolds shear stress of the fully rough surface was accompanied by an increase in the skin friction, resulting in an earlier boundary layer separation. Our study is unique among these other studies in identifying a decrease in Reynolds shear stress and that being the mechanism by which the separation location is advanced. However our results are consistent with the expectation that the Reynolds shear stress would decrease if a surface successfully reduced skin friction without introducing roughness elements.

Application to Ships

This study shows that applying an SHS to a ship hull could advance the onset of separation, leading to an increase in pressure drag. This concern needs to be taken into account when considering superhydrophobic coatings as a drag reducing method. Further work is needs to determine how the results of this study will translate to higher length and velocity scales. The study demonstrated that at higher flow rates, the influence of the SHS on separation location became negligible. An understanding of this phenomenon at ship-scale Reynolds numbers would be needed to determine if the geometry of a ship would need to be modified to optimize the overall performance of superhydrophobic drag reduction.

6.3 Further Work

There is further work to be done within this field. In addition to some open questions about this particular study that could be addressed with different instrumentation, there is opportunity to study the scaling of the phenomena observed as well as develop better understanding of the behavior of the plastrons.

Open Questions

The key open question from this study was the measurement of the skin friction. The current results based on the slope of the logarithmic layer are believed to include a bias induced by the fringe pattern. Instrumentation with improved near-wall resolution could be used to estimate the skin friction based on the velocities in the viscous sublayer.

An improved estimate for skin friction would also be useful to complete a comparison of balance of the terms influencing the evolution a x-momentum in equation 2.28. Once the accuracy of all the terms is verified, an analysis comparing the scale of the four terms - which come from the freestream velocity gradient, the viscous dissipation, the turbulent mixing, and the wall-normal convection - may be able to explain the trends in changing separation location as a function of Reynolds number.

Extensions of this Work

The behavior of plastrons on the surface of the SHS is a complex problem to study with many possible avenues of research. First, a robust method needs to be developed to characterize and quantify the plastrons. This is needed for both the static state of the plastrons, as well as their dynamic behavior as they interact with the turbulent boundary layer. A method is needed to quantify the behavior of the microscopic bubbles while simultaneously applying that method to large surface areas in order to track the aggregate influence on a turbulent boundary layer. In this study, a camera focused on the plastrons was able to capture the local state, but the narrow field of view did not capture the larger patches where plastrons were being pulled from the surface.

Additionally, it is unknown why the original thick plastrons seen on a newly submerged SHS do not return in the same state when they are replenished via air injection. Possible explanations could be surface contamination or physical damage to the SHS coating. Another explanation could be that the surface needs to be statically exposed to the air, such as being removed from the water and dried, opposed to dynamically having air flowing past.

Another extension of this work is to explore how the turbulent boundary layer separation behavior changes with variations in scale. One simple step would be to test the same ramp geometry with a shorter development plate. This may be able to identify if the behavior scales with Re_x, or if it scales with a different function of velocity. Additionally, adding a capability to control the water temperature enables additional scaling. As momentum thickness upstream of the ramp is modified by the SHS, it is impossible to match Re_θ at the same operating condition without controlling the viscosity. The ability to keep temperature and viscosity constant between runs is an additional benefit that will reduce one possible source of noise. The goal of this area of research would be to

identify the critical parameters that determine in which flow regimes the separation is sensitive to the presence of a drag reducing coating.

Bibliography

[1]M. Cames, J. Graichen, A. Siemons, and V. Cook, *Emission reduction targets for international aviation and shipping* (2015).

[2]M. Sofiev, J. J. Winebrake, L. Johansson, E. W. Carr, M. Prank, J. Soares, J. Vira, R. Kouznetsov, J.-P. Jalkanen, and J. J. Corbett, "Cleaner fuels for ships provide public health benefits with climate tradeoffs", Nature communications **9**, 1–12 (2018).

[3]J. R. Paulling, ed., *The principles of naval architecture series* (The Society of Naval Architects and Marine Engineers, 2010).

[4]J. W. Gose, K. Golovin, M. Boban, J. M. Mabry, A. Tuteja, M. Perlin, and S. L. Ceccio, "Characterization of superhydrophobic surfaces for drag reduction in turbulent flow", Journal of Fluid Mechanics **845**, 560 (2018).

[5]J. Seo and A. Mani, "On the scaling of the slip velocity in turbulent flows over superhydrophobic surfaces", Physics of Fluids **28**, 025110 (2016).

[6]H. Park, C.-H. Choi, and C.-J. Kim, "Superhydrophobic drag reduction in turbulent flows: a critical review", Experiments in Fluids **62**, 229 (2021).

[7]S. Wang and L. Jiang, "Definition of superhydrophobic states", Advanced Materials **19**, 3423–3424 (2007).

[8]J. W. Gose, K. Golovin, M. Boban, B. Tobelmann, E. Callison, J. Barros, M. P. Schultz, A. Tuteja, M. Perlin, and S. L. Ceccio, "Turbulent Skin Friction Reduction through the Application of Superhydrophobic Coatings to a Towed Submerged SUBOFF Body", Journal of Ship Research **65**, 266–274 (2021).

[9]S. Song and J. Eaton, "The effects of wall roughness on the separated flow over a smoothly contoured ramp", Experiments in Fluids **33**, 38–46 (2002).

[10]C. D. Aubertine, J. K. Eaton, and S. Song, "Parameters controlling roughness effects in a separating boundary layer", International Journal of Heat and Fluid Flow **25**, Turbulence and Shear Flow Phenomena (TSFP-3), 444–450 (2004).

[11]Ö. Savaş, "Me-263 turbulence", Unpublished course notes., Feb. 2017.

[12]S. B. Pope, *Turbulent flows* (Cambridge University Press, Cambridge, 2000).

[13]F. M. White, *Viscous fluid flow*, 3rd ed. (McGraw-Hill, New York, 2006).

[14]H. Schlichting, *Boundary-layer theory*, trans. by J. Kestin, 7th ed. (McGraw-Hill, New York, 1979).

[15]D. Coles, "The law of the wake in the turbulent boundary layer", Journal of Fluid Mechanics **1**, 191–226 (1956).

[16]D. Spalding et al., "A single formula for the law of the wall", Journal of Applied Mechanics **28**, 455–458 (1961).

[17]L. Castillo, X. Wang, and W. K. George, "Separation Criterion for Turbulent Boundary Layers Via Similarity Analysis ", Journal of Fluids Engineering **126**, 297–304 (2004).

[18]B. S. Stratford, "The prediction of separation of the turbulent boundary layer", Journal of Fluid Mechanics **5**, 1–16 (1959).

[19]W. Wu and U. Piomelli, "Effects of surface roughness on a separating turbulent boundary layer", Journal of Fluid Mechanics **841**, 552–580 (2018).

[20]J. W. Gose, K. B. Golovin, J. M. Barros, M. P. Schultz, A. Tuteja, M. Perlin, and S. L. Ceccio, "Laser doppler velocimetry measurements of a turbulent boundary layer flow over sprayed superhydrophobic surfaces", in Tenth international symposium on turbulence and shear flow phenomena (Begel House Inc., 2017).

[21]I. Nedyalkov, "Design of contraction, test section, and diffuser for a high-speed water tunnel", MA thesis (Chalmers University of Technology, 2012).

[22]J. M. Wetzel and R. E. A. Arndt, "Hydrodynamic Design Considerations for Hydroacoustic Facilities: Part I—Flow Quality", Journal of Fluids Engineering **116**, 324–331 (1994).

[23]M. Raffel, C. E. Willert, F. Scarano, C. J. Kähler, S. T. Wereley, and J. Kompenhans, *Particle image velocimetry: a practical guide* (Springer, 2018).

[24]E. Aljallis, M. A. Sarshar, R. Datla, V. Sikka, A. Jones, and C.-H. Choi, "Experimental study of skin friction drag reduction on superhydrophobic flat plates in high reynolds number boundary layer flow", Physics of Fluids **25**, 025103 (2013).

[25]*Quick guide to surface roughness measurement*, 2229, Mitutoyo America Corporation (Dec. 2016).

[26]J. Kestin, M. Sokolov, and W. A. Wakeham, "Viscosity of liquid water in the range -8 °c to 150 °c", Journal of Physical and Chemical Reference Data **7**, 941 (1978).

[27]S. Chandrasekhar, *Newton's principia for the common reader* (Clarendon Press, 2003).

Appendix A

Discussion of Governing Equations

A.1 Introduction to the Governing Equations of Fluid Flow (for readers who have not studied fluid dynamics)

The behavior of an medium in motion is governed by the law's of motion outlined by Sir Isaac Newton in his work "Principia".[27]

Newton's first law establishes the concept of inertia, or an object's resistance to change in its state of motion. Skipping forward we recall Newton's third law: "For every action, there is an equal and opposite reaction." This concept allows us to relate the forces between two interacting bodies. But Newton's second law is the key to developing a governing equation for the motion of a fluid. While many focus on the case of constant mass in which the force on a body is equal to mass times the acceleration of the body, the more general form of the law states that the force is equal to the time rate of change of momentum. We will apply this to an infinitesimal element of fluid within a larger continuum of fluid in order to derive our governing equations of motion.

It should be noted that Newton's second law describes behavior in a Lagrangian reference frame, or terms of forces acting on a particular parcel of material as it moves through space. The material derivative is used to convert this expression into an Eulerian reference frame, in which the forces are applied to the material that is located at a particular point in space. Newton's second law applied to an infinitesimal element is given in equation A.1, where the mass of the element is given by m, the velocity vector of the element is given by $\vec{\mathbf{u}}$, and the net forces on the element are given by $\vec{\mathbf{F}}$.

$$\frac{D(m\vec{\mathbf{u}})}{Dt} = \vec{\mathbf{F}} \tag{A.1}$$

Recall that material derivative can be decomposed in to a local partial derivative with respect to time and a convective derivative representing the local change in a property as a result of that property being carried in or out of the infinitesimal element by the surrounding velocity field. This is shown in equation A.2 for the arbitrary property g.

$$\frac{Dg}{Dt} = \frac{\partial g}{\partial t} + \vec{\mathbf{u}} \cdot \nabla g \tag{A.2}$$

If the expression in equation A.1 of Newton's second law is divided by the volume of the infinitesimal element of fluid, we arrive at an expression based on the local properties given in equation A.3, where $\vec{\mathbf{f}}$ is the volume-specific force on the fluid. This gives us a differential equation that describes fluid flow.

$$\frac{D(\rho\vec{\mathbf{u}})}{Dt} = \vec{\mathbf{f}} \tag{A.3}$$

Navier-Stokes Equations

For the applications explored in this work, some assumptions can be made about the fluid that enable simplifications to the equations. The fluid is assumed to be incompressible, meaning that the density is not a function of the pressure. This is applicable to most cases of the flow of liquid, as well as flows of gases with velocities much lower than the speed of sound in the gas. A stronger assumption of constant density can be applied when variations in temperature or solute concentration (e.g. salinity) are small within the domain of interest. This enables the constant density term to be moved outside of the material derivative, resulting in equation A.4.

$$\rho\frac{D(\vec{\mathbf{u}})}{Dt} = \vec{\mathbf{f}} \tag{A.4}$$

The forces within the fluid can be decomposed into three parts: the normal forces, the shear forces, and the body forces. A normal force, by definition acts normal, or directly into, to the face on which it acts. Shear forces act tangential to, or along the face of, the surface. Body forces are distributed throughout the fluid, acting on the fluid as a whole. The most common example of a body force is the force that results from the pull of gravity. Within an incompressible fluid, the normal force consists of the negative of the pressure gradient. The shear force develops as a result of the viscosity of a fluid resisting velocity gradients. A second assumption is the fluid is Newtonian, or the shear stress developing from viscosity has a linear relationship with the velocity gradient. This is expressed in equation A.5, where τ represents the shear stress and μ is the viscosity. The viscosity is assumed to be constant for fluids with small variation in temperature within the domain.

$$\tau = \mu\frac{\partial\vec{\mathbf{u}}}{\partial\vec{\mathbf{x}}} \tag{A.5}$$

After these are assumptions are applied, with all of the body forces coming from gravity, the governing equations for fluid motion take the form of the Navier-Stokes equations for an incompressible fluid. The vector form is given in equation A.6, where $\hat{\mathbf{z}}$ is in the unit vector pointing upward, opposite the direction of acceleration due to gravity.

$$\rho\frac{D(\vec{\mathbf{u}})}{Dt} = -\nabla P + \mu\nabla^2\vec{\mathbf{u}} - \rho g\hat{\mathbf{z}} \tag{A.6}$$

Continuity

In addition to the conservation of linear momentum that is expressed in the Navier-Stokes equations, the conservation of mass is required in the form of the continuity equation. Equation A.7 states that mass can be neither created nor destroyed.

$$\frac{D\rho}{Dt} = 0 \tag{A.7}$$

With an assumption that the density is constant, the continuity equation simplifies to the following.

$$\nabla \cdot \vec{\mathbf{u}} = 0 \tag{A.8}$$

Appendix B

Additional Plots of Results

B.1 Velocity Profiles in Wall Units

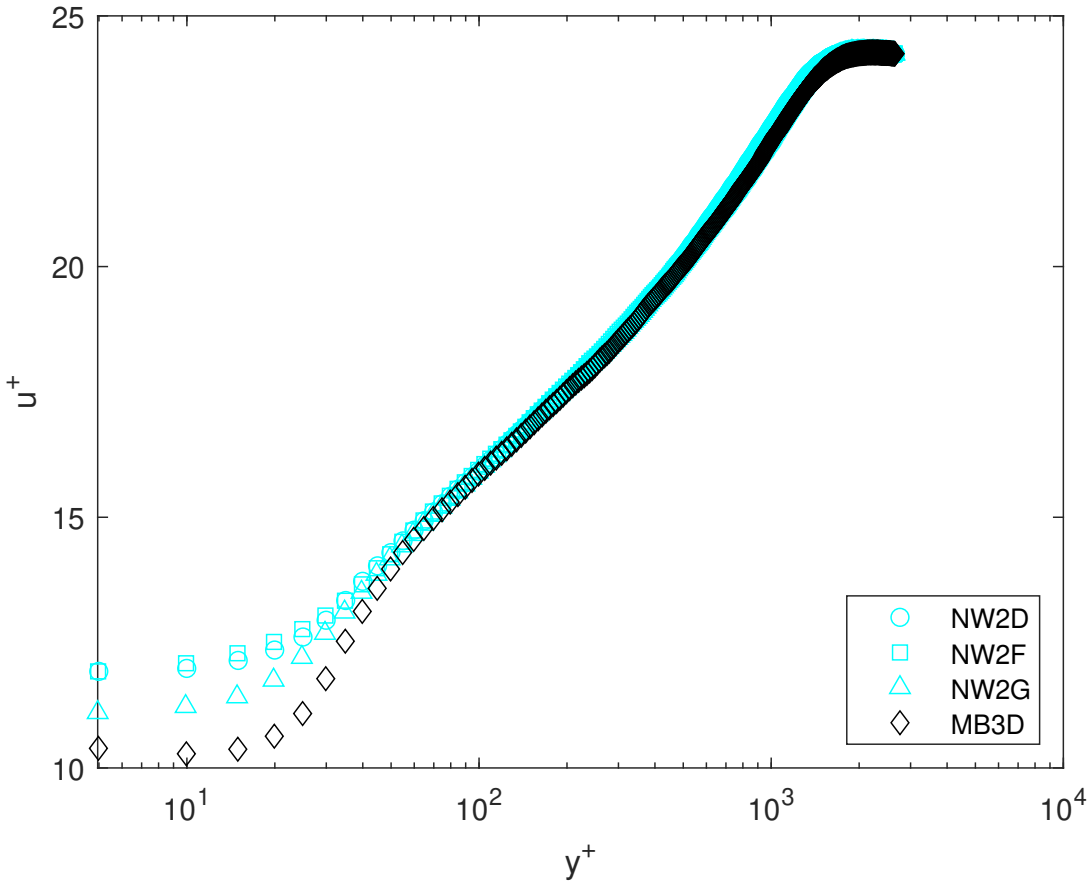

Figure B.1: The velocity profile, plotted in wall units, for data collected with the pumps at 13 Hz.

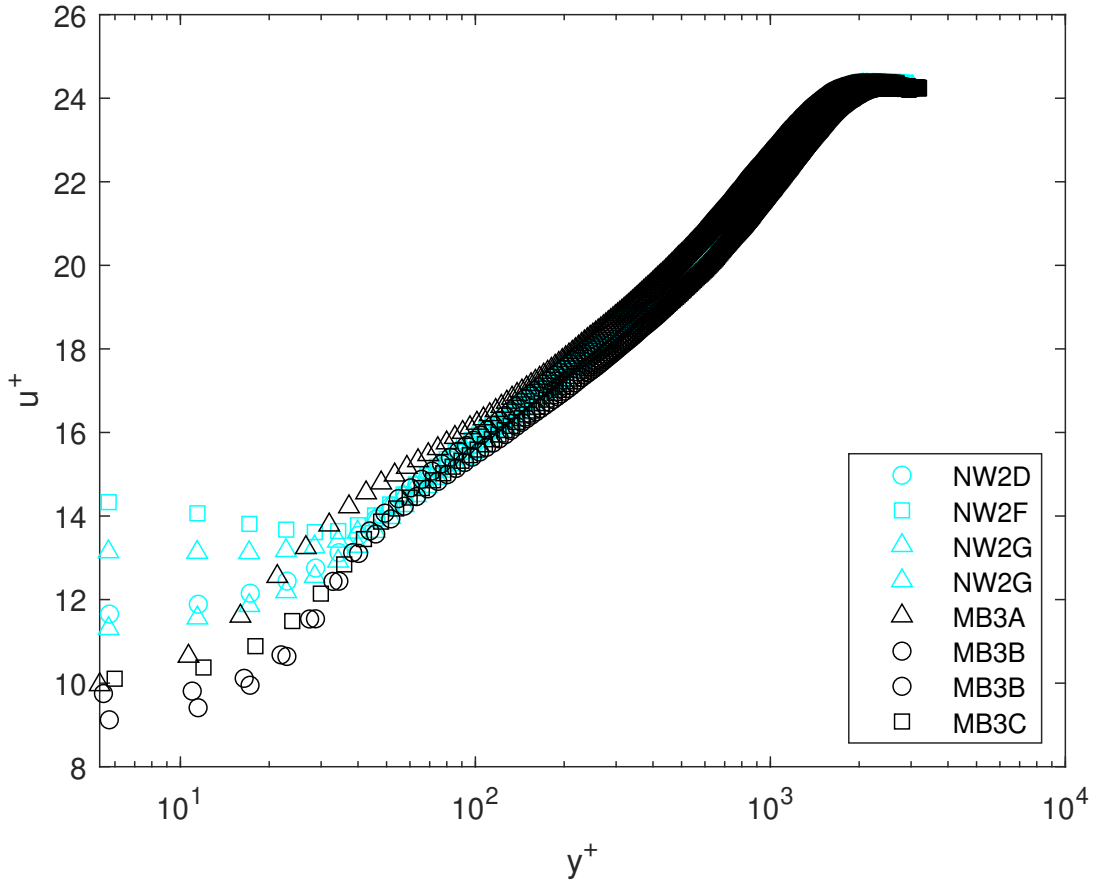

Figure B.2: The velocity profile, plotted in the wall units, for data collected with the pumps at 15 Hz.

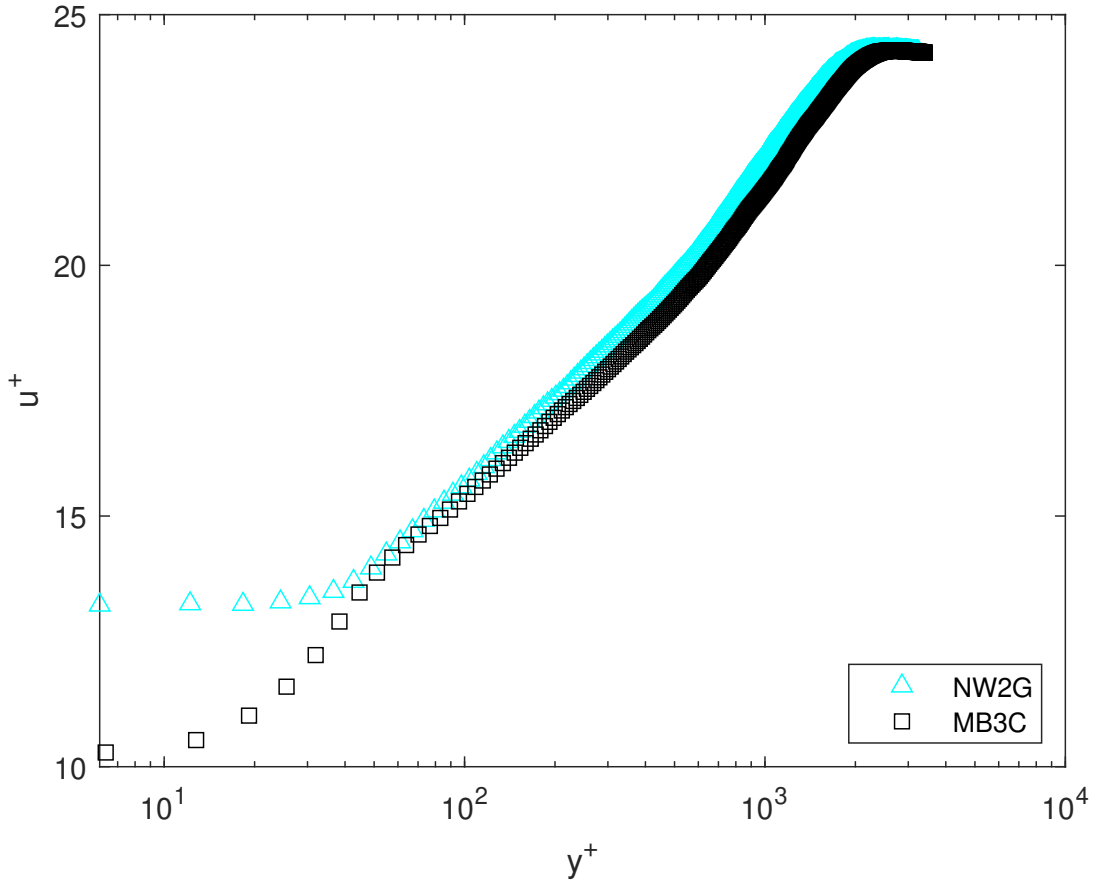

Figure B.3: The velocity profile, plotted in wall units, for data collected with the pumps at 16 Hz.

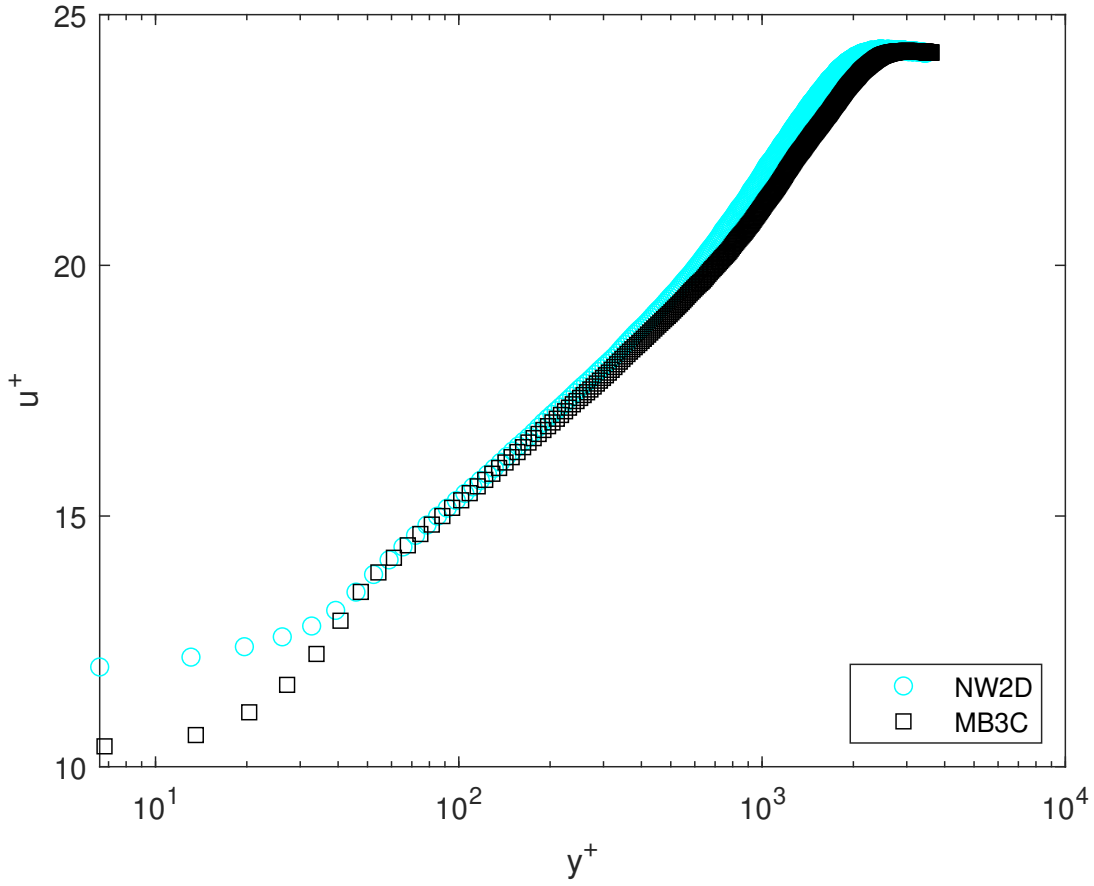

Figure B.4: The velocity profile, plotted in wall units, for data collected with the pumps at 17 Hz.

B.2 Velocities and Reynolds Stresses in the Boundary Layer

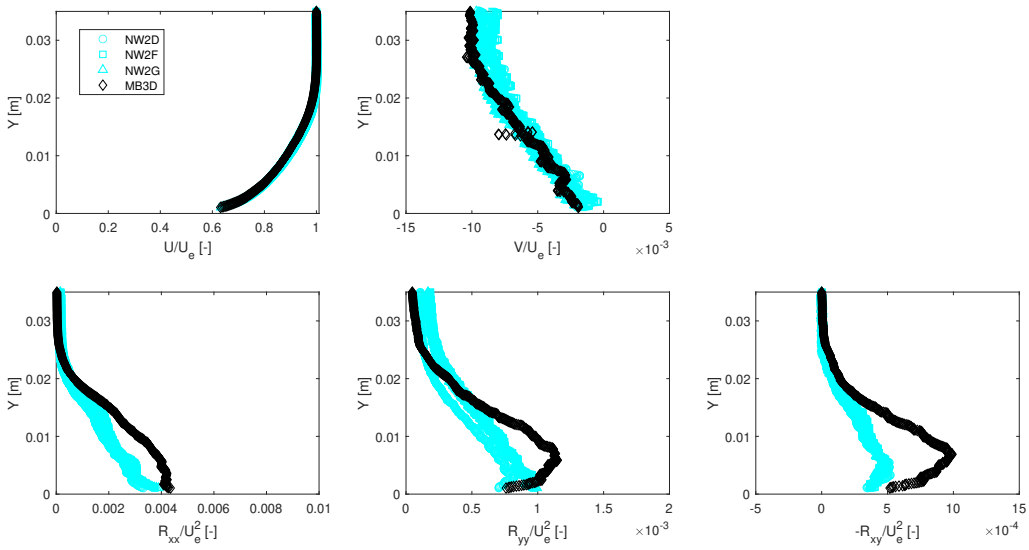

Figure B.5: The profiles of mean velocities and Reynolds stresses in the boundary layer for data collected at 13Hz.

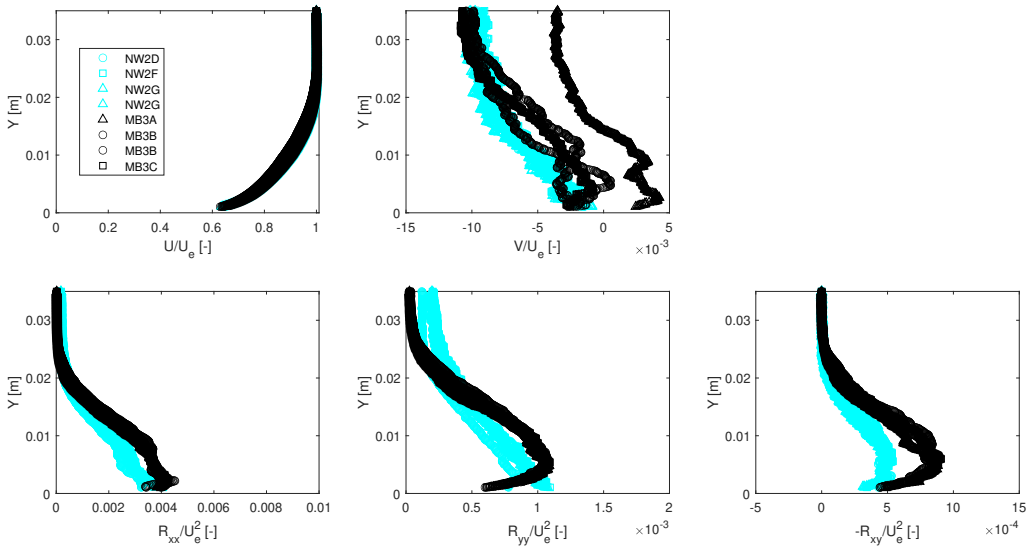

Figure B.6: The profiles of mean velocities and Reynolds stresses in the boundary layer for data collected at 15Hz. Note that the data from case MB3A appears to have an offset in mean velocity in the y direction. The wall-normal mean velocity should trend to zero at the wall. The source of this error is unknown.

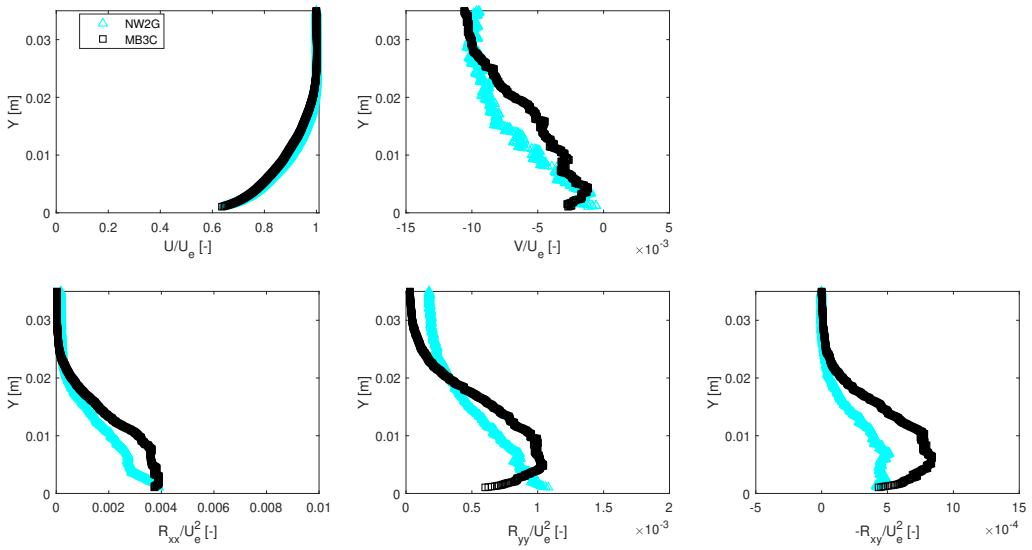

Figure B.7: The profiles of mean velocities and Reynolds stresses in the boundary layer for data collected at 16Hz.

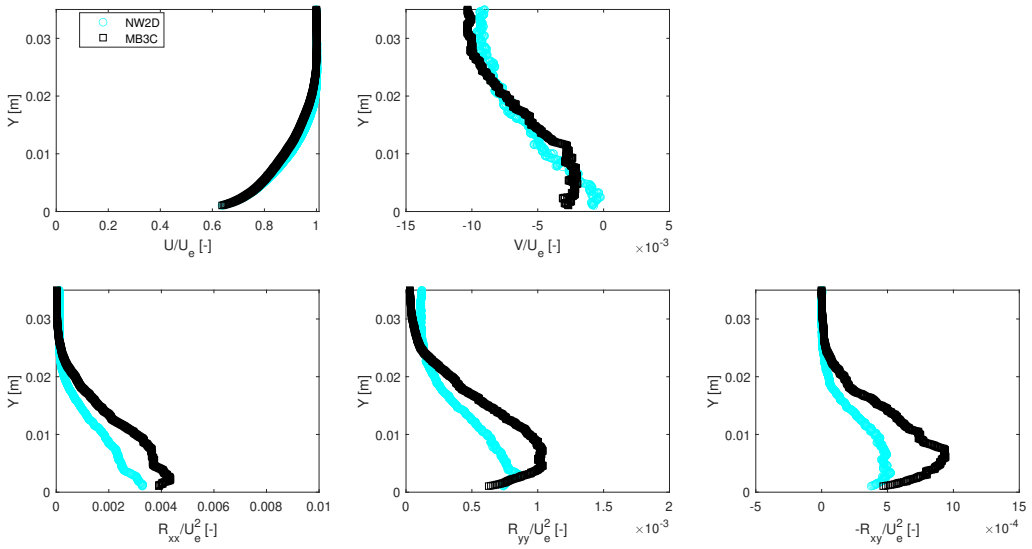

Figure B.8: The profiles of mean velocities and Reynolds stresses in the boundary layer for data collected at 17Hz.

B.3 Estimated Skin Friction Coefficient

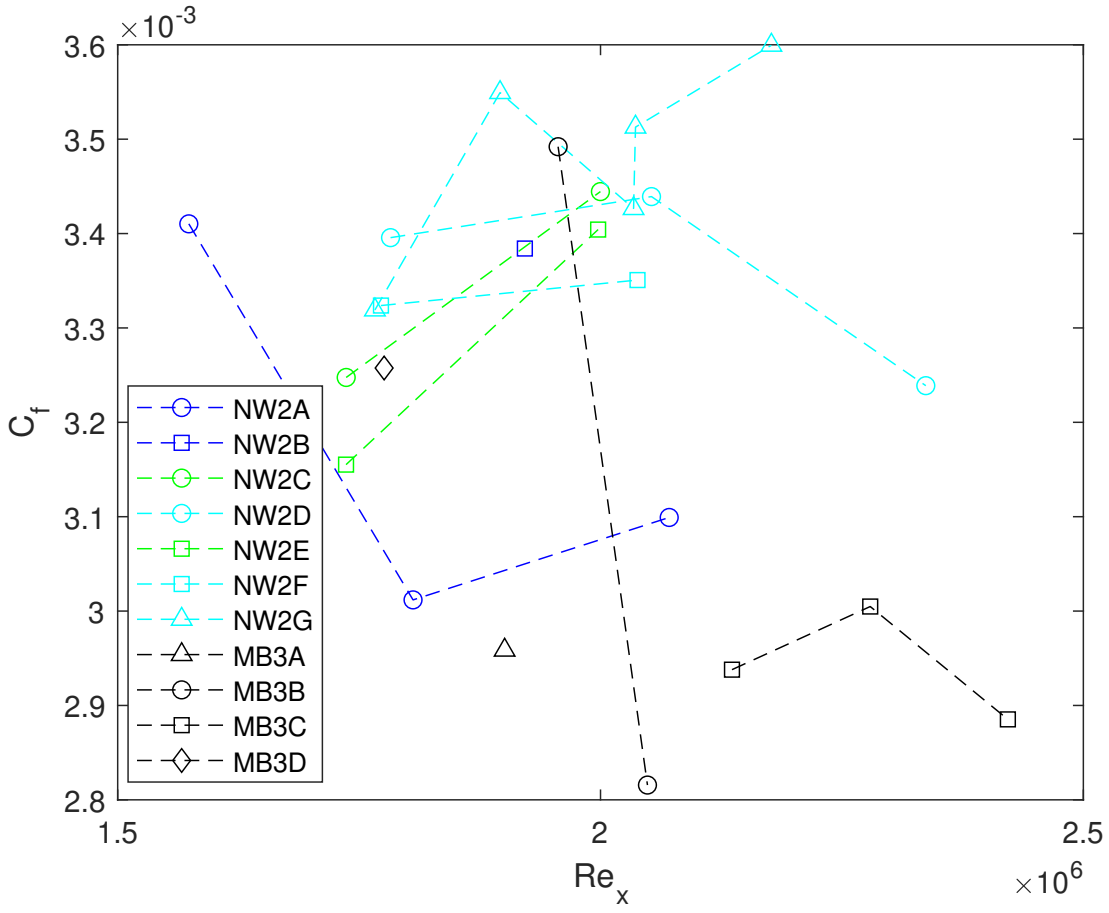

Figure B.9: The estimated skin friction coefficient, based on the slope of the velocity profile in the logarithmic region of the boundary layer.